1999

# High temperature phase equilibria studies in the Bi-Sr-Ca-Cu-O-Ag system

Lawrence Margulies
*Iowa State University*

# INFORMATION TO USERS

This manuscript has been reproduced from the microfilm master. UMI films the text directly from the original or copy submitted. Thus, some thesis and dissertation copies are in typewriter face, while others may be from any type of computer printer.

**The quality of this reproduction is dependent upon the quality of the copy submitted.** Broken or indistinct print, colored or poor quality illustrations and photographs, print bleedthrough, substandard margins, and improper alignment can adversely affect reproduction.

In the unlikely event that the author did not send UMI a complete manuscript and there are missing pages, these will be noted. Also, if unauthorized copyright material had to be removed, a note will indicate the deletion.

Oversize materials (e.g., maps, drawings, charts) are reproduced by sectioning the original, beginning at the upper left-hand corner and continuing from left to right in equal sections with small overlaps. Each original is also photographed in one exposure and is included in reduced form at the back of the book.

Photographs included in the original manuscript have been reproduced xerographically in this copy. Higher quality 6" x 9" black and white photographic prints are available for any photographs or illustrations appearing in this copy for an additional charge. Contact UMI directly to order.

UMI®

Bell & Howell Information and Learning
300 North Zeeb Road, Ann Arbor, MI 48106-1346 USA
800-521-0600

# High temperature phase equilibria studies in the Bi-Sr-Ca-Cu-O-Ag system

by

Lawrence Margulies

A dissertation submitted to the graduate faculty

in partial fulfillment of the requirements for the degree of

DOCTOR OF PHILOSOPHY

Major: Materials Science and Engineering

Major Professor: R. W. McCallum

Iowa State University

Ames, Iowa

1999

Graduate College
Iowa State University

This is to certify that the Doctoral dissertation of

Lawrence Margulies

has met the dissertation requirements of Iowa State University

Signature was redacted for privacy.

Major Professor

Signature was redacted for privacy.

For the Major Department

Signature was redacted for privacy.

For the Graduate College

# TABLE OF CONTENTS

## ABSTRACT

A variety of experimental techniques were utilized to examine the high temperature phase equilibria in the Bi-Sr-Ca-Cu-O-Ag system. Quenching studies were used to determine the liquid solubility of Ag in the $Bi_2Sr_2CaCu_2O_8$ (Bi2212) melt and the details of the peritectic decomposition pathway of Bi2212 as a function on Ag content and oxygen partial pressure ($PO_2$). A liquid immiscibility region between oxide and Ag liquids in the 8-98 at% range was found above 900°C. Two eutectics were found in the Bi2212-Ag pseudo-binary. On the oxide rich side, a eutectic exists at approximately 4 at% Ag. On the Ag rich side, a eutectic exists at approximately 98 at% Ag at a temperature of 15°C below the melting point of pure Ag. Six distinct solid phases were found to be in equilibrium with the partial melt within the Ag content and $PO_2$ range studied. The stability of these solid phases were found to be highly sensitive to $PO_2$, and to a much lesser extent Ag content. High temperature x-ray diffraction (HTXRD) studies of this system are in conflict with these results. It is suggested that these discrepancies are due to experimental artifacts caused by the significant thermal gradients and lack of full bulk sampling which is inherent in conventional HTXRD designs.

In part II, a new furnace design compatible with synchrotron radiation sources is introduced to address these problems. This design allows for full bulk sampling in a low thermal gradient environment using Debye-Scherrer transmission geometry. Sample spinning is also introduced in the design to eliminate preferred orientation and incomplete powder averaging and allow for quantitative phase analysis and structural refinement. Studies on model systems are presented to demonstrate the capabilities for high resolution

structural studies ($Al_2O_3$) and time resolved phase transformation studies ($SrCO_3$). Finally, the Bi2212 system is examined to confirm the quenching results of part I, and to demonstrate the degree to which this new HTXRD design solves the problems associated with conventional designs.

# GENERAL INTRODUCTION

Understanding the phase equilibria and structure of material systems at high temperatures is critical for gaining a better grasp on the thermodynamics and kinetics of condensed matter systems, as well as in guiding the processing parameters for producing novel microstructurally tailored materials. The question then arises: How can one study materials at high temperatures on both a microstructural and atomic structural level?

A number of techniques have been developed for probing the structure of materials at high temperatures. A common approach is rapidly cooling the material from the temperature and atmosphere of interest with the goal of quenching in the high temperature equilibrium structure. The material can then be easily characterized by conventional techniques (microscopy, spectroscopy, diffraction). This technique has a number of disadvantages. If one is interested in studying systems within a range of temperatures, it becomes necessary to prepare a large number of samples, and subsequent analysis can be time consuming. Furthermore, when dealing with quenched materials, one can never be certain that the high temperature structure has in fact been frozen in. This can be particularly difficult, if not technically impossible, when dealing with partial liquid phase regions or metastable high temperature structures with limited kinetic barriers. For example, there are a number of well known high temperature structures that cannot be maintained even with the fastest attainable quenching rates (SV, $Ni_3V$).

A number of in situ high temperature techniques have been used to complement quenching techniques, but again, these bring with them their own specific problems.

- **Electron microscopy**: A number of hot stages have been developed for scanning and transmission electron microscopes. These techniques, though, often do not provide information that is representative of the bulk material. TEM is primarily a local structure probe and is limited in its ability to give bulk equilibrium data. SEM, as well, probes only the surface region. In addition, these techniques are problematic for samples which are sensitive to atmosphere and actively exchange materials with a gas phase at elevated temperatures.

• **Optical microscopy**: Hot stages developed for optical microscopy have many of the disadvantages of electron microscopes. In addition, limited information can be gained, and this technique is generally only useful in conjunction with other techniques in order to confirm the chemical and crystallographic identity of observed phases.

• **X-ray diffraction**: With the development of increasingly sophisticated structural refinement models and code, high temperature powder diffraction has the potential for providing an extremely powerful tool for studying non-ambiant phase equilibria and structures. Unfortunately, many of the same problems associated with hot stage microscopy also plague conventional high temperature diffraction techniques. The typical penetration depth of $CuK_\alpha$ radiation is 10 μm, so that only a surface layer is probed. With the development of a third generation of synchrotron radiation sources, the increased availability of high energy x-rays can be used to solve this problem. The high flux of these sources at high energies (35-100 keV) allows for full bulk sampling of mm sized samples. In addition, more practical sample containment can be used to protect highly reactive or volatile materials.

This thesis is organized into two fairly distinct parts which address two approaches to high temperature phase equilibrium measurements. Part I examines the results of a quench study on the partial liquid phase equilibria in the Bi-Sr-Ca-Cu-O-Ag system. Scanning electron microscopy with energy dispersive spectroscopy (SEM-EDS) and chemical analysis was performed on rapidly quenched samples (melt-spinning, oil quenching) in order to study the liquid solubility of Ag in Bi2212 and the effect of $PO_2$ and Ag content on the peritectic decomposition of Bi2212. These results are in considerable disagreement with most high temperature x-ray diffraction studies, and this provides part of the motivation for the work described in Part II of this thesis. Part II describes the development of a new experimental design for performing high temperature x-ray diffraction using synchrotron radiation. The goal was to address the problems associated with conventional high temperature diffraction systems, which are thought to be responsible for the disagreement between quenching and in situ diffraction studies in the Bi2212 system. The use of synchrotron radiation allows for a significant redesign of the x-ray furnace and diffraction geometry. This new design not only minimizes thermal gradients and provides for full bulk sampling, but also allows for a higher

level of quantitative data collection by minimizing artifacts associated with preferred orientation and incomplete powder averaging. In part II, the design and capabilities of this system are presented through the examination of well characterized model systems. Finally, the Bi2212 system is re-examined with this system in order to confirm the reliability of the quenching results presented in part I and to highlight the limitations of conventional high temperature x-ray diffraction systems.

# PART I

## PARTIAL LIQUID PHASE EQUILIBRIA IN THE Bi-Sr-Ca-Cu-O-Ag SYSTEM

# INTRODUCTION

The initial discovery of high temperature superconductivity in copper oxide systems brought about an immediate state of euphoria over the potential uses of such a new class of materials. The reality of the situation, though, soon sunk in as it became increasingly clear that this class of potentially revolutionary materials brought with them new sets of problems associated with microstructural control. An important figure of merit for bulk superconductors is the critical current ($J_c$), defined as the current density that the material is able to carry before the superconducting state is destroyed and normal resistive current flow begins. Although the intrinsic intragranular $J_c$ of high $T_c$ superconductors is quite high, bulk polycrystalline materials exhibit much lower $J_c$. In the last ten years it has become clear that $J_c$ is a complex function of the microstructural details, most notably the second phase content and grain boundary structure.

There are three major problems associated with microstructural control of bulk high $T_c$ materials during processing:

- **Mechanical Stability**: The desired form for many potential applications is in long lengths of wire or tape. Processing crack free, flexible lengths of wire out of a brittle ceramic is a challenging materials problem that has only begun to be addressed. To date the most promising route lies in utilizing a composite structure in which the ceramic is encased in a metal sheathing. A typical processing route for forming such a composite structure is the Powder-In-Tube method[1,2]. Oxide precursor powder is packed into a metal (commonly Ag) tube. The packed tube is then drawn, rolled, or swaged with intermediate heat treatments. The annealing procedure is critical for forming the desired core microstructure. The use of a ductile metal sheathing is necessary for mechanical stability, although additional complexities are introduced. An extra component is effectively added to the system, further complicating the phase diagram. Thermal expansion mismatch between the metal and ceramic can lead to crack formation at high cooling rates. This is especially troublesome for phases which are stable only at elevated temperatures such as $(Bi,Pb)_2Sr_2Ca_2Cu_3O_y$ (Bi2223).

Finally, residual gases from incomplete carbonate decomposition in the precursor powders can be trapped leading to bubble formation within the wire.

• **Weak Links**: An important difference between high $T_c$ materials and conventional low $T_c$ superconductors is in the characteristic pairing distance of the superconducting charge carriers. The coherence length ($\xi$) of high $T_c$ superconductors is unusually small (3-30Å). Defects that are larger than the coherence length can disrupt supercurrent flow and limit $J_c$. When a supercurrent tunnels across a normal region, it is attenuated by a factor proportional to $\exp(-t/\xi)$, where t is the thickness of the barrier. Due to the small coherence length of high $T_c$ materials, even barriers which are just a few atoms thick can appreciably limit the superconducting current flow. The superconducting current flow is also highly anisotropic, being confined to the $Cu_2O$ planes. As a result, polycrytalline materials must be highly textured to ensure good coupling between the $Cu_2O$ planes across adjacent grains. For these reasons, grain boundaries are often a barrier to current flow. Small second phase buildup or high angle grain boundary interfaces can effectively decouple the grains. This is often modeled in terms of insulating Josephson junctions between superconducting grains, and is termed a weak link. The three dimensional weak link structure is often the limiting factor in the $J_c$ of bulk superconductors.

Partial melt processing of high $T_c$ materials has proven effective in addressing the weak link problem. The solid state diffusion rates are often too low to eliminate many current limiting defects in a reasonable amount of time. The presence of a liquid phase greatly enhances atomic mobility, improving the grain boundary structure. More importantly, though, melt processing has been shown to be highly effective at producing well textured material. In melt processed Bi2223 tapes, it is thought that a reaction at the Ag/oxide interface is responsible for the texture, although at present this is poorly understood[3].

•**Flux Creep**: For high field applications, there is another mechanism which is responsible for limiting $J_c$. High $T_c$ materials are type II superconductors, so that in moderate fields there will be partial magnetic flux penetration. The flux is distributed within the bulk in quantized bundles known as flux vortices. These vortices are essentially small flattened cylindrical volumes of non-superconducting material with a radius on the order of the

coherence length. The vortices repel each other, so that there is sufficient superconducting volume around each vortice to allow for unimpeded supercurrent flow. However, the Lorentz force due to this supercurrent flow can act on nearby vortices, causing motion. The motion of flux lines within the superconductor produces a voltage drop, introducing resistive heating, which often leads to catastrophic runaway behavior leading to complete loss of superconductivity. As individual flux lines become pinned at defect sites, the mutual repulsion between vortices will produce a flux line lattice, referred to as an Abrikosov lattice. The vortices become, in effect, frozen in this lattice. Flux lattice motion can be pinned by careful introduction of intragranular defects. Both the size and distribution of these defects must be tailored to maximize their effectiveness as flux pinning centers. Ideally, one would like pancake shaped defects with a radius on the order of the coherence length to be uniformly distributed within the grains.

A number of techniques have been developed for introducing a flux pinning defect structure. Neutron or ion bombardment has been found to be particularly effective in producing columnar defects which are well suited for pinning flux vortices[4,5]. Obviously, though, such a technique is not practical for commercial applications. A more promising technique consists of forming fine second phases within the superconducting matrix[6]. A number of high $T_c$ phases exhibit a large range in solid solubility. The single phase stability boundaries are highly dependent of oxygen partial pressure ($PO_2$) and temperature. By careful processing, a supersaturated solid solution can be formed which will precipitate extremely fine second phase particles within the grains when annealed at low temperatures[7].

In order to further improve microstructural control during processing of bulk high $T_c$ materials, a better understanding of the multicomponent system phase diagrams is necessary. To date, phase diagram information in these systems in far from complete due to a number of experimental difficulties as well as the overwhelming size of the phase space that must be examined to complete phase equilibria studies in these multicomponent systems. For example, the 110 K phase, $(Bi,Pb)_2Sr_2Ca_2Cu_3O_y$ is a six component system. In many cases it is necessary to add Ag as a seventh component due to its use as a sheathing material. Systematic phase diagram studies of seven component systems are often unrealistic, so that

well chosen cuts or projections must be examined that best address processing issues. A variety of phase diagram studies are critical to further processing improvements. The single phase region of high $T_c$ materials must be carefully mapped out with particular emphasis on the effect of varying $PO_2$. Partial liquid phase regions must also be examined in detail. Many high $T_c$ phases undergo complex peritectic reactions during melt-processing, and a better understanding of the partial liquid phase relations is critical to controlling microstructure of melt processed materials.

Currently, melt-processing is one of the most widely used techniques for producing highly textured $Bi_2Sr_2CaCu_2O_x$ (Bi2212) wires and tapes. These tapes are processed by partial melting followed by slow cooling through the peritectic. The literature is full of reports on partial melt techniques in the processing of Bi2212 and Bi2212/Ag composites. Unfortunately, most reports only offer information on the final microstructure that results from slow cooling and annealing. As a result, they are unable to determine the point of origin of the final second phase content. It is unclear whether the second phases formed upon the peritectic melting reaction and were retained during cooling or instead crystallized from the melt during cooling. Obviously, unless the control of microstructure is to remain a phenomenological guessing game, it is necessary to understand the details of the peritectic reactions that are initiated during melt processing. Only then can a proper understanding of how processing parameters effect the final phase content be claimed.

A major issue is the role of Ag and its effect upon the phase equilibria of the Bi2212 system. The formation of liquid enhances grain alignment along the c-axis. Additionally, the use of Ag as a substrate has been shown to increase the degree of texture of melt processed tapes[8]. It is thought that Ag is needed for good c-axis alignment, as Bi2212 crystals align along the oxide-Ag interface. However, it has been pointed out that well aligned Bi2212 could be formed on MgO or Au substrates. It has been suggested that Bi2212 nucleates at the gas-liquid interface[9]. In melt processed materials, a common observance is that the degree of alignment increases for Ag sheathed tapes with increasing $PO_2$. For low $PO_2$ processed tapes, it is observed that Bi2212 crystals align along pore surfaces within the ceramic core. Since the Bi2212 crystallization temperature increases with increasing $PO_2$, it is thought that nucleation will occur at the point at which oxygen is

supplied to the liquid. In the case of high $PO_2$ environments, the oxygen content will be highest at the Ag-liquid interface due to oxygen diffusion through Ag. In low $PO_2$, though, trapped air within pores may raise the crystallization temperature sufficiently to trigger nucleation at the pore surface.

It is well known that the use of Ag as a sheathing material acts to depress the onset of liquid formation by 15-25°C depending on oxygen partial pressure[10]. As a result, material near the Ag/Bi2212 interface will begin melting at a lower temperature than within the bulk. To ensure uniform melt processing throughout the sample, fine Ag powder must be mixed with the Bi2212 precursor powder.

There are contradictory reports in the literature on the effect of Ag additions on the $J_c$ of Bi2212. A number of researchers have reported that Ag enhances $J_c$ due to improvement of the intergranular weak links[11,12]. Others report a decrease of $J_c$ in Ag added material[13]. A common observation is that Ag begins to show detrimental effects above approximately 3 wt%[14]. This is attributable to changes in microstructure. Ag may act to pin grain growth, thereby increasing the grain boundary area and exacerbating the weak link effect. It has also been suggested that Ag at the grain boundaries may cause a mismatch of Cu-O planes across grain boundaries[12].

Diffusion studies of Ag in Bi2212 have demonstrated that the mean diffusion distances during modest processing times are much larger than the typical tape thickness[15]. As a result, the amount of Ag in the system is limited solely by its solubility and not by the diffusion rate. The question of solid and liquid solubility of Ag in Bi2212 is then key to optimizing melt processed material. More work needs to be done, then, to determine the details of the Bi-Sr-Ca-Cu-O-Ag phase diagram. In beginning this investigation there are two major issues to be addressed:

1) What is the nature of the Bi2212-Ag pseudo-binary diagram? A knowledge of this is important in recognizing the inherent limitations on Ag-Bi2212 compounds and how they should be processed.
2) What is the combined effect of Ag content and $PO_2$ on the details of the peritectic reactions that occur during melt-processing? Answering this question will involve a determination of the solid phases which are in equilibrium with the partial melt.

## LITERATURE REVIEW

The Bi-Sr-Ca-Cu-O-Ag phase diagram is a dense jungle, within which one may become easily disoriented and hopelessly lost. To prepare against such unfortunate circumstances it is best to begin slowly by considering first the derivative binary and ternary systems. For simplicity, such diagrams are often represented in terms of the equilibrium binary oxide components at the temperature and $PO_2$ of interest ($1/2Bi_2O_3$, SrO, CaO, CuO or $Cu_2O$). This convention will be used in this work, however, it is important to be aware that all such diagrams are projections along the oxygen composition axis and are presented for a fixed $PO_2$. The focus of this survey is on those regions of phase space which are directly related to issues involving the Bi2212 phase equilibria, so as to aid in understanding the details of the partial liquid phase regions in the Bi2212-Ag pseudo-binary as a function of $PO_2$. A fairly exhaustive review of the literature relating to the full system is provided as an aid to further study into currently less well explored corners of this formidable phase space. The sheer number of phase equilibria studies in these systems over the past 10 years has unavoidably led to some confusion regarding the nomenclature and stochiometery of newly discovered phases. A further aim of this review, then, is to clear up some of these discrepancies in order to assure unambiguous phase identification. The majority of the phase diagram work has been done in air (0.21 bar $O_2$). Unless explicitly stated, it is safe to assume that the details summarized below are valid only at this oxygen partial pressure.

### Pseudo-binaries

#### $1/2Bi_2O_3$-CaO[16-25]

The $1/2Bi_2O_3$-CaO pseudo-binary is quite rich, and a number of binary compounds have been found. The $Bi_2Ca_2O_5$ phase is stable up to 925°C in air. It has a triclinic unit cell of space group P1[16]. This compound had previously been identified as $Bi_7Ca_6O_{16}$[17]. $Bi_6Ca_4O_{13}$ has been identified as orthorhombic with space group C2mm[23], and was previously identified as $Bi_{10}Ca_7O_{22}$[24,25]. This phase decomposes above 855°C in air at which point a metastable high temperature BCC phase forms. The BCC phase, also called the β phase, exists as a solid solution from 35 to 45 mole% CaO. $Bi_2CaO_4$ is monoclinic

(C2/c) and decomposes at 778°C in air. $Bi_{14}Ca_5O_{26}$ is stable up to 732°C. Although its crystal structure remains unsolved, the complexity of its powder pattern suggests a triclinic symmetry. A rhombohedral (Rbar3m) solid solution exists for compositions of $(Bi_{1-x}Ca_x)_2O_{3-x}$ ($0.2<x<.25$). At high temperatures a FCC solid solution exists for $(Bi_{1-x}Ca_x)_2O_{3-x}$ ($0<x<.29$). This solid solution has a congruent melting point between 20 and 23 mole% CaO at 885°C.

**$1/2Bi_2O_3$-CuO**[26-33]

Only one binary compound has been confirmed in this system, $Bi_2CuO_4$, with space group P4/ncc. There is some disagreement as to whether it melts congruently or incongruently (to liquid and CuO), although there is general agreement that the decomposition temperature is approximately 845°C. $Bi_2CuO_4$ forms a eutectic with $Bi_2O_3$ at 770°C in air, and this represents the lowest liquid formation temperature in the Bi-Sr-Ca-Cu-O phase diagram. According to the phase diagram from [26] in air, $(Bi_{2+x}Cu_{1-x})_4O_7$ has a small solid solution range. This result has not been reproduced and there is considerable doubt regarding the existence of this phase. At low $PO_2$ (0.01 bar), $Bi_2CuO_4$ is no longer stable, and a simple eutectic is formed between $Cu_2O$ and $Bi_2O_3$ at 590°C[33].

**$1/2Bi_2O_3$-SrO**[34-42]

Six binary compounds have been identified in the $1/2Bi_2O_3$-SrO system. A rhombohedral solid solution (Sillen Phase)[40] exists which is similar to the corresponding phase in the $1/2Bi_2O_3$-CaO system. The solid solution range is slightly larger here with $(Bi_{1-x}Sr_x)_2O_{3-x}$ ($0.1<x<.265$). It has been suggested that this phase undergoes a polymorphic transition at approximately 700°C[36], although this has not been confirmed. $Bi_2SrO_4$ has been found to exist in high temperature and low temperature polymorphic forms with a transition temperature of 825°C. A metastable body centered tetragonal (I4/m) solid solution exists between 765°C and 985°C. This phase has been called $Bi_{1.22}SrO_{2.83}$, $Bi_4Sr_3O_9$, or $\gamma$. The line compound $Bi_2Sr_2O_5$ is orthorhombic with space group Pnma[37]. It is stable up to 925°C where it transforms to the high temperature BCT phase, forming the Sr rich phase boundary. $Bi_2Sr_3O_6$ is a rhombohedral (R3m) line compound which decomposes at 1210°C. $Bi_2Sr_6O_9$, sometimes referred to as $Bi_2Sr_7O_{10}$, is also rhombohedral and decomposes at 965°C.

**CaO-CuO**[20,43-49]

There are three binary compounds in the CaO-CuO system. $Ca_2CuO_3$ was the first to be discovered[43]. It is an orthorhombic (Immm)[46] line compound which undergoes a peritectic reaction to CaO and liquid at 1030°C in air. A second orthorhombic (Pmmn) phase, $CaCu_2O_3$, was found soon after and is stable only in a narrow temperature range between 985°C and 1018°C. $CaCuO_2$ is also orthorhombic (Cmca)[44] and is stable below 760°C. At reduced oxygen partial pressures, these phases can demonstrate considerable oxygen and cation nonstoichiometry. This behavior based on a thermodynamic assessment of the Ca-Cu-O system has been carefully studied and reported[47].

**CaO-SrO**[49,50]

CaO and SrO exhibit a complete solid solution above 900°C. Below this temperature there is a wide miscibility gap. Tentative binodal and spinodal curves have been computed using a subregular solution model[50], although there has been no experimental verification.

**CuO-SrO**[34,35,44,46,49]

There are three known compounds in the CuO-SrO system. $Sr_2CuO_3$ is orthorhombic (Immm) and stable up to 1220°C. $SrCuO_2$ is also orthorhombic (Cmcm) and is stable up to 1080°C. A recently discovered face centered orthorhombic phase has been identified in the literature as $Sr_3Cu_5O_8$[49] or $Sr_4Cu_7O_{12}$[35]. There is now general agreement that the actual stoichiometry of this phase is $Sr_{14}Cu_{24}O_{41}$.

**Pseudo-ternaries**

**1/2$Bi_2O_3$-CaO-CuO**[19,21,51,52]

There are no known ternary phases in this system, and no significant solubility regions of the constituent binary phases exist within the ternary field.

**1/2$Bi_2O_3$-CaO-SrO**[17,52-54]

A number of the binary compounds in the $Bi_2O_3$-SrO system show significant solid solution ranges with CaO. This is not so for the Ca-bismuthates which show little solubility of SrO, except for the rhombohedral Sillen phase which shows a complete solid solution between CaO and SrO. At 800°C, $Bi_2SrO_4$ can accept approximately 10% CaO substituted for SrO. $Bi_2Sr_2O_5$ accepts approximately 5% CaO substitution, while $Bi_2Sr_3O_6$ exists with as much as 50% CaO substituion. Finally, $Bi_2Sr_6O_9$ is stable with CaO substitutions of up to

10%. In addition to these extended solid solubility ranges, two new ternary compounds have been found. $Bi_{14}Sr_{6-x}Ca_{6+x}O_{33}$ (-.6<x<3.5) crystallizes in the monoclinic space group C2/m[55]. This phase has been referred to as the "2110" phase [56] and the "8250" phase[17]. Most recently, it has been suggested that the true stoichiometry of this phase is $Bi_{16}Sr_{7-x}Ca_{7+x}O_{38}$[54]. The second ternary phase exists in both high and low temperature forms. The low temperature form crystallizes in the orthorhombic Pmmm space group, while the high temperature form is monoclinic (Pc)[53]. The structure was solved for a sample with a Sr:Ca:Bi ratio of 49.5:16.5:34.0. This phase has been referred to as $Bi_9Sr_{11-x}Ca_{5+x}O_y$ (9$\underline{1}$15)[17] and 24x[57]. There is some disagreement as to the exact range of solid solubility, although it is seems clear that there is considerable solubility along the SrO-CaO line. Both of these new ternary compounds have been found to exist in equilibrium with the Bi2212 phase, so their illucidation has been helpful in clearing up some of the confusion regarding the phase equilibria dynamics of Bi2212 formation.

**1/2$Bi_2O_3$-CuO-SrO**[34,35,58-66]

Four ternary compounds have been identified in this system. The Raveau solid solution, $Bi_{2.2+x}Sr_{1.8-x}Cu_{1\pm x/2}O_z$ (0.0<x<0.15), is superconducting with a $T_c$ of 6 to 9K and has a tetragonal structure. This phase is commonly called 2201 or Bi2201, as it closely resembles the n=1 end member of the series $Bi_2Sr_2Ca_{n-1}Cu_{2n}O_{2n+4}$. It has also been referred to as $\underline{1}$1905 due to the Bi excess and Sr deficiency as compared to 2201[65]. The stochiometric 2201 composition is nonsuperconducting, and there is considerable evidence that the 2201 and raveau solid solution are two distinct phases, although some report a single solid solution within this region[64]. There is still considerable confusion regarding the differentiation of these two phases. This is due primarily to the psychological need to refer to the superconducting phase as 2201 despite the fact that the orthorhombic phase closest to this composition is nonsuperconducting. This nonsuperconducting phase has also been referred to as $Bi_{17}Sr_{16}Cu_7O_y$[58]. Subtle structural modulations in these phases seem to be sensitive to cation and oxygen stochiometry, so it is unlikely that this issue will be resolved easily. It seems unavoidable that both these phases will continue to be referred to as 2201 in the literature. The $Bi_4Sr_8Cu_5O_{19+x}$ ternary compound was initially identified as $Bi_2Sr_4Cu_2O_{9+x}$. It seems clear that this 1:2:1 composition was actually a multi-phased

sample. The crystal structure has been solved and reported as orthorhombic (Fmmm)[65]. $Bi_2Sr_3Cu_2O_8$ has been indexed with a C-centered monoclinic unit cell. Two additional phases have been reported, $Bi_2Sr_7Cu_2O_x$ and $Bi_4Sr_9CuO_x$[67]. Theses phases have not been reproduced and may have been stabilized by the use of 0.5wt% $Li_2CO_3$ as a mineralizer.

**CaO-CuO-SrO**[49,52,68-72]

The CaO-CuO-SrO system contains three solid solution series which extend from the CuO-SrO binary compounds. $(Sr,Ca)_2CuO_3$ shows complete solid solubility between CaO and SrO. The variation in the orthorhombic (Immm) cell parameters with Sr/Ca ratio has been found to follow Vegard's law[70]. $(Sr_{1-x}Ca_x)_{14}Cu_{24}O_{41}$ exists for $0<x<7$. Based on observed systematic extinction in powder patterns the possible space groups are Fmmm, F222, or Fmm2. The lattice parameters follow Vegard's law within the solid solution range. There is some disagreement as to the solubility limit for $(Sr_{1-x}Ca_x)CuO_2$. In general it is found that this phase is stable for $x<.65$ to .75 and crystallizes in the Cmcm orthorhombic space group. A ternary phase with a small solid solution range has been found in this system. $(Sr_xCa_{1-x})CuO_2$ is tetragonal (P4/mmm)[69] and is stable for $0.10<x<0.16$. According to [72], the Ca rich end member of $(Sr_{1-x}Ca_x)CuO_2$ is at $x=.62$ and a distinct ternary phase exists of composition $Sr_{0.3}Ca_{0.7}CuO_2$. This study was done in 100% $O_2$, which may explain the discrepancies with other studies.

**Pseudo-quaternaries**

**1/2$Bi_2O_3$-CaO-CuO-SrO**[17,59,64,65,73-81]

This system has been studied extensively due to the existence of two superconducting quaternary compounds, $Bi_2Sr_2CaCu_2O_{8+x}$ (2212) and $Bi_2Sr_2Ca_2Cu_3O_{10+x}$ (2223). There has been considerable disagreement in the literature concerning solid solubility ranges for these phases. A complete study of the single phase space would entail mapping the solid solution volumes within the $1/2Bi_2O_3$-CaO-CuO-SrO system at a series of temperatures and oxygen partial pressures. The sluggish kinetics in this system have prevented unambiguous phase boundaries from being drawn. As the superconducting properties can be sensitive to extremely low second phase content levels, determining these boundaries with precision is of more that academic concern. There is good agreement on the variation of the Sr and Ca content. At 800°C in air, $Bi_{2.18}Sr_{3-y}Ca_yCu_2O_{8+\delta}$ is stable for $.95<y<1.8$[80]. At higher

temperatures, the single phase region shrinks and is shifted toward Sr rich compositions. There is less agreement concerning the variability of Bi content in the 2212 phase. For $Bi_xSr_2CaCu_2O_{8+\delta}$, some studies find a maximum stability region of $2.05<x<2.3$[80,81]. Other studies have been a bit more generous, claiming extended stability regions as wide as $1.78<x<2.4$[65]. These discrepancies may be partly caused by Bi volatility during prolonged heat treatments, or by differing criteria for confirming "single phase" samples.

One of the more complete recent studies found that at 830°C in air 2212 was in equilibrium with 10 phases, leading to 16 distinct four phase equilbrium regions surrounding the 2212 primary phase field. These four phase tetrahedral volumes were mapped, and the three phase planes which define the surface of the 2212 crystallization volume were used to fit an analytical expression describing the 2212 primary crystallization field. This region was found to encompass a compositional range of 24 to 42 mole% Bi, 7 to 33 mole% Sr, 2 to 27 mole% Ca, and 19 to 43 mole% Cu. Solid state electrochemical techniques have been used to determine the phase stability limits for 2212 and 2223 in a $PO_2$ range of 1 bar to $10^{-6}$ bar $O_2$[76,77,79].

**Partial liquid phase equilibria**

A number of researchers have reported studies on the peritectic decomposition of Bi2212. These studies were done using a variety of techniques including high temperature x-ray diffraction, SEM analysis of quenched samples, and high temperature optical microscopy.

The first high temperature diffraction studies were done by Oka et al.[82,83]. There are serious questions regarding the validity of the results reported using high temperature diffraction. Phase separation can easily occur in partial liquid samples due to differences in density between solid and liquid phases. Large thermal gradients across the sample thickness and length can worsen this problem and prevent the differentiation of narrow phase regions due to a loss in temperature resolution. Quenching studies are potentially a more reliable method of investigating the partial liquid phase assemblage, but misleading results are possible if the quench rate is not sufficiently rapid. Bi2201 commonly forms during cooling of the partial liquid. Air and liquid nitrogen quenching are not sufficient to prevent significant crystallization and growth which can make identification of the high temperature

equilibrium phases difficult and unreliable. It is for this reason that early on many researchers mistakenly concluded that Bi2212 peritectically decomposed to liquid and Bi2201.

A review of the results that have been reported in the literature on the partial liquid phase equilibria for Bi2212 and Bi2212+Ag are summarized below at a number of oxygen partial pressures. There is considerable disagreement between these studies, due in part to the above mentioned experimental issues. It should be evident from this review that a careful and systematic study of the Bi2212 peritectic decomposition as a function of $PO_2$ and Ag content is needed to clear up this confusion.

**100% $O_2$**

Endo et al. [84] studied the phases present in water quenched Ag sheathed tapes held between 885° and 895° C in 100% $O_2$. They reported a phase assemblage of liquid, $(Sr,Ca)_3Cu_5O_x$, and a Cu-free phase. Zhang and Hellstrom[85] performed a similar study on oil quenched tapes and found $(Sr,Ca)_{14}Cu_{24}O_{41}$ and $Bi_2(Sr,Ca)_4O_x$ in equilibrium with liquid from 880° to 910° C. MacManus-Driscoll et al. [86] reported the reaction Bi2212 + Ag → liquid + $Bi_2(Sr,Ca)_3O_6$ + $(Sr,Ca)CuO_2$ from samples quenched in a solid state electrochemical cell. Buhl at al. [87] reported $(Sr,Ca)_{14}Cu_{24}O_{41}$ and $Bi_3Sr_4Ca_3O_z$ in equilibrium with liquid.

**21% $O_2$**

The majority of phase equilibria studies in the Bi2212-Ag system have been done in air. A high temperature study by Hein et [88,89] found 2212, CuO, an alkaline earth cuprate phase, and an unidentified phase in equilibrium with liquid on an MgO substrate at 920° C. This result is highly suspect, and most probably demonstrates the type of artifacts introduced due to the large thermal gradients in an open hot stage x-ray diffraction geometry.

MacManus-Driscoll et al. [86] reported the reaction Bi2212+Ag → liquid + $(Ca,Sr)_2CuO_3$ in their solid state electrochemical cell. In a high temperature x-ray diffraction performed by Oka et al. [82] $(Sr,Ca)CuO_3$ was observed in the melt at 900° C for Bi2212 on a Pt substrate. Hasegawa et al. [90] performed a high temperature XRD study of Bi2212 films on Ag substrates. They reported the reaction Bi2212 → liquid + $(Sr,Ca)CuO_2$ at 870° C. Subsequent oil quenching studies of these samples revealed an additional phase.

$Bi_2(Sr,Ca)_4O_x$, which they were later able to identify in high temperature XRD [91]. Hasegawa [92] also performed a high temperature diffraction study on Bi2212 on a MgO substrate. They reported $(Sr,Ca)CuO_2$ +$(Sr,Ca)Cu_2O_3$ + $Bi_2(Sr,Ca)_4O_x$ in the partial liquid at 880° C.

High temperatute x-ray diffraction was performed by Polonka et al. on Bi2212 with and without Ag on a Au substrate [93]. They reported $(Sr,Ca)CuO_2$ and liquid at 870°C, $(Sr,Ca)CuO_2$, $(Ca,Sr)_2CuO_3$, and liquid at 880°-890° C. For Ag added Bi2212, they reported $Bi_2(Sr,Ca)_4O_x$ and liquid at 850°-860°C. Matheis et al. [94] have performed high temperature diffraction and high temperature optical microscopy on Ag free material on an MgO substrate. They reported $(Sr,Ca)CuO_2$ + $(Ca,Sr)_2CuO_3$ + liquid at 900°C and $(Sr,Ca)CuO_2$ + $(Ca,Sr)_2CuO_3$ + (Ca,Sr)O + liquid at 950°C. Kase et al. [95] studied air quenched Bi2212 films on Ag foil. They reported $(Sr,Ca)CuO_2$ + $Bi_3(Sr,Ca)_7O_x$ + CuO + Bi2201 + liquid at 880°-890°C. Hellstrom and Zhang[85] reported $(Sr,Ca)CuO_2$ + $Bi_2(Sr,Ca)_4O_x$ + liquid from 870°-880°C, $(Sr,Ca)CuO_2$ + $(Ca,Sr)_2CuO_3$ + $Bi_2(Sr,Ca)_4O_x$ + liquid from 885°-900°C for oil quenched Ag sheathed tapes. Endo et al. [84] observed liquid and $(Sr,Ca)CuO_2$ in Ag tapes water quenched from 885°-895°C.

Hasebe et al. [96] performed high temperature optical microscopy on Bi2212 on a Ag substrate. They observed needle-like phases on the surface on the melt.. When the samples were water quenched from 890° C, they contained $(Sr,Ca)CuO_2$ and a Cu free phase in the quenched liquid. Air quenched samples, though, were found to contain $(Sr,Ca)CuO_2$ and Bi2201.

Suzuki et al. [97] developed an apparatus to perform simultaneous x-ray diffraction and optical microscopy on samples heated on an MgO substrate. They observed Bi2212 decomposing to $(Sr,Ca)CuO_2$ + Bi2201 + liquid at 887°C. The Bi2201 was observed only within a narrow temperature range, and above 894°C only $(Sr,Ca)CuO_2$ remained in equilibrium with the liquid. It is interesting to note that the Bi2201 was only observed after holding for several hours at temperature. The authors suggest that this implies sluggish formation kinetics of Bi2201 by precipitation from a liquid with low supersaturation.

**1% $O_2$**

Yoshida[98] examined water quenched Ag sheathed tapes using SEM-EDS analysis. His was one of the few studies to take into account effects of Bi2212 composition. $Bi_2Sr_xCa_{3-x}Cu_2O_x$ with $1.5<x<2.3$ was examined. For $1.8<x<2.1$ $Bi_2(Sr,Ca)_3O_6$, $(Sr,Ca)CuO_2$, $(Ca,Sr)_2CuO_3$, and liquid were in equilibrium at 850°C. For x= 2.3, $Bi_2(Sr,Ca)_3O_6$ and $(Sr,Ca)CuO_2$ were the equilibrium solid phases, while for x=1.6 only $(Ca,Sr)_2CuO_3$ exists. For the entire range of x, they found the liquid phase to have a Bi:(Sr,Ca) ratio of 1:1.

Hellstrom and Zhang[99] reported liquid, $(Ca,Sr)_2CuO_3$, and $Bi_2(Sr,Ca)_3O_x$ in Ag sheathed tapes quenched from 850° C. MacManus-Driscoll et al. [86] reported the reaction Bi2212+Ag → liquid + $(Ca,Sr)_2CuO_3$ in their solid state electrochemical cell study.

## EXPERIMENTAL RESULTS

### Liquid Solubility of Ag in Bi2212

In order to determine the high temperature solubility of Ag in a Bi2212 melt, samples were quenched from the temperature of interest by melt spinning in air. The samples consisted of Kalichemie Bi2212 blended with 20 wt% Ag powder and pressed into powder pellets. $SiO_2$ was used as a crucible at temperatures of 1100°C and below, and $Al_2O_3$ was used at 1100°C and above. Direct RF heating of the samples was unsuccessful, as the silver would melt and segregate without heating the oxide sufficiently enough to melt. Therefore, samples were heated radiantly using an Inconel susceptor. The susceptor also acted as an effective RF noise shield, allowing the use of a thermocouple within the crucible. The temperature was measured simultaneously by a K-type thermocouple in a $SiO_2$ sheath which was embedded in the melt, and by a two-color infrared pyrometer aimed at the susceptor. On reaching the desired temperature, the molten stream was ejected onto a copper chill block rotating at 20 meters per second.

In initial experiments, it was observed that in cases where after reaching temperature the Ag-Bi2212 melt failed to shoot from the crucible, the solidified melt consisted of a Ag nodule at the bottom of the crucible surrounded by oxide material. This suggests an extremely low solid solubility of Ag in Bi2212. The melt spun material that resulted from a successful run could be separated into two distinct types. Long lengths of Ag ribbon (10-50 cm) were thrown into a collection tube. Of these ribbons, some showed a double-sided morphology. The remainder of the ribbons were nearly purely metallic with small streaks of oxide glass near the ribbon edges. It seems clear that the double-sided ribbons resulted from a phase separated liquid stream. It is not clear, though, if the oxide glass seen on the metal ribbons was due to separation in the liquid or subsequent separation upon solidification. The second distinct type of melt-spun material was an oxide glass flake, 5-10 mm in length. The oxide glass flakes were thrown off the wheel at a lower trajectory than the metal ribbons, and as a result did not land in the collection tube. Instead the oxide glass flakes collected in the wheel chamber.

**Chemical analysis**

Chemical analysis (ICP-AES) of the oxide and metal ribbons are presented in Table 1. The oxide ribbons show an increase in Ag content from 6.1 at.% at 900°C to 9.8% at 1200°C. The two samples processed at 1100°C showed anomalously low Ag contents of 6.3% and 4.9%. In both these cases the ribbons agglomerated, which may have resulted in a slow quench and possible phase separation, explaining the lower Ag contents. The Bi content of the oxide ribbons steadily decreased from 28% at 900°C to 24% at 1200°C. Similarly, the Cu content decreased from 28% at 900°C to 25.2% at 1200°C. The Sr and Ca content of the oxide ribbons showed little systematic variation with temperature. The Si and Al contamination was minimal for samples processed in quartz, while samples processed in $Al_2O_3$ showed 4.5% Al and .3-2.1% Si in the oxide ribbons and negligible Si and Al content in the metal ribbons. The metal ribbons showed a decrease in Ag content with increasing temperature from 99% at 950°C to 96.7% at 1200°C. Again, the samples processed at 1100°C gave slightly anomalous results. Finally, the amount of Cu in the metal ribbons increased with temperature from 0.8% at 950°C to 2.2% at 1200°C. This may reflect an increased tendency to form metallic Cu with increasing temperature, which in turn is soluble in Ag.

**Thermal analysis**

Differential thermal analyses (DTA) were done on product ribbons to determine melting events and, therefore, invariant points on the pseudo-binary phase diagram. The DTA curve of a Ag-rich ribbon melt-spun at 950°C showed an onset of melting at 933°C in air. This compares to the onset of melting for pure Ag in air at 947°C. The suppression of onset temperature is indicative of a eutectic between Ag and Bi2212. The DTA curve of the oxide glass flake melt-spun at 950°C showed much more complex melting events. The endothermic event deviates from the baseline at 810°C with an initial onset of 830°C. This is followed by a compound melting indicative of multiple phase boundaries being crossed. An endothermic peak also occurs with an onset of 935°C, which correspond quite well with the measured onset temperature of the Ag rich ribbon. This 935°C endotherm further demonstrates the low solubility of Ag in Bi2212.

Table 1. ICP analysis, in mole % and cation ratio of Bi:Sr:Ca:Cu with Cu fixed at 2, of the prescursor Bi2212, oxide ribbons, and metal ribbons. Mole percentages are accurate to 1 to 3% relative.

| | Bi | Sr | Ca | Cu | Ag | Si | Al | Bi/Sr/Ca/Cu |
|---|---|---|---|---|---|---|---|---|
| Precursor | | | | | | | | |
| | 25.5 | 27.2 | 13.5 | 27.2 | - | - | - | 1.88/2.00/1.00/2.00 |
| Oxide ribbons | | | | | | | | |
| Temp (°C) | | | | | | | | |
| 900 | 30.0 | 24.5 | 11.2 | 28.0 | 6.1 | 0.1 | 0.0 | 2.14/1.75/0.80/2.00 |
| 950 | 28.4 | 24.8 | 12.5 | 26.4 | 7.6 | 0.2 | 0.1 | 2.15/1.87/0.95/2.00 |
| 1000 | 28.4 | 24.0 | 12.4 | 27.6 | 7.5 | 0.1 | 0.0 | 2.05/1.74/0.90/2.00 |
| 1100[a] | 28.0 | 25.2 | 12.7 | 27.5 | 6.3 | 0.3 | 0.0 | 2.04/1.84/0.93/2.00 |
| 1100[ab] | 24.7 | 25.2 | 12.7 | 25.9 | 4.9 | 2.1 | 4.5 | 1.91/1.95/0.98/2.00 |
| 1200[b] | 24.0 | 23.5 | 11.7 | 25.2 | 9.8 | 0.3 | 4.6 | 1.99/1.86/0.93/2.00 |
| Metal ribbons | | | | | | | | |
| 950 | 0.0 | 0.0 | 0.0 | 0.8 | 99.0 | 0.0 | 0.0 | 0.00/0.00/0.00/2.00 |
| 1000 | 0.3 | 0.2 | 0.1 | 1.2 | 98.2 | 0.0 | 0.0 | 0.50/0.33/1.68/2.00 |
| 1100[a] | 0.1 | 0.0 | 0.0 | 1.2 | 98.6 | 0.0 | 0.0 | 0.17/0.00/0.00/2.00 |
| 1100[ab] | 0.4 | 0.2 | 0.1 | 4.4 | 94.9 | 0.0 | 0.0 | 0.18/0.09/0.05/2.00 |
| 1200[b] | 0.3 | 0.3 | 0.2 | 2.2 | 96.8 | 0.1 | 0.1 | 0.27/0.27/0.18/2.00 |

[a] in $Al_2O_3$ crucible with thermocouple

[b] Ribbons aglomerated, resulting in a slow quench and possible phase separation.

**Discussion**

As it is beyond the scope of this study to deal correctly with the six dimensional Bi-Sr-Ca-Cu-O-Ag phase diagram, we instead consider a schematic pseudo-binary isopleth through the Bi2212-Ag system (Figure 1). In this isopleth we must make the approximation that both end points are congruently melting components. This is not the case for Bi2212, so this pseudo-binary will not follow the normal rules for binary phase diagrams. In particular, the compositions of all the phase presented in the diagram do not lie in the plane of the isopleth, and the lever law is not valid for the individual oxide phases. Starting with the pure Bi2212 compound, it is know that in air Bi2212 decomposes to $Bi_9(Sr_{1-x}Ca_x)_{16}O_x$ (9$\underline{1}$15) + $(Sr_{1-x}Ca_x)CuO_2$ (11) + liquid to (9$\underline{1}$15) + (11) + $(Sr_{1-x}Ca_x)_2CuO_3$ (21) + liquid to (11) + (21) + liquid to (21) + $(Ca_{1-x}Sr_x)O$ (10) + liquid to (10) + liquid and finally completely melts. As we move into the pseudo-binary isopleth, the lines separating these phase regions will blow out into additional cuts of phase volumes. The differentiation of these regions is beyond the resolution of this experiment, and the above phases will be lumped together as OX meaning solid oxide phases. Further elaboration on the details of these phase regions is held for a later section.

The main feature of the pseudo-binary diagram is the large liquid immiscibility between the oxide and Ag liquids which is clearly demonstrated by the segregation of Ag and Bi2212 melt in the air quenched crucible. As demonstrated by the two types of flakes obtained on melt spinning, the segregation was such that the composition at the limits of immiscibility for both sides of the region could be obtained from a single run at each temperature. On the Bi2212 side of the region, the slope of the boundary is approximately 1 at.%/100°C, while on the Ag side the slope is somewhat steeper. From this data it is not possible to extrapolate the critical point for the immiscibility region which is well outside the range of this experiment.

From the DTA measurements on both the oxide and Ag rich flakes, it is clear that a pseudo-eutectic exists on each side of the diagram. For the oxide rich side the existence of this eutectic has been known for some time, but the composition at which it occurs has not been extensively investigated.

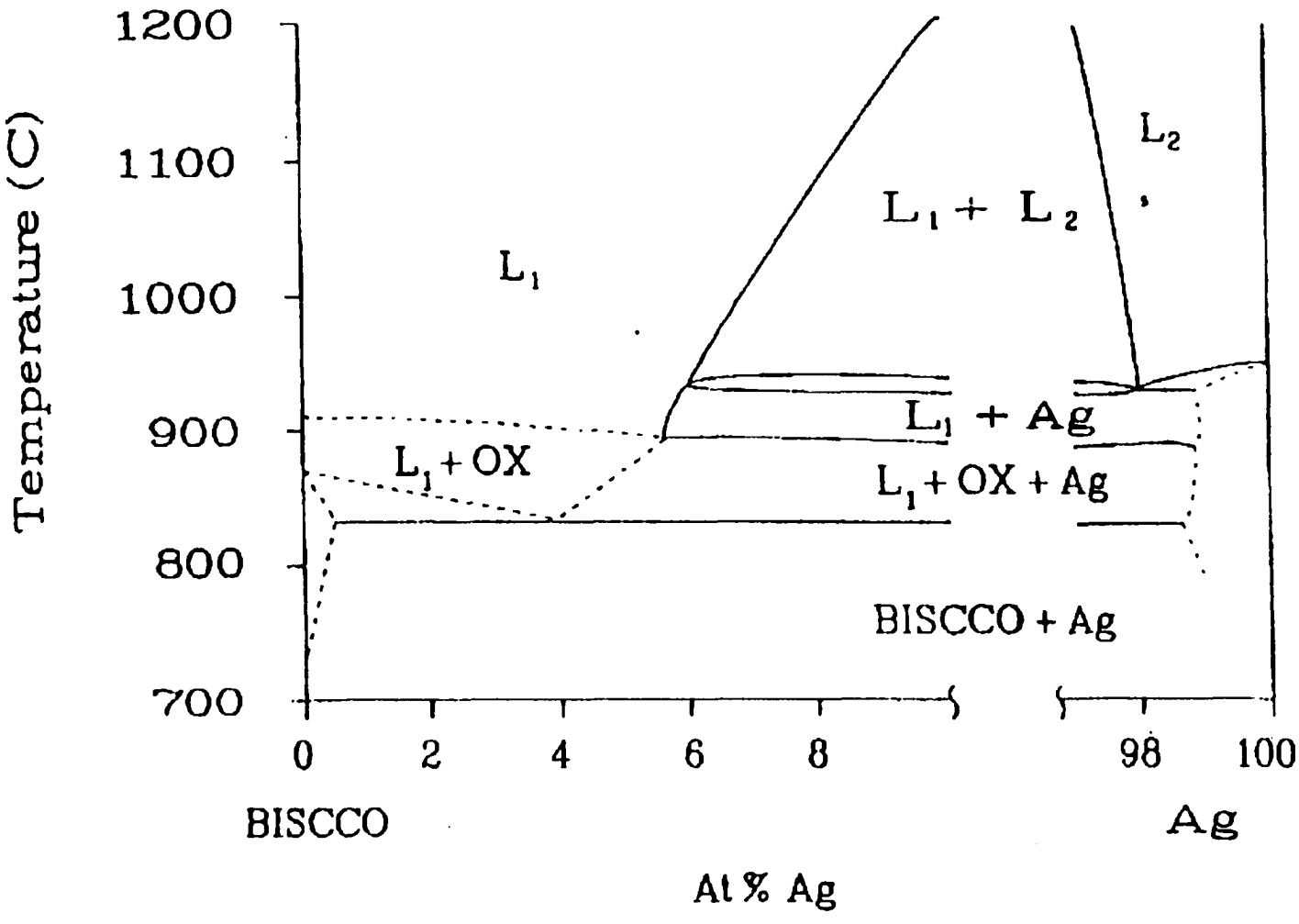


Figure 1. A schematic of the Bi2212-Ag pseudo-binary isopleth in air.

**Peritectic Decomposition of Bi2212 + Ag**

Although there have been a number of studies on the melting pathway of Bi2212, there has been no detailed study of the complete melting pathway that has taken into account the effects of both $PO_2$ and Ag content. While the use of Ag as a substrate has been shown to increase the degree of texture of melt-processed tapes, the eutectic reaction of Ag with Bi2212 further complicates the understanding of the partial melting[100]. It is well known that Ag reduces the first solidus temperature by 11-27°C depending on oxygen partial pressure[101]. Many decomposition studies have been done using samples on Ag tapes or substrates[85,93,102,103]. In these cases it is not clear how to quantify the Ag content of the samples. Of the results that have been reported, there are numerous discrepancies as to what second phases exist in the subliquidus melt. In 100% $O_2$, it has been reported that the pertitectic melting of Bi2212 results in liquid, $(Sr_{1-x}Ca_x)_{14}Cu_{24}O_{41}$ (14,24), and $Bi_9Sr_{11}Ca_5O_x$ (9$\underline{11}$5) [102]. Others have reported the decomposition products to be liquid, (14,24), and $Bi_2(Sr_{1-x}Ca_x)_4O_x$ (24x)[84], liquid, (14,24), and $Bi_3Sr_4Ca_3O_z$[87], or liquid, (14,24), and $Bi_2(Sr_{1-x},Ca_x)_3O_3$ (23x)[87]. In air, the reported decomposition products include liquid, $(Sr_{1-x}Ca_x)CuO_2$ (11), and 24x[88], liquid and (11)[83,104], and even liquid and Bi2223[105]. In 1% $O_2$, it has been reported that the first decomposition products are liquid, (11), $(Sr_{1-x}Ca_x)_2CuO_3$ (21), and 23x[103], liquid, (21), and 23x[85]and liquid and (21)[106]. The lack of consistency between these studies is of concern and will be addressed. The goal of this study is to present comprehensive data on the effect of $PO_2$ and Ag content on the decomposition pathway of Bi2212.

**Experimental procedure**

Commercial Bi2212 (Kalichemie) was heat treated in flowing (10 l/min) air at 860°C-870°C to minimize second phases and increase homogeneity. This heat treatment eliminated all second phases to the resolution level of differential thermal analysis (DTA) and x-ray diffraction (XRD). The $CO_2$ and hydrocarbon content of this process gas was reduced to below 2 ppm by a molecular sieve. The resulting powder was thoroughly mixed with 2 and 10 wt.% Ag powder (<5μm). ICP-AES analysis was done to determine the composition of the starting material. The cation ration was determined to be $Bi_{2.01}Sr_{2.04}Ca_{0.98}Cu_{2.00}$. The Ag contents of the three batches were measured at <.005, 2.4, and 9.6 weight percent.

Samples consisting of approximately 50-100 mg of powder in a MgO tube (2mm ID, 3mm OD) were suspended in the hot zone of a vertical furnace (Figure 2). The quartz tube in the furnace was evacuated and backfilled with 1%, 21% or 100%$O_2$ ($N_2$ balance). All gases used in this study were rated to below .5 molar percent hydrocarbons and 3.5 molar percent $H_2O$. Samples were held at temperature in a flowing atmosphere for 30 minutes and then dropped into an oil bath. Cross sections of the tubes were mounted and polished for scanning electron microscopy with energy dispersive spectroscopy (SEM-EDS) and microprobe analysis. Standardless semi-quantitative EDS data was collected for each sample. Microprobe analysis was done on a number of samples to verify the compositions of the solid phases. $Al_4Bi_2O_9$, CuO, $CaCO_3$, and $SrSO_4$ were used as internal standards.

Thermal analysis was performed using a Perkin Elmer DTA-7. Pressed pellets (20mg) were run in MgO cups and were surrounded with MgO powder to minimize discontinuities in thermal contact between the sample and cup. In addition, unlike Pt and $Al_2O_3$, MgO does not react with the partial melt. The scans were performed at 5°C/min. The oxygen partial pressure was controlled by mass flow controllers and monitored with a zirconia oxygen analyzer. The carbon content of all samples was measured by a Horiba EMIA-520 carbon analyzer.

**Results**

Table 2 shows the nomenclature and compositions as observed by electron microprobe for all equilibrium solid phases found in this study. Tables 3-5 present the observed phase assemblage with temperature for samples quenched in 100%, 21%, and 1% $O_2$, respectively. Isothermal cuts of a pseudo-ternary phase diagram have been constructed for each of the major phase regions above the solidus. A set of these cuts for each oxygen partial pressure is presented to aid in understanding the evolution of the phase assemblage with temperature.

**100% $O_2$**

Figure 3 shows the decomposition pathway of Bi2212 in 100% $O_2$. The first peritectic reaction, Bi2212 --> (14,24) + (9$\underline{1}$15) + L, occurs at 899°C. The (14,24) and (9$\underline{1}$15) both have a blocky appearance with a slight preference for growth along one axis (Figure 4a). With the addition of Ag this reaction remains the same, although it is lowered in

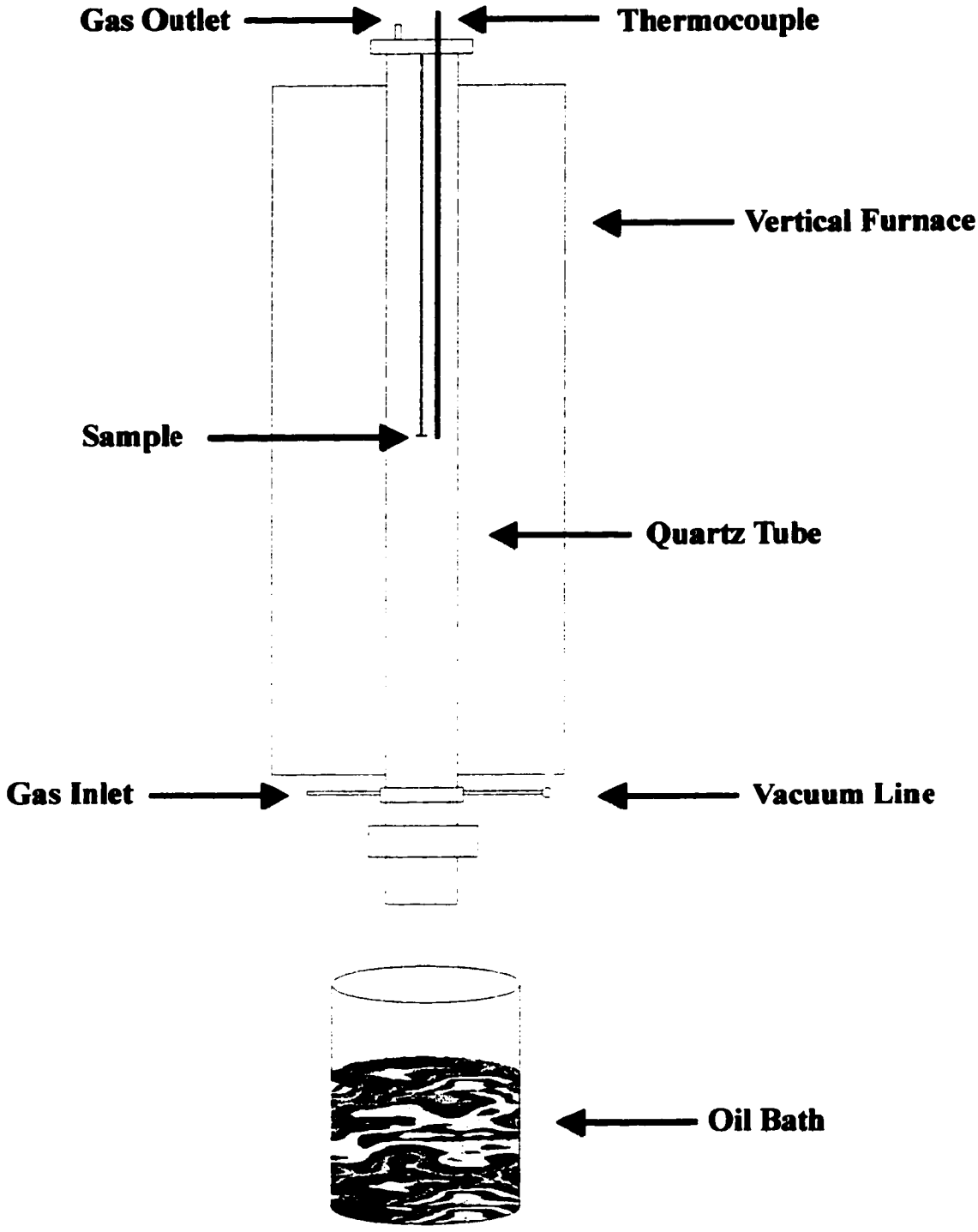


Figure 2. A Schematic of the drop tube apparatus

Table 2. Nomenclature and composition of solid phases as measured by electron microprobe.

| Phase | Nomenclature | observed solid solution range | Avg. composition by microprobe (Bi/Sr/Ca/Cu) |
|---|---|---|---|
| (14,24) | $(Sr_{1-x}Ca_x)_{14}Cu_{24}O_{41}$ | x= .25 - .35 | .04/.26/.11/.63 |
| (11) | $(Sr_{1-x}Ca_x)CuO_2$ | x= .32 - .45 | .02/.29/.20/.51 |
| (21) | $(Sr_{1-x}Ca_x)_2CuO_3$ | x= .63 - .80 | .04/.20/.46/.34 |
| (10) | $(Ca_{1-x}Sr_x)O$ | x= .02 - .05 | .01/.02/.96/.01 |
| 23x | $Bi_2(Sr_{1-x}Ca_x)_3O_y$ | x= .27 - .33 | .41/.38/.19/.02 |
| (9$\underline{1}$15) | $Bi_9(Sr_{1-x}Ca_x)_{16}O_x$ | x= .30 - .35 | .36/.41/.20/.03 |

temperature to 877°C at 2 wt.% Ag and 872°C at 10 wt.% Ag. At 2 wt.% Ag, all of the Ag is soluble in the ceramic liquid. No solubility of Ag in any of the solid phases was found up to the delectability limits of EDS. With 10 wt.% Ag added, the solubility limit of Ag in the liquid is exceeded, and the excess Ag remains as either a separate solid phase or as an immiscible liquid above 923°C[107]. Between 930°C and 940°C, (21) begins to nucleate from the liquid. The (21) has a very regular prismatic needle shape and shows a marked preference for growth along one axis (Figure 4b). From the pseudo-ternary representation, it is difficult to understand why the (21) begins to form before the (11). This difficulty arises due to the projection of Ca and Sr onto one axis. Figure 5 shows this same region with the Ca-Sr axes uncollapsed. In this representation, it is clear that the (11), (21), and (14,24) are not collinear and that the (11) does not lie in the (9$\underline{1}$15)-(21)-(14,24)-liquid phase region. A similar argument could be made in terms of the projection of oxygen composition onto the pseudo-ternary isotherm. In any case, it is clear that the geometric intuition suggested by a two dimensional cut of a three dimensional projection of a 5 component system can be misleading. By 944°C, the (14,24) has undergone a peritectic decomposition into (11) and liquid. The (11) has a similar prismatic shape to the (21) but tends to grow much thicker and less needle-like (Figure 4b). Again, the addition of Ag only acts to depress the temperature

Table 3. Phase content of samples quenched in 100% $O_2$ as determined by SEM-EDS.

| 0% Ag | | 2% Ag | | 10% Ag | |
|---|---|---|---|---|---|
| Temp(°C) | Phases | Temp(°C) | Phases | Temp(°C) | Phases |
| 902 | 14,24+9115+L | 900 | 14,24+9115+L | 900 | 14,24+9115+L |
| 912 | 14,24+9115+L | 910 | 14,24+9115+L | 918 | 14,24+9115+21+L |
| 930 | 14,24+9115+L | 918 | 14,24+9115+L | 922 | 14,24+9115+21+L |
| 942 | 14,24+9115+21+L | 926 | 14,24+9115+21+L | 929 | 9115+11+21+L |
| 943 | 14,24+9115+21+11+L | 929 | 9115+11+21+L | 939 | 9115+11+21+10+L |
| 944 | 9115+11+21+L | 933 | 9115+11+21+L | 940 | 9115+21+10+L |
| 945 | 9115+11+21+L | 944 | 9115+11+21+L | 944 | 9115+21+10+L |
| 948 | 9115+11+21+L | 952 | 9115+11+21+L | 950 | 9115+10 |
| 952 | 9115+11+21+L | 956 | 9115+11+21+10+L | 955 | 10+L |
| 960 | 9115+11+21+L | 960 | 9115+21+10+L | | |
| 963 | 21+9115+L | 966 | 21+10+L | | |
| 966 | 21+10+L | | | | |
| 973 | 21+10+L | | | | |
| 992 | 21+10+L | | | | |

Table 4. Phase content of samples quenched in 21% $O_2$ as determined by SEM-EDS.

| 0% Ag | | 2% Ag | | 10% Ag | |
|---|---|---|---|---|---|
| Temp(°C) | Phases | Temp(°C) | Phases | Temp(°C) | Phases |
| 890 | 9115+11+L | 880 | 9115+11+L | 872 | 9115+11+L |
| 900 | 9115+11+21+L | 895 | 9115+11+21+L | 877 | 9115+11+L |
| 910 | 9115+11+21+L | 910 | 9115+11+21+L | 884 | 9115+11+21+L |
| 920 | 9115+11+21+L | 915 | 9115+11+21+L | 890 | 9115+11+21+L |
| 925 | 11+21+L | 920 | 11+21+10+L | 900 | 9115+11+21+L |
| 930 | 11+21+L | 925 | 11+21+10+L | 905 | 9115+21+10+L |
| 937 | 21+10+L | 930 | 11+21+10+L | 910 | 9115+21+10+L |
| 943 | 21+10+L | 935 | 21+10+L | 920 | 21+10+L |
| 945 | 21+10+L | 941 | 21+10+L | 930 | 21+10+L |
| 950 | 21+10+L | 950 | 21+10+L | 942 | 10+L |
| 965 | 10+L | 962 | 10+L | | |

Table 5. Phase content of samples quenched in 1% $O_2$ as determined by SEM-EDS.

| 0% Ag | | 2% Ag | | 10% Ag | |
|---|---|---|---|---|---|
| Temp(°C) | Phases | Temp(°C) | Phases | Temp(°C) | Phases |
| 850 | 23x+11+21+L | 845 | 23x+11+21+L | 842 | 23x+11+21+L |
| 857 | 23x+11+21+L | 850 | 23x+11+21+L | 851 | 23x+11+21+L |
| 860 | 23x+11+21+ 10+L | 860 | 23x+11+21+10 +L | 859 | 23x+11+21+10 +L |
| 870 | 23x+11+21+ 10+L | 870 | 23x+11+21+10 +L | 861 | 23x+11+21+10 +L |
| 875 | 23x+11+21+ 10+L | 880 | 23x+10+L | 870 | 23x+21+10+L |
| 880 | 23x+21+10+L | 890 | 23x+10+L | 880 | 23x+10+L |
| 886 | 23x+21+10+L | 900 | 23x+10+L | 902 | 23x+10+L |
| 891 | 23x+10+L | 910 | 23x+10+L | 910 | 10+L |
| 897 | 23x+10+L | 920 | 10+L | 920 | 10+L |
| 910 | 23x+10+L | | | | |
| 920 | 10+L | | | | |

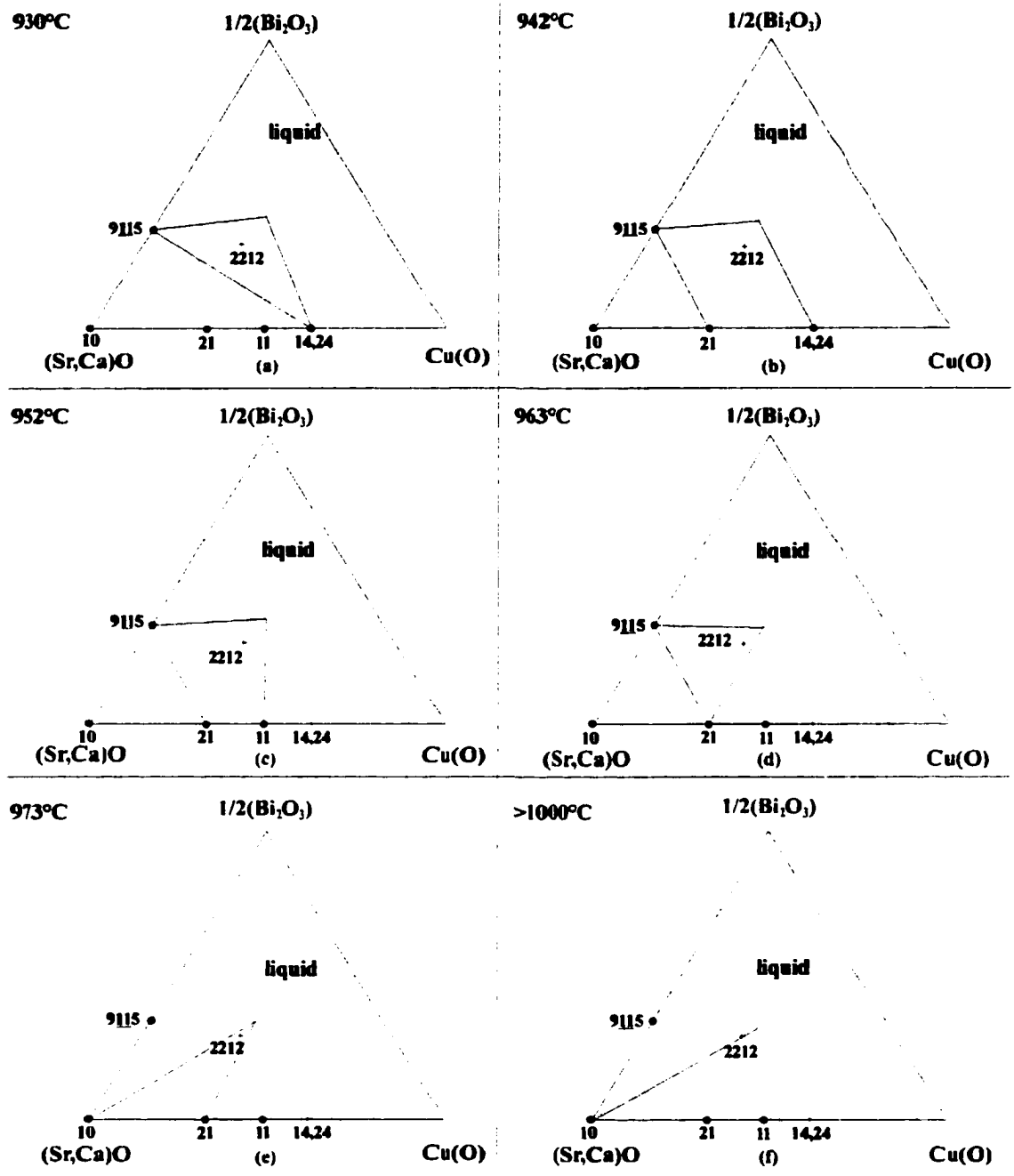


Figure 3. A series of pseudo-ternary phase diagrams illustrating the decomposition pathway of Bi2212 in 100% $O_2$.

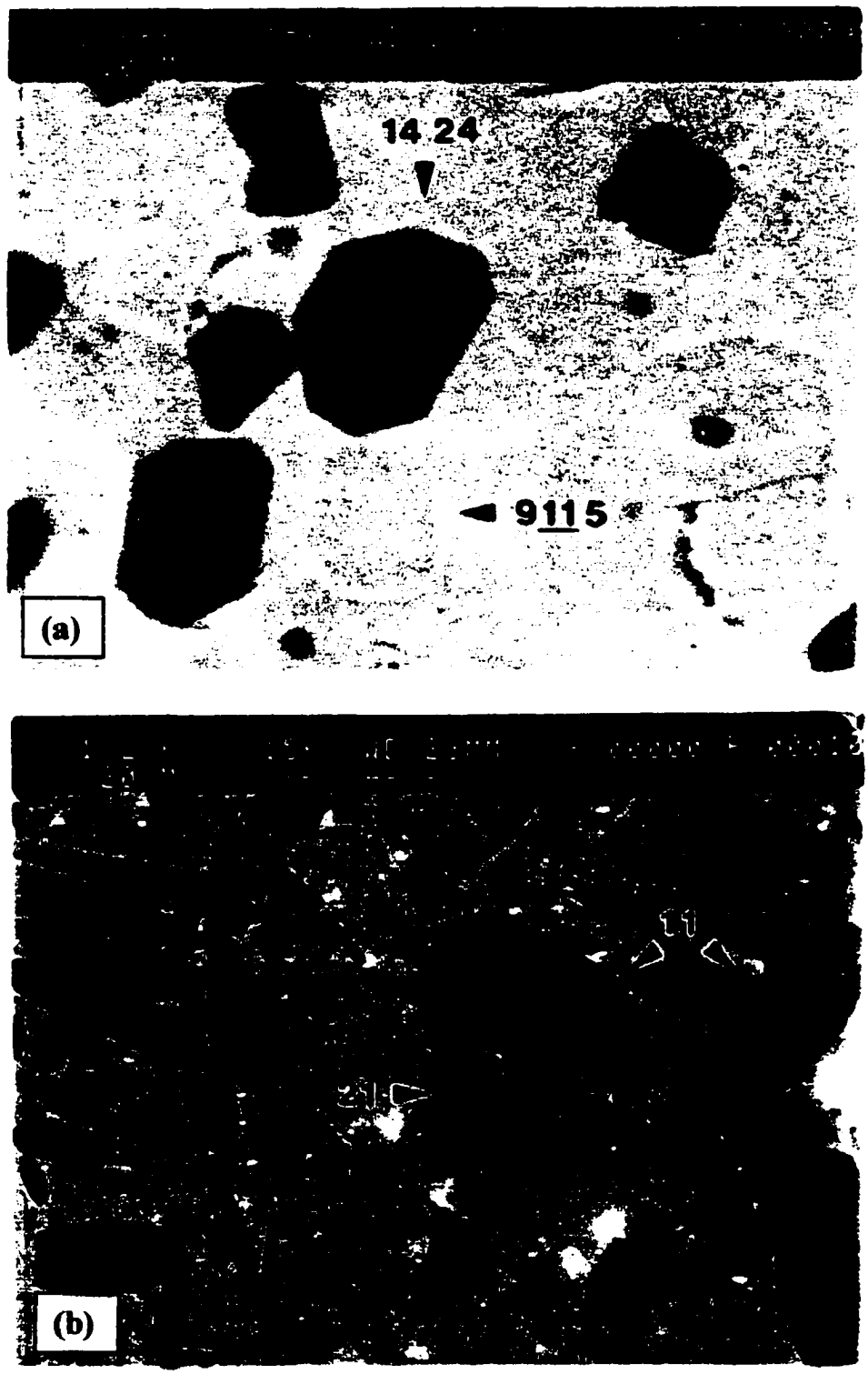


Figure 4. SEM micrographs of oil quenched samples. (a) 912°C at 1 bar $O_2$, (b) 944°C at 1 bar $O_2$, (c) 973°C at 1 bar $O_2$, and (d) 850°C at 0.01 bar $O_2$.

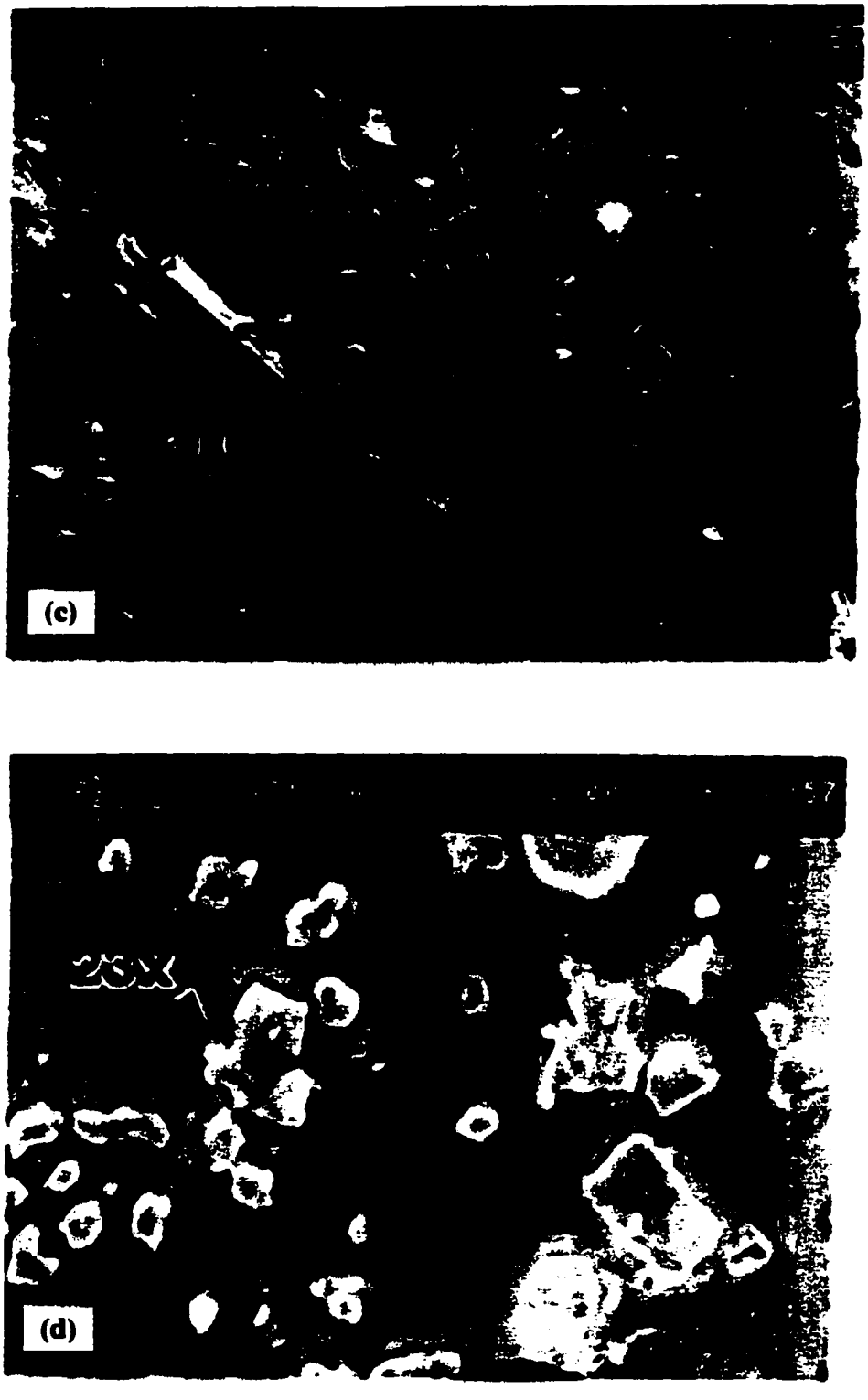


Figure 4. (continued)

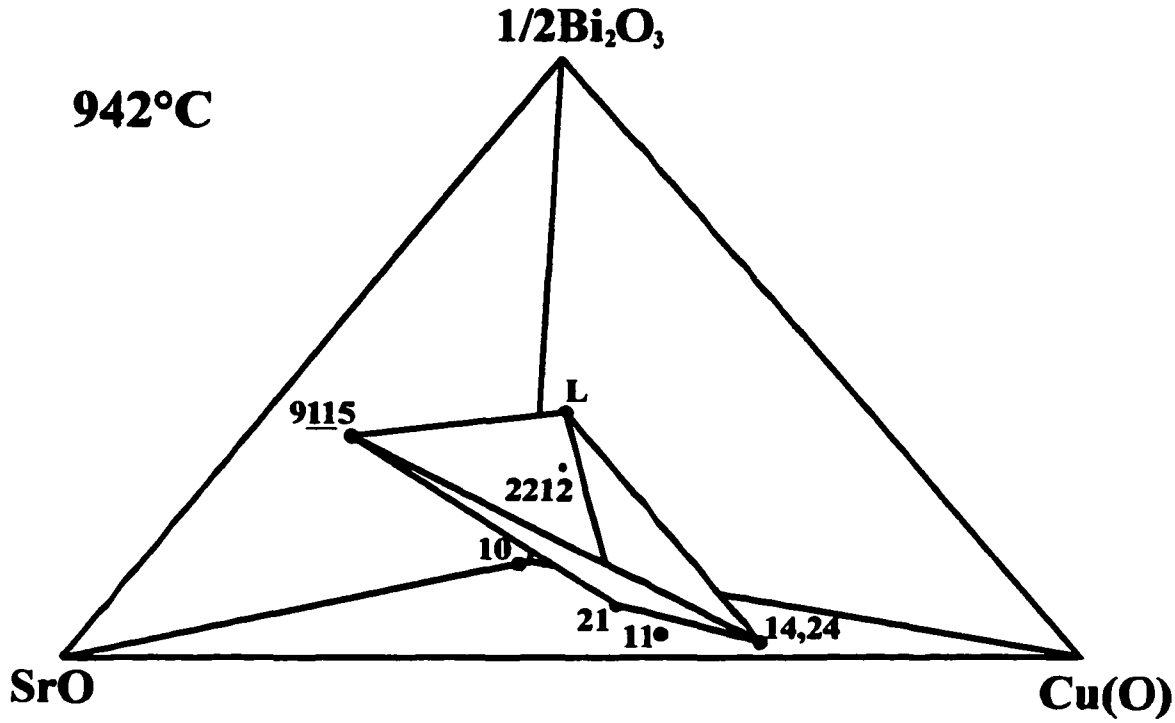


Figure 5. Quaternary phase diagram illustrating the 4 phase tetrahedron which contains the Bi2212 composition at 942°C at 1 bar $O_2$.

at which these reactions occur. In the Ag free system (11), (21), (9$\underline{1}$15), and liquid remain in equilibrium until 960°C. At this point the liquid composition is close to the plane formed by (9$\underline{1}$15), (21), and Bi2212. The (11) slowly dissolves as the liquid composition nears this plane and disappears when they intersect, leaving (9$\underline{1}$15), (21), and liquid in equilibrium. The (9$\underline{1}$15) melts soon after this, shifting the liquid composition onto the plane formed by (21), (10), and Bi2212 causing (10) to begin nucleating from the liquid. The (10) is nearly cubical and rarely grows above 10μm on a side (Figure 4c). The addition of Ag seems to lower the temperature at which the (10) nucleates so that there now exists a phase region in which (9$\underline{1}$15), (11), (21), (10), and liquid are in equilibrium. The addition of Ag also seems to effect the stability of each of the equilibrium solid phases differently, causing slight modifications in the decomposition pathway of Bi2212. The decomposition temperatures of the (11) and (21) are depressed to a greater extent than that of the (9$\underline{1}$15) in the presence of Ag. With 10 wt.% Ag added, the decomposition temperature of (9$\underline{1}$15) is depressed by about 10°C, while the (11) is depressed by 20°C and the (21) by at least 40°C. As a result, there now exists a phase region in the 10 wt.% Ag system in which (9$\underline{1}$15), (10), and liquid are in equilibrium. In the Ag free system the (21) and (10) remain in equilibrium with the liquid up to 992°C. Based on the SrO-CaO-CuO phase diagram one would expect the (21) to decompose next followed by the (10)[44]. No attempt was made to study the system at temperatures above 1000°C, and it is expected that the final liquidus is well in excess of this temperature.

The liquid composition of the partial melt could not be determined by EDS analysis. The quench rate of the samples was not sufficient to prevent the liquid from crystallizing along a compositional gradient. As a result, the liquid crystallized in a progressively finer grained eutectic structure. On the scale of the EDS interaction volume only the last liquid to crystallize was homogeneous enough to give a reproducible composition. It was found that this final liquid tended toward the same composition independently of the temperature the partial melt was quenched from. This suggests the existence of a quaternary eutectic point in the $1/2Bi_2O_3$-SrO-CaO-CuO system. In order to get a picture of the evolution of the liquid composition, the volume fraction of equilibrium phases at a number of temperatures was estimated and a series of mass balance equations were solved to determine the composition

of the partial melt. Figure 6 shows the liquid path with increasing temperature. The $1/2Bi_2O_3$-CaO-(Sr,Cu)O projection was used as the Sr/Cu ratio of the liquid remains nearly constant. Although the exact curvature can only be guessed, the liquid phase region boundaries of the ternary isopleths have been drawn to fit a number of known points, the liquid composition of the partial melt as determined by mass balance and the isothermal intersections of the liquidus lines as reported in the BiO-SrO[19], BiO-CaO[34], BiO-CuO[108], CaO-CuO[44], and SrO-CuO[19] binary systems.

A DTA scan of Bi2212 in 100% $O_2$ is shown in Figure 7. The positions of the thermal events are consistent with the drop tube data. The first endotherm has an onset of 899°C and clearly corresponds with the melting of Bi2212. The second event has an onset of 936°C and seems to correspond with the melting of the (14,24) phase. The next event is quite broad and is probably the sum of at least two events. The drop tube experiments suggest that the (11) and (9$\underline{1}$15) phases completely melt within approximately 5°C of each other between 960°C and 966°C, which could easily account for the third broad endotherm with an onset of 954°C. Due to thermal gradients and a finite quenching rate, the maximum temperature of the drop tube experiments only approximates the temperature of the DTA events.

**21% $O_2$**

Isothermal cuts of a pseudo-ternary phase diagram have been constructed for each of the major phase regions in 21% $O_2$ (Figure 8). The first peritectic reaction, Bi2212 --> (11) + (9$\underline{1}$15) + L, occurs at 887°C. At this lower oxygen partial pressure, the peritectic decomposition temperature of (14,24) must be depressed below that of Bi2212 so that (11) replaces (14,24) in the first peritectic reaction. By 900°C, (21) has begun to nucleate from the liquid. Again, it is important to understand that the (9$\underline{1}$15)-(11)-(21)-L four phase region represented in the ternary is the projection of a four phase tetrahedral volume in the four component system. The (9$\underline{1}$15) completely dissolves by 925°C and we enter a region in which (11), (21), and liquid are in equilibrium. As the temperature increases, the (11) slowly dissolves. By 937°C, the (11) has completely gone and (10) begins to nucleate from the liquid. The (21) then begins to dissolve while the (10) continues to nucleate. By 965°C the (21) has disappeared leaving just (10) and liquid. The size and shape of the second phases do

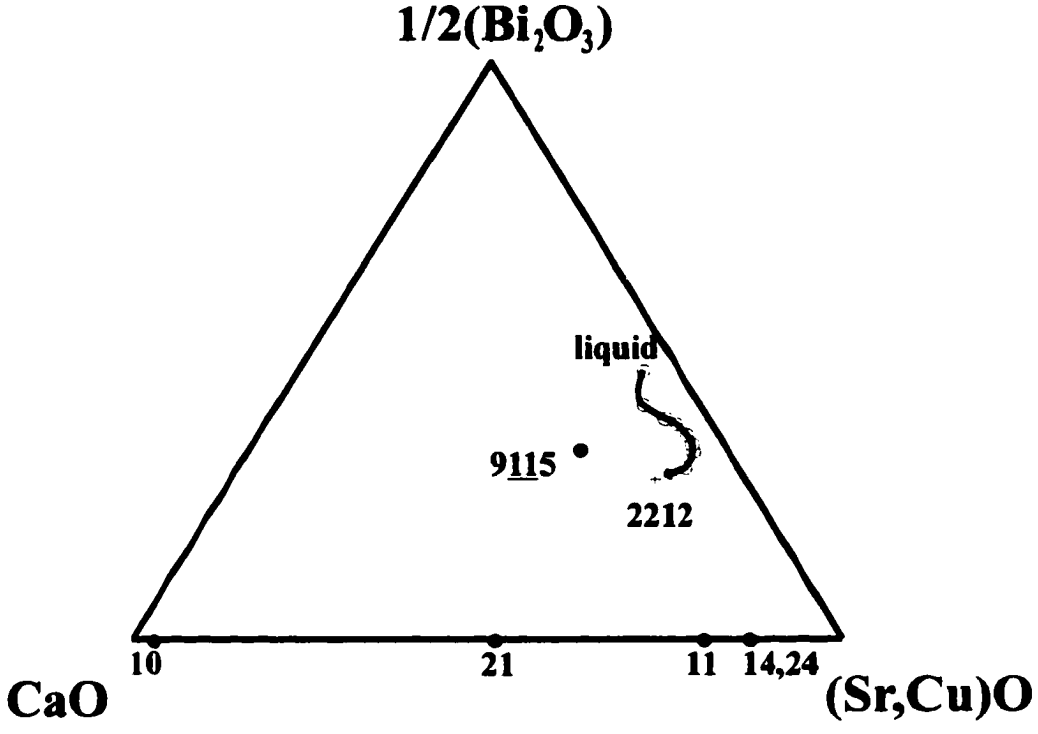


Figure 6. The evolution of the partial melt composition with increasing temperature at 1 bar $O_2$.

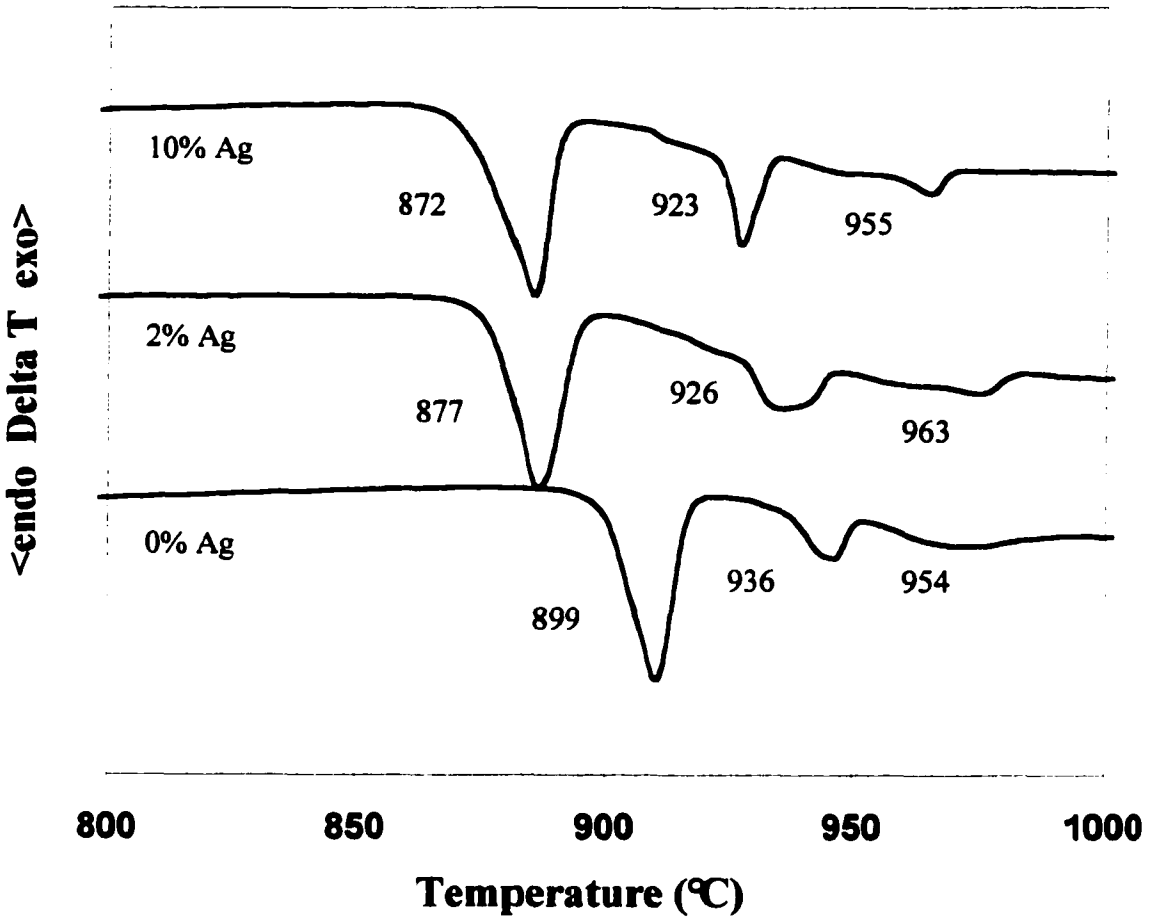


Figure 7. Thermal analysis of Bi2212 with 0, 2, and 10 wt.% Ag added at 1 bar $O_2$.

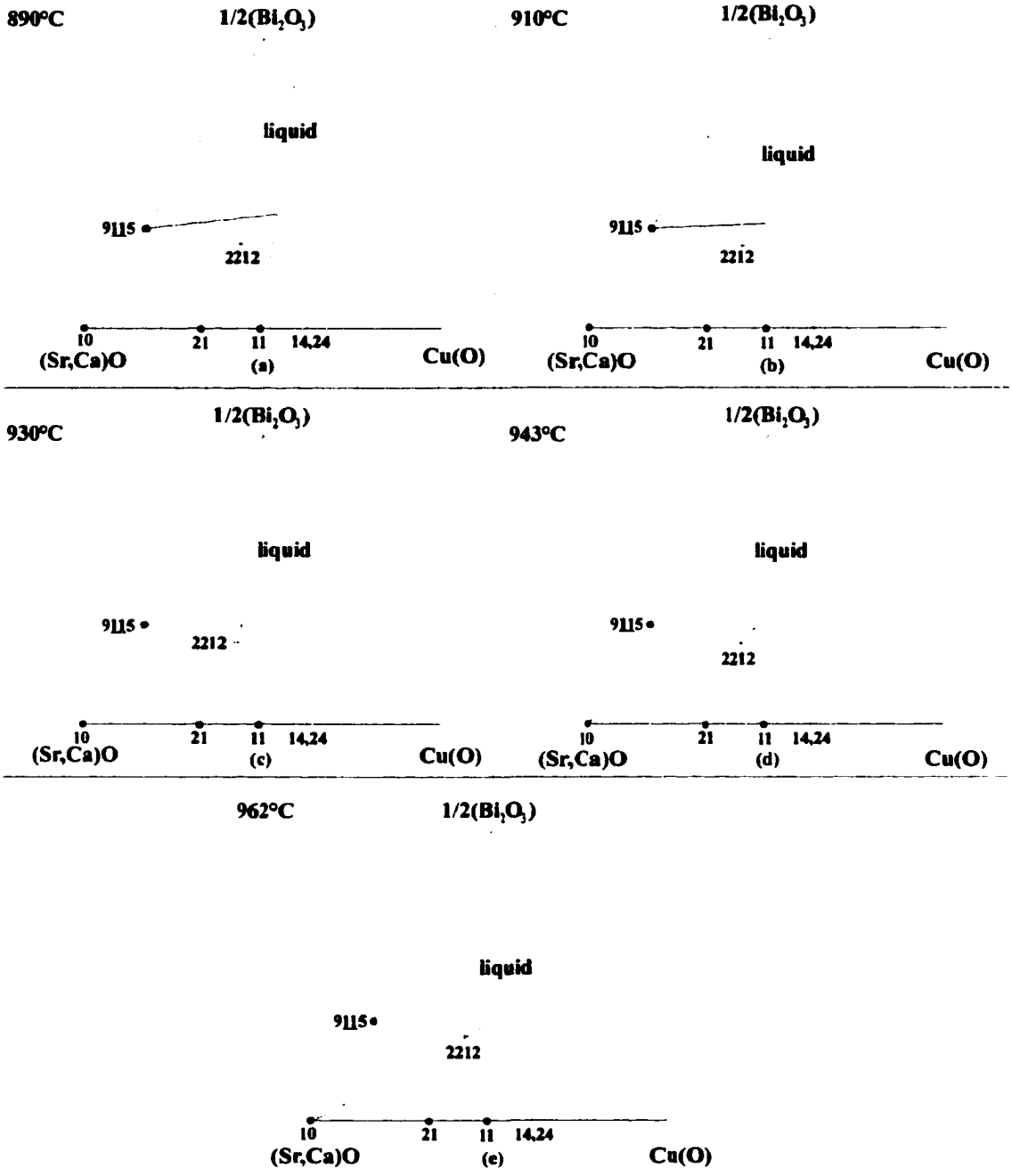


Figure 8. A series of pseudo-ternary phase diagrams illustrating the decomposition pathway of Bi2212 in 21% $O_2$.

not vary significantly from what was observed in the 100% $O_2$ samples. The effect of Ag addition is very similar to that in the 100% $O_2$ system. The first peritectic reaction is depressed to 871°C with 2 wt.% Ag and 867°C with 10 wt.% Ag added. Again, the presence of Ag seems to have a much greater effect on the stability of the (11) and (21) than on the (9$\underline{1}$15), so that with the addition of 10 wt.% Ag the decomposition order of (9$\underline{1}$15) and (11) switches creating a new phase region in which (9$\underline{1}$15), (21), (10), and liquid are in equilibrium. The nucleation temperature of (10) is lowered by 30°C with 10 wt.% Ag added which also causes slight modifications in the decomposition pathway.

**1% $O_2$**

Isothermal cuts of a pseudo-ternary phase diagram have been constructed for each of the major phase regions in 1% $O_2$ (Figure 9). The first peritectic reaction, Bi2212--> (11) + (21) + 23x + L, occurs at 845°C. At this low oxygen partial pressure, the (9$\underline{1}$15) is no longer stable and is replaced by the 23x. The 23x grows to a much larger size than the (9$\underline{1}$15) and has a more cubical shape (Figure 4d). The (10) begins to nucleate from the liquid soon after the first peritectic reaction. Because of the small size and amount of (10), a polished cross section may not contain any even though it does exist in the sample. The (10) was observed at temperatures as low as 860°C. By 880°C the (11) has completely dissolved, leaving 23x, (21), and (10) in equilibrium with the liquid. By 890°C the (21) has disappeared as well leaving 23x and (10) in equilibrium with the liquid. The 23x is retained until it melts somewhere between 910°C and 920°C. Again, the (10) remains stable until the liquidus is reached. The addition of Ag has less of an effect on the decomposition pathway of Bi2212 at this lower $PO_2$. The first peritectic reaction is depressed by only 11°C with 10 wt.% Ag added compared to 27°C at 1 bar $PO_2$. In fact, the reaction order is identical for 0, 2, and 10 wt.% Ag samples.

Table 6 summarizes the decomposition pathway of Bi2212 with respect to $PO_2$ and Ag content. Phase regions marked with an asterisk were not directly observed but are expected to exist due to thermodynamic considerations.

**Effect of carbon**

It has been suggested that Ag alone does not have any effect on the decomposition temperature of Bi and Tl containing superconductors, but C together with Ag is necessary to

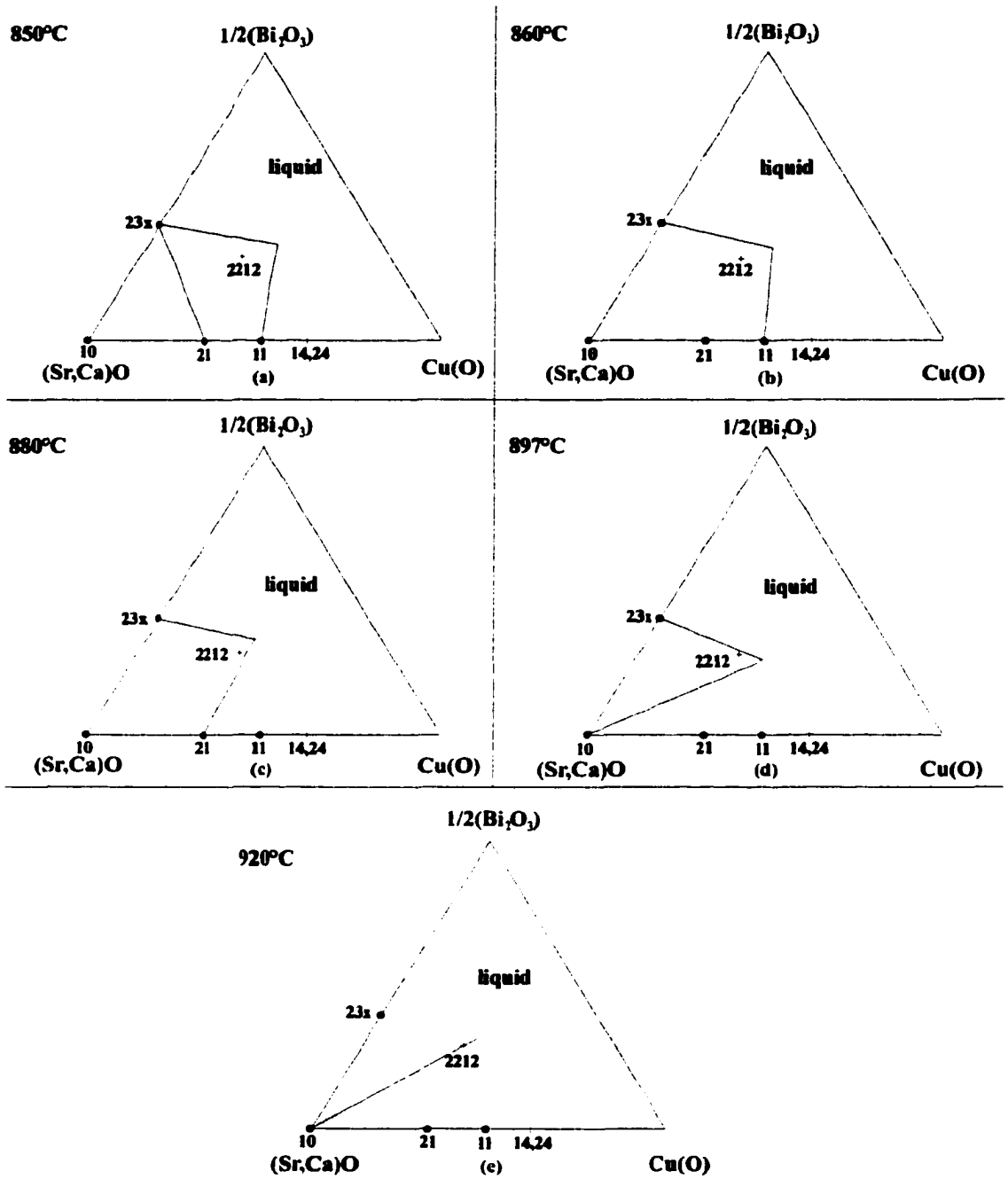


Figure 9. A series of pseudo-ternary phase diagrams illustrating the decomposition pathway of Bi2212 in 1% $O_2$.

Table 6. Summary of decomposition pathways with Ag content and $PO_2$.

| $PO_2$ | 0% Ag | 2% Ag | 10% Ag |
|---|---|---|---|
| 100% $O_2$ | | | |
| | Bi2212 --> | Bi2212 --> | Bi2212 --> |
| | (14,24)+(9115)+L --> | (14,24)+(9115)+L --> | (14,24)+(9115)+L --> |
| | (14,24)+(9115)+21+L --> | (14,24)+(9115)+21+L --> | (14,24)+(9115)+21+L --> |
| | (9115)+11+21+L --> | (9115)+11+21+L --> | (9115)+11+21+L --> |
| | (9115)+21+L --> | (9115)+11+21+10+L --> | (9115)+11+21+10+L --> |
| | 21+10+L --> | (9115)+21+10+L --> | (9115)+21+10+L --> |
| | *10+L | 21+10+L --> | (9115)+10+L --> |
| | | *10+L | 10+L |
| 21% $O_2$ | | | |
| | Bi2212 --> | Bi2212 --> | Bi2212 --> |
| | (9115)+11+L --> | (9115)+11+L --> | (9115)+11+L --> |
| | (9115)+11+21+L --> | (9115)+11+21+L --> | (9115)+11+21+L --> |
| | 11+21+L --> | *(9115)+11+21+10+L --> | *(9115)+11+21+10+L --> |
| | 21+10+L --> | 11+21+10+L --> | (9115)+21+10+L --> |
| | 10+L | 21+10+L --> | 21+10+L --> |
| | | 10+L | 10+L |
| 1% $O_2$ | | | |
| | Bi2212 --> | Bi2212 --> | Bi2212 --> |
| | 23x+11+21+L --> | 23x+11+21+L --> | 23x+11+21+L --> |
| | 23x+11+21+10+L --> | 23x+11+21+10+L --> | 23x+11+21+10+L --> |
| | 23x+21+10+L --> | 23x+21+10+L --> | 23x+21+10+L --> |
| | 23x+10+L --> | 23x+10+L --> | 23x+10+L --> |
| | 10+L | 10+L | 10+L |

* These phase regions were not directly observed but are expected to exist due to thermodynamic considerations.

lower the melting temperature[109]. A high temperature x-ray diffraction study by Misture, *et al.* demonstrated that Bi2212 with 1600 ppm carbon showed no depression of the melting temperature with the addition of 20 wt.% Ag [110]. The possibility that the suppression in the peritectic decomposition temperature could be due to the combined effect of C and Ag prompted further study into the effect C content may have on the peritectic decomposition temperature of Bi2212.

The material used for the previous study on the effect of Ag and $PO_2$ on the decomposition of Bi2212 was analyzed for C content. The Ag free material contained 270 ppm C and the 10 wt.% Ag added material contained 1470 ppm. In order to determine whether C had any role in the observed depression of the melting reaction temperatures in the Ag added material, some of the original material with and without Ag was heat treated in flowing $O_2$ at 800°C for 3 days. Analysis of this heat treated material showed a C content of 30 ppm for the Ag free material and 81 ppm for the 10% Ag material. This low C material was then exposed to air and water saturated air for a controlled amount of time and re-analyzed for C content (Table 7). The presence of $H_2O$ in the atmosphere increases the rate at which Bi2212 picks up C for both the Ag and Ag free material. The presence of Ag,

Table 7. The C content of samples used in this study.

| | C content (ppm) | |
|---|---|---|
| sample history | 0% Ag | 10% Ag |
| original material | 270 | 1470 |
| 800°C 72hrs | 30 | 81 |
| 3 days in $H_2O$ saturated air | 1770 | 990 |
| 3 weeks in $H_2O$ saturated air | 6980 | 1030 |
| 3 days in air | 111 | 273 |

though, lowers the rate at which C is picked up, which is directly opposite to the effect observed in low humidity. It is possible that $H_2O$ facilitates the decomposition of Bi2212 and the formation of $CaCO_3$ and $SrCO_3$ [111], although the combined role of Ag and $H_2O$ in this reaction is not known.

Thermal analysis was performed for high (> 1000 ppm) and low (< 100 ppm) C levels in 1.00, 0.21 and 0.01 bar $PO_2$ for Bi2212 and Bi2212 + 10% Ag added material (Figure 10). In 1.00 bar $O_2$, a 27°C depression with the addition of 10% Ag was previously observed. With the C content lowered to below 100 ppm, a depression of 28°C was observed. These results suggest that down to at least 70 ppm C, the addition of Ag significantly depresses the melting temperature of Bi2212, but the effect of C content up to 1500 ppm is negligible. Lowering the C content of Bi2212 and Bi2212 + 10% Ag did produce a slight increase in decomposition temperature over a wide range in $PO_2$ when controlling for Ag content (~ 3°C). Regardless of the C content of the samples, 10% Ag added material had significantly lower onsets for the peritectic decomposition, depending on the $PO_2$ (Table 8). When controlling for Ag content but changing $PO_2$, the C effect on the peritectic decomposition temperature is slightly more pronounced with decreasing $PO_2$. This is in contrast to that of Ag, where lowering the $PO_2$ minimizes the effect of Ag on the peritectic decomposition. The slight increase in the C effect with lowering $PO_2$ can be attributed to a highly reactive surface layer. It is speculated that some recombination of the carbonates is occurring during the DTA runs. This effect would be more pronounced with higher $PO_2$ [112].

Table 8. Peritectic decomposition temperatures for various C, Ag, and $PO_2$ concentrations are given in the first four columns. The last two columns show the range in differences in the peritectic decomposition for Ag (holding C fixed) and for C (holding Ag fixed).

| | 0% Ag | | 10% Ag | | ΔT (°C) | |
|---|---|---|---|---|---|---|
| $PO_2$ (bar) | Low C (°C) | High C (°C) | Low C (°C) | High C (°C) | Ag | C |
| 1.00 | 905 | 902 | 877 | 877 | 25-28 | 0-3 |
| 0.21 | 893 | 889 | 874 | 873 | 16-19 | 1-4 |
| 0.01 | 853 | 850 | 844 | 839 | 9-11 | 3-5 |

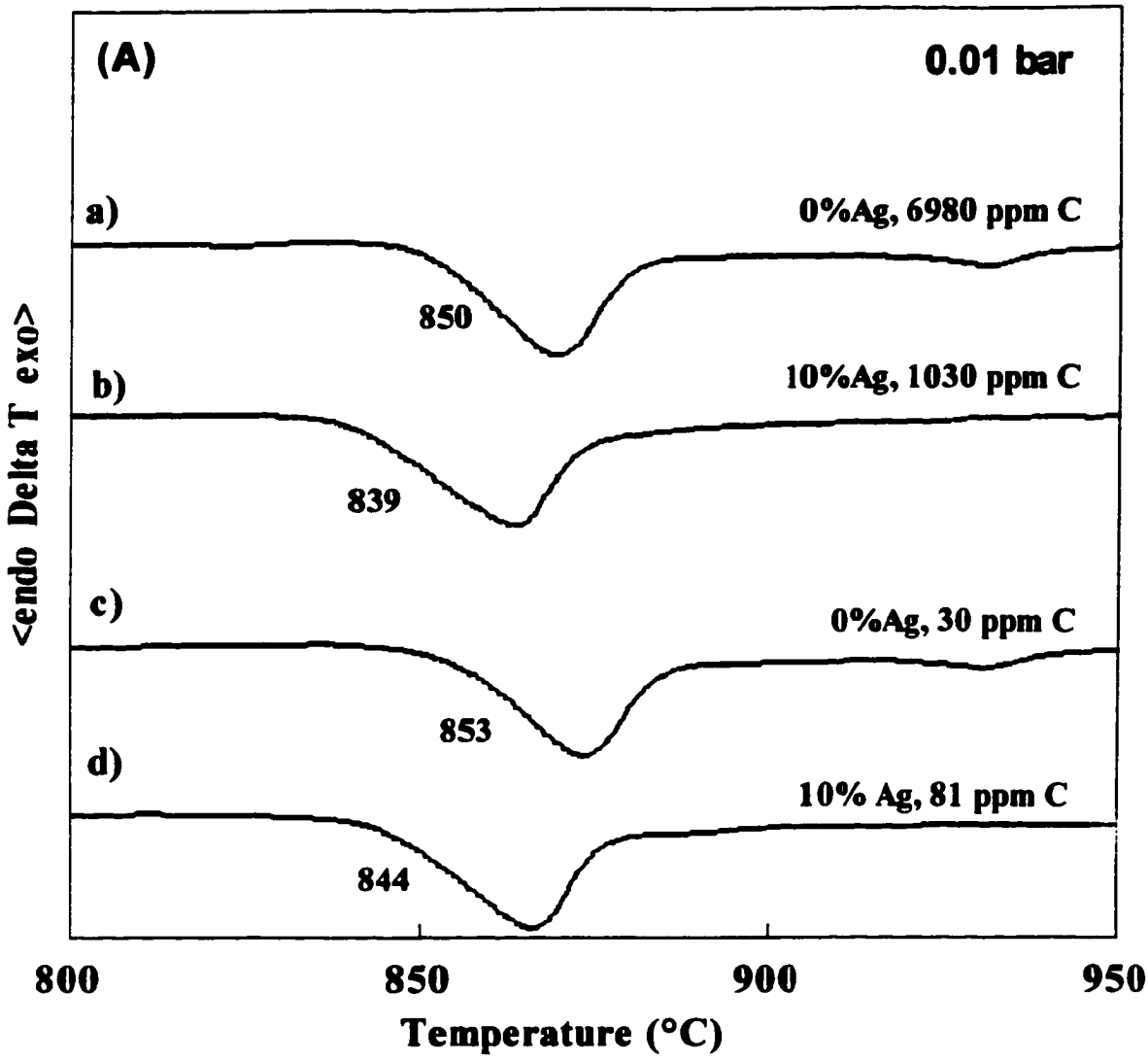


Figure 10. DTA scans for Bi2212 with and without Ag in (A) 0.01, (B) 0.21, and (C) 1.00 bar oxygen. Scans a) and b) are for the higher C containing samples, while c) and d) are for the low C samples.

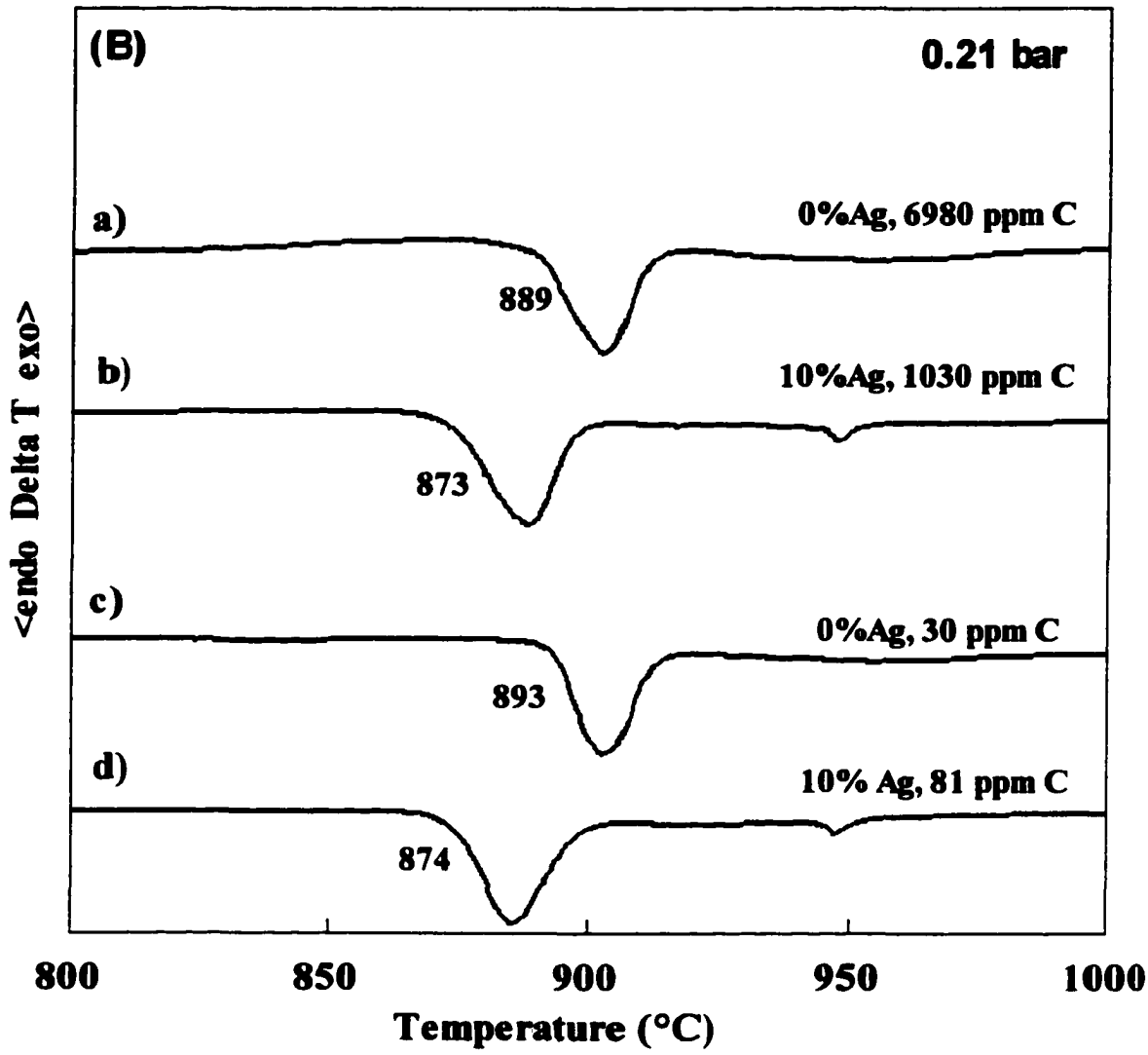


Figure 10. (continued)

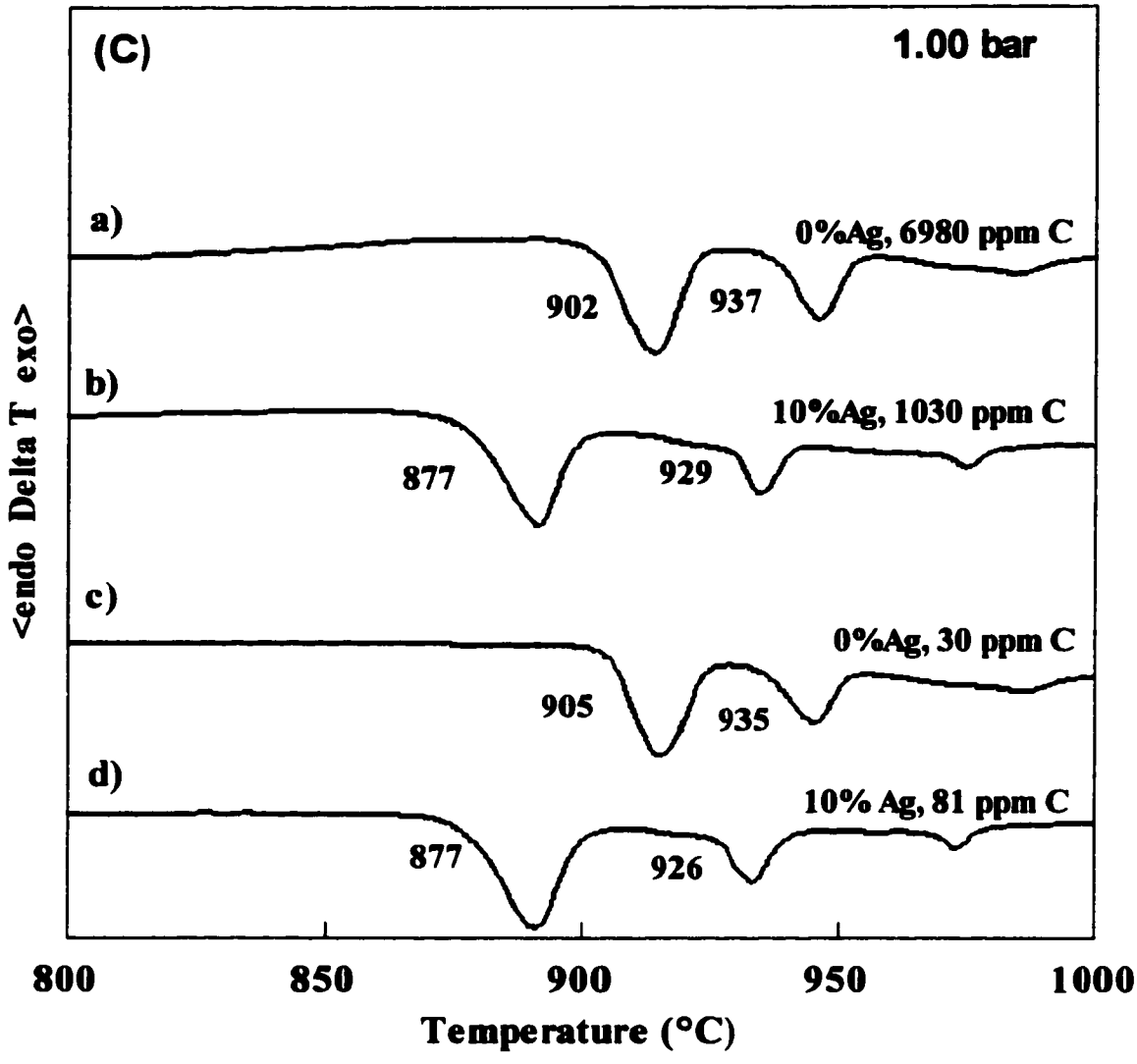


Figure 10. (continued)

It should be noted that only one composition in the solid solution range of Bi2212 was analyzed. This composition is at the Ca/Sr rich end of the solid-solution for Bi2212 [81]. Thus small losses of Ca or Sr to carbonate formation will force the bulk composition further into the solid-solubility region. In the case where compositions are choosen near to the Bi rich side of the solubility limit, a small loss of Ca/Sr will force the bulk composition out of the Bi2212 stability regime. Once the bulk composition is outside the solid-solubility region, numerous decomposition reactions are possible, but all are lower in temperature than the Bi2212 peritectic decomposition.

**Thermal analysis**

Although the drop tube experiments were only done in 100%, 21%, and 1% $O_2$, differential thermal analysis was done at a number of intermediate oxygen partial pressures. Figure 11 shows a plot of 1/T (where T is the onset temperature of the first peritectic reaction) versus the ln of the oxygen partial pressure. In this representation, the slope is equal to the change in enthalpy of the system during the first peritectic reaction. One would expect a discontinuous change in $\Delta H$ as the decomposition products alter with varying $PO_2$. The drop tube experiments suggest that such discontinuities must exist between 100% $O_2$ and 21% $O_2$ and between 21% $O_2$ and 1% $O_2$. By fitting and extrapolating lines to the data, one finds a discontinuity in slope at approximately 33% $O_2$. This would correspond to the $PO_2$ boundary at which the first peritectic decomposition products switch from (14,24), (9$\underline{1}$15), and liquid to (11), (9$\underline{1}$15), and liquid. Indeed, this must be the oxygen partial pressure at which the melting temperature of the (14,24) drops below that of the 2212. There does not seem to be any shift in slope, though, between 21% $O_2$ and 1%$O_2$. As the $PO_2$ is lowered, the actual $PO_2$ seen by the sample is difficult to determine as Bi2212 releases oxygen during melting. As a result, data points at these lower oxygen partial pressures may be unreliable. A sample dropped in 10% $O_2$ contained 23x, (11), and (21) which suggests that the (9$\underline{1}$15) becomes unstable somewhere between 21% and 10% $O_2$.

**Effect of Ag on oxygen activity**

The effect of Ag on the oxygen content of the Bi2212 melt was examined by monitoring the oxygen partial pressure of the outlet gas during heating to 1000°C. An inlet stream of 1% $O_2$ was used and the total oxygen released by the sample was calculated by the

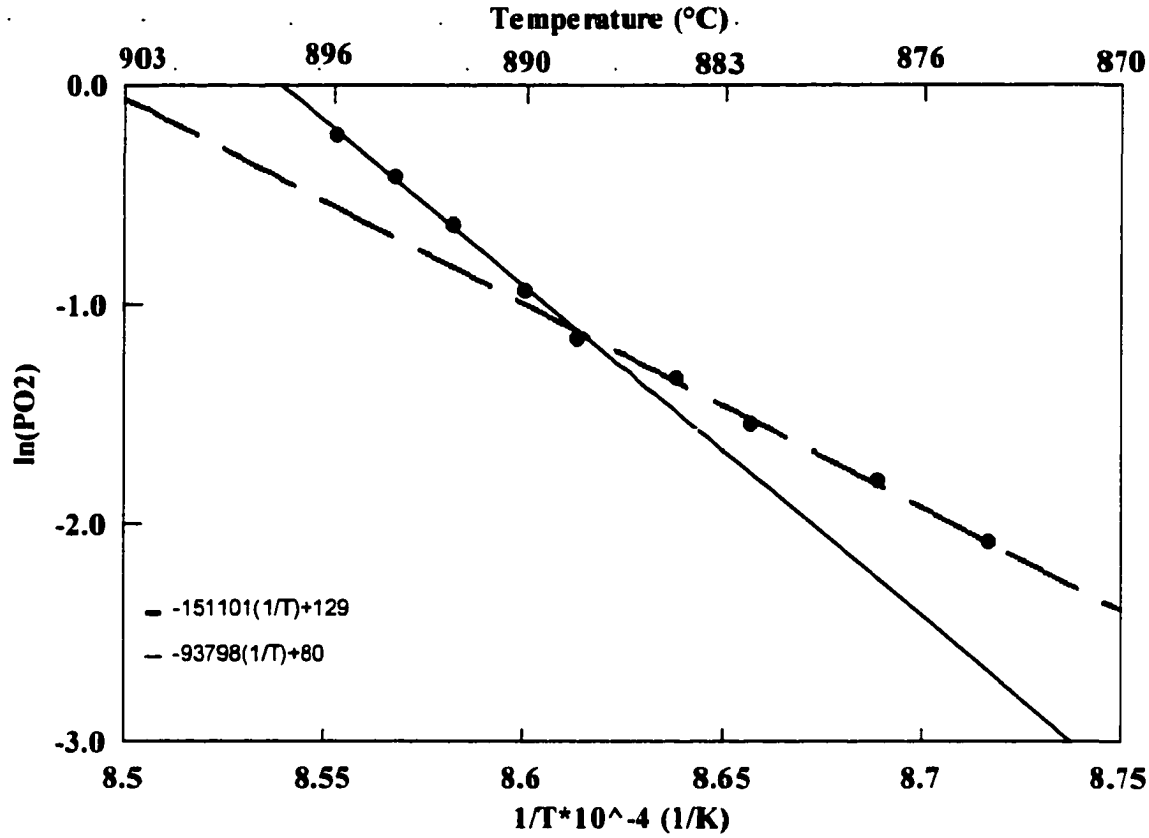


Figure 11. The plot of ln[P($O_2$)] versu 1/T shows a discontinuity in slope at approximately 0.33 bar $O_2$.

integrated intensity of the observed $O_2$ peak. The final mole percentage of $O_2$ released was normalized to take into account the various Ag contents. Figure 12 shows the change in $O_2$ loss with weight percent Ag. At 1000°C the samples were nearly fully liquid with just a small amount of CaO in equilibrium with the melt. As the samples were all fully oxygenated, the amount of $O_2$ released during melting should give an indication of the $O_2$ content of the liquid. The data suggests that the addition of Ag initially increases the $O_2$ content of the liquid, which reaches a maximum at approximately 6 wt. % Ag. Further addition of Ag causes the $O_2$ content of the melt to decrease again, until it has nearly regained the Ag free level at 20 wt. % Ag. This behavior may be explained in terms of the dependence of the activity coefficient of $O_2$ on Ag content. The significance of this behavior is not yet clear, as the chemical activity of a particular species may be a complex function of composition in a multicomponent system such as this. However, it does suggest a strong link between $O_2$ activity and the solubility of Ag in the ceramic liquid. This moderating influence of Ag on the $O_2$ activity may be responsible for the strong influence of Ag in depressing the peritectic decomposition temperature. In many ways the effect of Ag addition seems equivalent to effectively lowering the $PO_2$, but there is a clear difference in these effects in that Ag shows no sign of destabilizing the high oxygen content phases such as (14,24) which are removed from the phase equilibria with lowering $PO_2$.

**Discussion**

The disagreement between the results presented here and those previously reported are significant and need to be addressed. Most of the high temperature x-ray diffraction work has been done in air and the results suggest that the first peritectic reaction is Bi2212--> (11) + L[104,113]. The (9$\underline{1}$15) is not observed at any point along the decomposition path. In the melt, the position of the solid phases relative to the surface of the liquid during in situ XRD experiments will depend on their relative densities. If the (9$\underline{1}$15) has a higher density than the liquid it will sink to the bottom and may be below the penetration depth of an x-ray beam. This may explain why the (9$\underline{1}$15) has only been observed in quenching experiments. The Cu free phase reported in quenching experiments has been labeled 24x[85] or (9$\underline{1}$15)[102]. In fact, a variety of (Sr,Ca):Bi ratios ranging from 1.71 to 2.33 have been reported with similar XRD patterns indexed to a monoclinic unit cell[113,53,114,115]. The atomic positions and

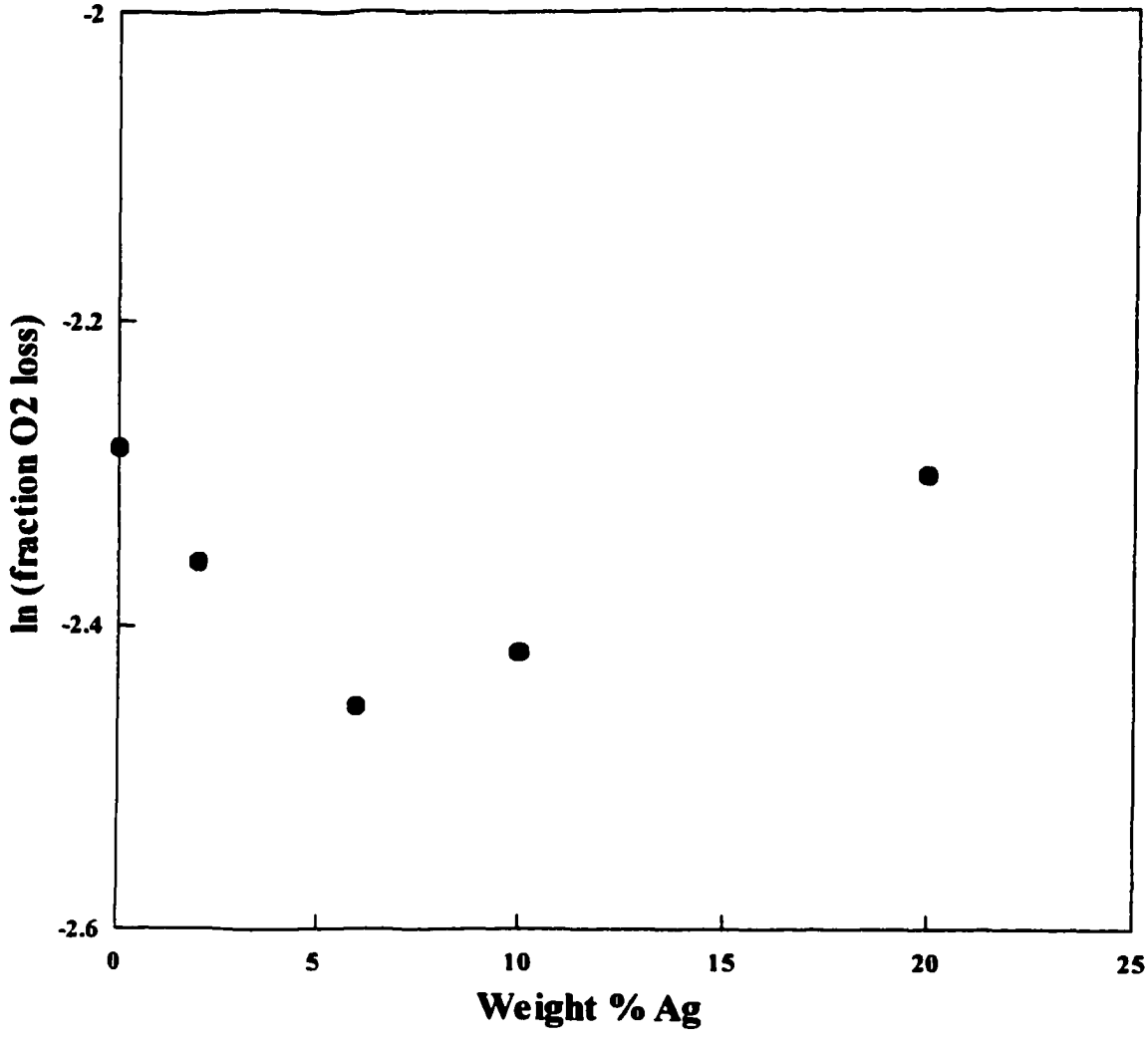


Figure 12. Normalized $O_2$ loss as a function of Ag content during melting of Bi2212 in 0.01 bar $O_2$.

occupancies of the unit cell have not been solved in any of these studies. All of these phases are very close in composition and slight deviations in EDS standardization could easily cause confusion. Standardless semi-quantitative EDS analysis was not accurate enough to differentiate between these compositions. Microprobe analysis suggested that the true composition of this phase was closer to (9115), although there seemed to be approximately 3 mole % Cu substituting for Sr. It has been suggested that the (9115) phase is really the 24x with some solubility of Cu for Sr or Ca[116]. It seems likely that this Cu free phase has a solid solution range that extends not only along the Sr-Ca direction, but also along the Bi-(Sr,Ca) and even Cu-(Sr,Ca) directions. In this case, the various nomenclatures used in the literature are misleading and must remain so until the exact structure and solubility range of this phase is determined. It should also be noted that a variety of compositions have been used as starting materials in the literature. The dependence of the melting pathway on exact composition has not been examined well, and may play an important role in melt processing. The range of compositions used within the Bi2212 stability region is quite large and may explain some of the conflicting results reported in the literature.

Of the results reported in the literature, the quenched tape experiments done by Hellstrom and Zhang are the most consistent with our results. They reported that (14,24) and 24x (referred to here as (9115)) were the first decomposition products at 100% and 50% $O_2$ and that the (14,24) was replaced by (11) by 30% $O_2$[85]. This is consistent with the value of 33% for the transition between (14,24) and (11) suggested by the DTA results. At lower oxygen partial pressures, though, there is some disagreement with our results. At 7.5% $O_2$, Hellstrom and Zhang report that 24x, (11), and (21) are the first solid phases to form in the partial melt[103]. Our results suggest that the (9115) is replaced by 23x by 10% $O_2$. At 1% $O_2$, Hellstrom and Zhang report that (21) and 23x are the first decomposition products, while our results show that the (11) also forms during the first peritectic reaction[85]. The (11) was observed in 1%$O_2$ in an earlier quenching experiment done by Hellstrom and Zhang[103]. It should be noted that all samples in their studies were in closed Ag tapes. When monitoring the $PO_2$ of the outgoing gas during thermal analysis in 1% $O_2$, a significant release of $O_2$ can be observed upon the decomposition of Bi2212 (Figure 13). As a result, at lower oxygen

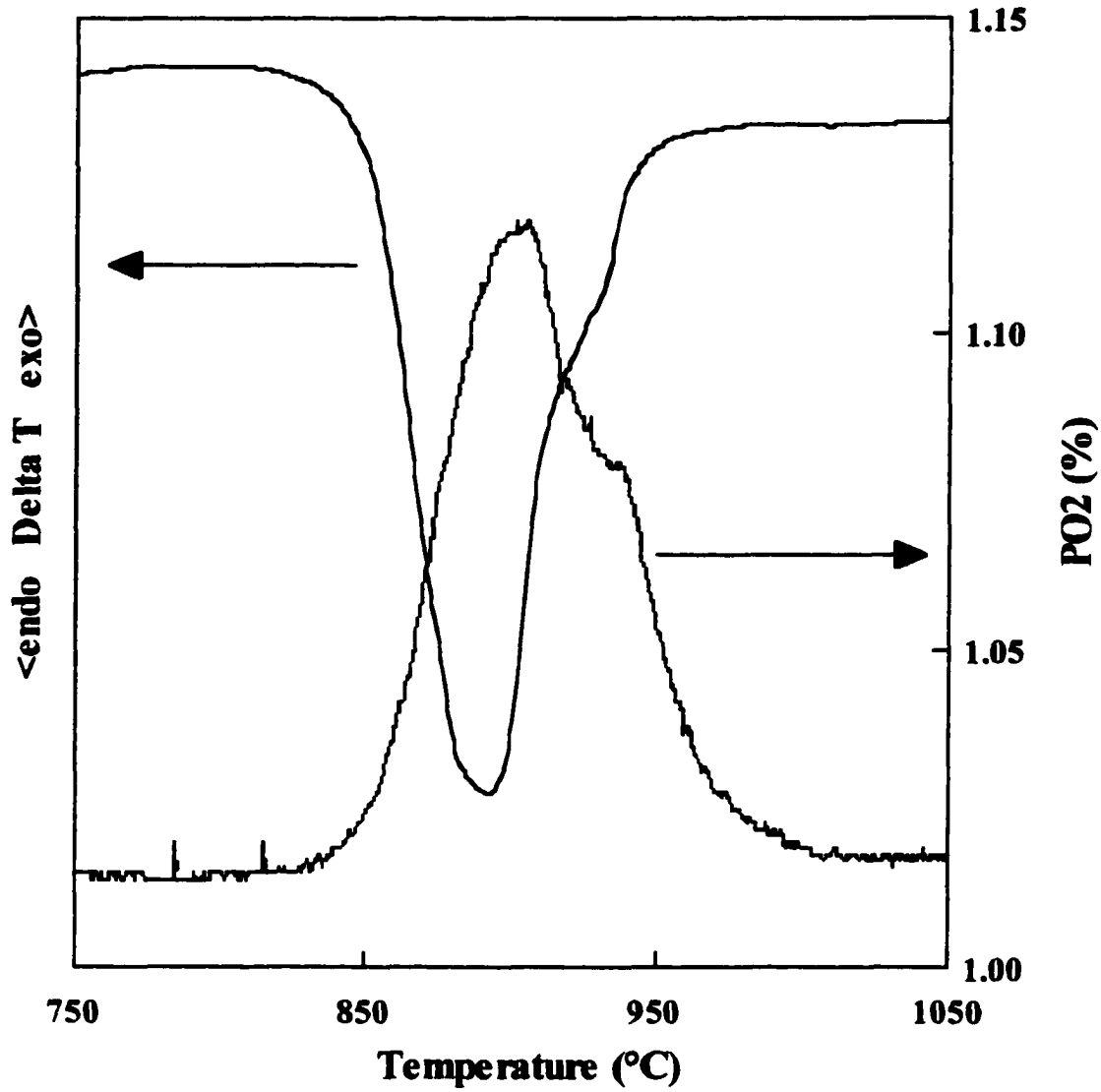


Figure 13. Simultaneous DTA and $PO_2$ measurements demonstrate the evolution of $O_2$ during the decomposition of Bi2212.

partial pressures the actual $PO_2$ seen by the sample could be significantly higher if the oxygen released by the sample does not have time to diffuse through the Ag tape. In addition, the effect of any residual carbon in the ceramic will be heightened as it too would be trapped and effectively increase the $CO_2$ partial pressure observed by the sample.

# CONCLUSIONS

Having mapped out the partial liquid phase regions as a function of $PO_2$ and Ag content, it is natural to examine partial melt processing techniques in light of this information. We should like to understand the relationship between the final microstructure and the processing parameters ($PO_2$, heating and cooling schedule) in terms of the high temperature phase equilibria data collected.

For Ag sheathed Bi2212 tapes melt processed in air, it has been found that the optimum maximum temperature is 885-890°C[117]. It is found that $J_c$ decreases quickly with higher maximum temperatures. It has also been observed that tapes processed at temperatures above 900°C contain large Cu-free phases, and this is likely the cause of the deteriorating $J_c$.

The 9$\underline{1}$15 phase will melt in Ag tapes at 910°-915°C. It is possible that this phase will grow larger when it nucleates on cooling from regions above this temperature. In this case it would be beneficial to remain in the first partial liquid phase region above the solidus to avoid second phase nucleation on cooling.

In general, one would like the crystalline phases in the partial melt to be uniformly distributed and as small as possible. This will minimize diffusion distances and speed homogenization of annealed tapes to single phase Bi2212. In tapes melt processed in air, large (11) grains are often found with sizes comparable to the tape thickness. These grains react slowly, so that even prolonged annealing times are not sufficient for fully removing them. These large grains are disastrous to the current carrying capacity of tapes, so one would like to modify typical processing routes to avoid their formation. From the partial liquid phase equilibria data presented here it is clear that air is not an ideal melt processing environment as the (11) phase will be in equilibrium with the partial liquid when Bi2212 begins to nucleate.

At lower $PO_2$, (21) is stabilized with respect to (11). In 1% $O_2$ there is considerably more (21) than (11) in the melt. The (21) grains form as thin needles and are easier to eliminate during annealing. Unfortunately, though, the 23x phase replaces 9$\underline{1}$15 at this $PO_2$,

and it is observed that 23x grows to a considerable size in the melt. In 100% $O_2$, (14,24) and 9$\underline{1}$15 are the first solid peritectic products during melt processing. Neither of these phases tend to grow as large as the (11) or 23x phases. It would seem, then, that this $PO_2$ range (33-100% $O_2$) should be optimal for producing a homogeneous microstructure in melt processed tapes.

Recently, thermodynamic calculations on the Ag-Bi-Sr-Ca-Cu-O system have been done using the CALPHAD method[118]. This involves modeling of the Gibbs free energy of the known phases, followed by optimization of adjustable parameters based on extracted experimental data, and the generation of model phase diagrams. Table 9 compares the calculated decomposition pathway of Bi2212+10 wt% Ag in 100% $O_2$ with the experimental results from the quenching results presented earlier. There is generally good agreement. Furthermore, the stability of the 9$\underline{1}$15 phase in the partial melt is confirmed by the thermodynamic calculations in opposition to many of the high temperature x-ray diffraction studies. Ideally, though, one would like to confirm the existence of this phase in the partial liquid through in situ measurements. As mentioned earlier, though, this pushes the limits of conventional high temperature diffraction systems. A new approach is necessary to avoid the artifacts associated with conventional designs.

Table 9. Calculated decomposition pathway of Bi2212 with 10 wt% Ag in 100% $O_2$ from Assal[118] compared with experimental results from this work.

| Assal calculations | T(K) | This work | T(K) |
|---|---|---|---|
| Bi2212 → | 1136 | Bi2212 → | 1145 |
| (14,24)+(9$\underline{1}$15)+L | 1157 | (14,24)+(9$\underline{1}$15)+L | 1182 |
| (14,24)+(9$\underline{1}$15)+(21)+L | 1191 | (14,24)+(9$\underline{1}$15)+(21)+L | 1199 |
| (9$\underline{1}$15)+(21)+L | 1195 | (9$\underline{1}$15)+(21)+(11)+L | 1207 |
| (21)+L | 1213 | (9$\underline{1}$15)+(21)+(11)+(10)+L | 1213 |
| (21)+(10)+L | 1297 | (9$\underline{1}$15)+(21)+(10)+L | 1220 |
| (10)+L | 1390 | (9$\underline{1}$15)+(10)+L | 1226 |
| L | | (10)+L | |

# PART II

# HIGH TEMPERATURE POWDER DIFFRACTION USING SYNCHROTRON RADIATION

## INTRODUCTION

Synchrotron radiation has been shown to be an excellent source for high resolution powder diffraction studies. A number of such studies have shown that reliable structural parameters can be extracted from synchrotron data utilizing Rietveld refinement programs[119-123]. Most high temperature powder diffraction studies have focused primarily on qualitative phase analysis. Over the years a number of high temperature diffractometer designs have been reported in the literature[124-127]. None of these designs, however, allow for sample rotation while maintaining a controlled atmosphere and low thermal gradient across the sample, a requirement that is critical for studying how processing parameters affect high temperature phase transformations and structures. The ability to accurately reproduce a variety of processing conditions is necessary in order to assure a reliable correlation between the high temperature diffraction data and the phase equilibria region of interest. Indeed, most high temperature diffraction designs produce a highly artificial sample environment which is often not representative of the actual processing conditions of interest. This is primarily due to the commonly used strip heater design which has been carried over from its use with conventional tube or rotating anode sources. The non-uniform heating geometry of this design produces significant thermal gradients both laterally and longitudinally across the sample. Additionally, the strip heater design does not allow for an easy method of introducing sample rotation, which is critical for achieving powder averaging and quantitative structure factor data.

Thermal expansion of the sample and substrate is also a source of error. In the flat plate Bragg-Brentano geometry a number of geometrical aberrations are introduced as the sample surface deviates from the focusing plane. Thermal expansion during heating will continually shift the sample surface height. This must often be adjusted during the course of sequential data sets, complicating later analysis. For this reason, Debye-Scherrer geometry is preferred for high temperature powder diffraction. With conventional x-ray sources this is often not practical, due primarily to absorption considerations. The use of high energy x-rays from synchrotron sources alleviates this problem and allows for a considerably more robust

furnace design. In addition, Debye-Scherrer geometry allows for a more natural introduction of sample rotation into the furnace design. Figure 14 shows the x-ray absorption length for Bi2212 as a function of x-ray energy. For a typical tube source energy of 8.048 keV ($CuK_\alpha$) the absorption length is on the order of .01 mm. For a reasonable capillary ID of 1 mm this translates to a 99% absorption of the incident beam. Energies in excess of 60 keV are necessary before the absorption length increases to the order of the sample thickness.

The data presented in the following section was collected during a number of experimental runs at two synchrotron sources. Experiments at the Advanced Photon Source (APS) were performed at the SRI-CAT 1-ID undulator beamline. Experiments at the Cornell High Energy Synchrotron Source (CHESS) were performed at the A2 24 pole wiggler beamline.

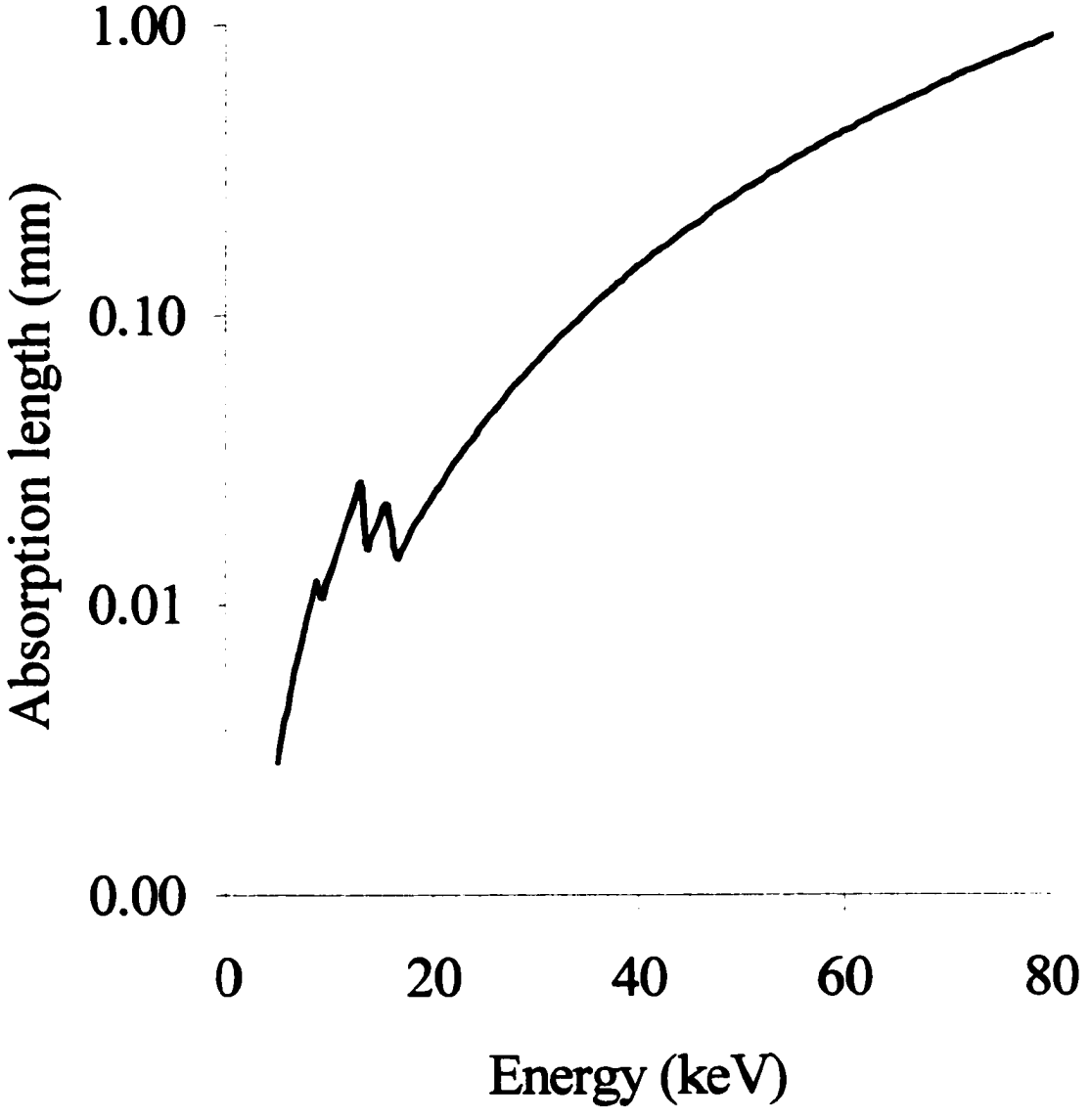


Figure 14. Absorption length for $Bi_2Sr_2CaCu_2O_8$ as a function of x-ray energy.

# EXPERIMENTAL DESIGN

## Furnace design

In constructing a furnace for high resolution diffraction, there are three primary design goals; i) due to the logistics of synchrotron work, it is necessary for the furnace to be compact and portable. It must be easily and quickly mounted and aligned on a standard four circle goniometer. ii) The sample environment must be well controlled and flexible. Thermal gradients must be minimized, and a wide range of temperatures and atmospheres should be achievable. The furnace should also be designed to mimic actual processing conditions that are routinely used in materials preparation. iii) Any sources of error that affect proper structure factor determinations must be addressed to allow for structural refinement. In practice, it is found that incomplete powder averaging is the primary source of error due to the extremely low angular divergence achievable with synchrotron beamlines. As a result, sample rotation must be designed into the furnace in such a way as to not compromise thermal stability or atmosphere control.

The furnace design consists of three basic units; the furnace, an outer frame for mounting and position adjustment, and a magnetically coupled rotating sample mount which attaches to one end of the tube furnace. A schematic of the basic furnace without the sample rotation attachment is shown in figure 15. The furnace is composed of Pt/Pt-10%Rh wire wound onto an $Al_2O_3$ tube. A BeO tube fits inside the $Al_2O_3$ tube and acts as the sample chamber. BeO was chosen for a number of reasons. First, it has a high melting point (2530 °C), low thermal expansion, and good chemical stability, allowing it to be used in a large range of sample environments (up to 1800 K in oxidizing, inert, or reducing atmospheres). Secondly, its low absorption at high x-ray energies provides for uniform thermal insulation surrounding the sample without excessive intensity loss. A control thermocouple placed inside the BeO tube is used to measure the temperature while the set point and ramp rate is remotely controlled with a Eurotherm 808 digital controller. An additional cylindrical layer of alumina-silica (Zircar SALI) insulation surrounds the furnace core, and this in turn is contained in a stainless steel can to complete the basic furnace. A 3mm diameter hole, to pass the incident beam, and a 3mm wide slot, which passes scattered x-rays at angles from 0°

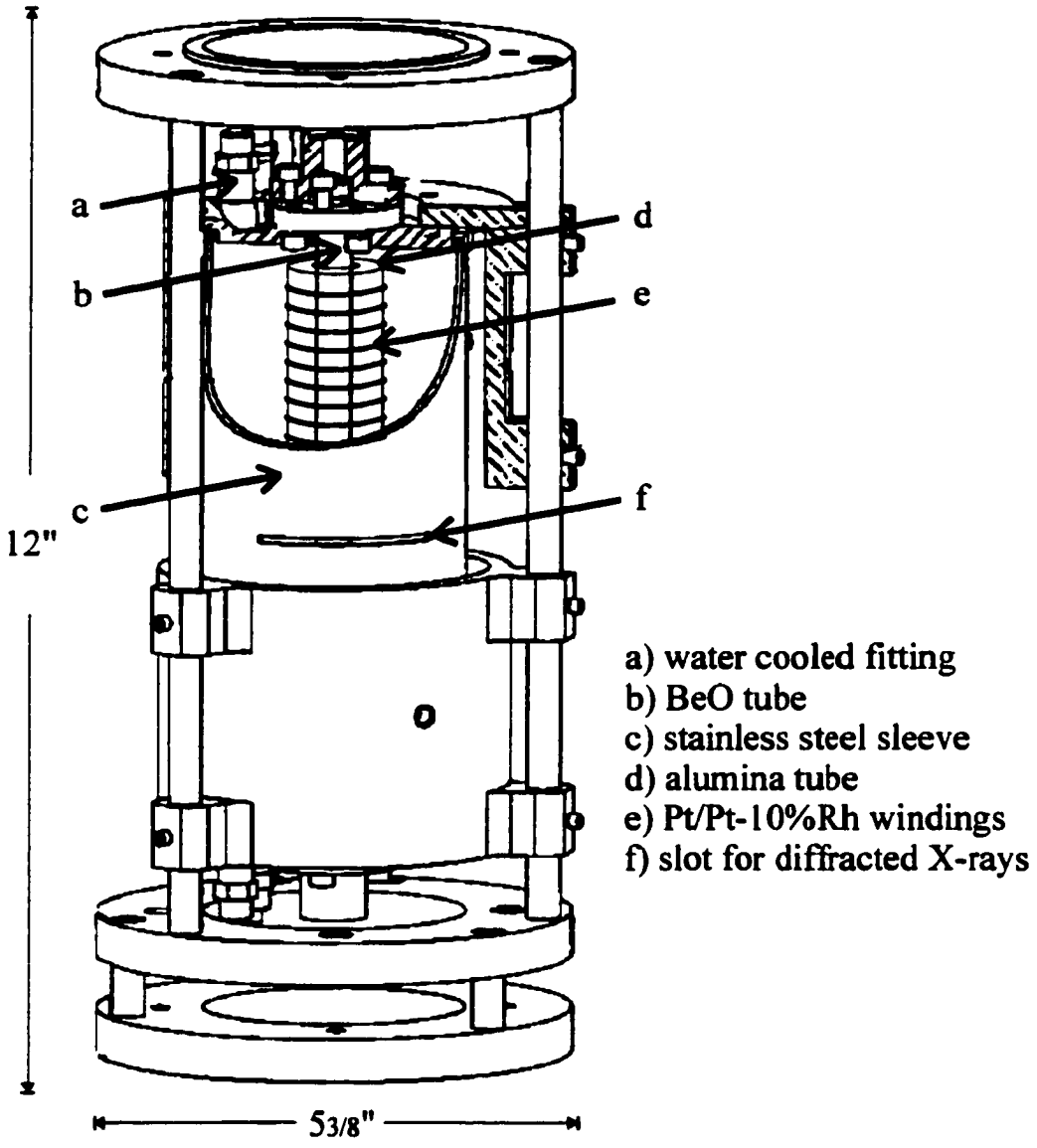


Figure 15. A schematic of the high temperature furnace design

to 90° 2θ, have been cut in the $Al_2O_3$ tube, SALI insulation, and stainless steel sleeve so that the BeO tube is the only attenuating material through which the x-rays pass. The furnace has been designed as a scaled down version of standard tube furnaces which are routinely used in many research laboratories in order to mimic actual processing environments as closely as possible.

The furnace is set inside an aluminum frame with a spring loaded end ring which has been designed to snap easily onto the chi-circle of a standard Huber four circle goniometer, where it is then secured using the standard mounting holes. The furnace is adjustable within this frame in the x, y, and z directions to allow proper alignment with the diffractometer and beam axes. Symmetrically placed spring loaded pins assure that the sample tube position remains centered during thermal expansion of the furnace assembly. Water cooled fittings with O-ring seals are attached to either end of the furnace to provide attachments to thermocouple leads, vacuum and gas lines, and the rotating sample holder. Depending upon the particular sample, furnace atmosphere, and temperature range of interest, a variety of sample tubes can be used including quartz, MgO, $Al_2O_3$, and BN. The low absorption of high energy x-rays offers greater flexibility in choosing sample holders while still maintaining good sample to holder signal ratios.

Sample rotation is achieved by magnetically coupling the sample holder shaft to a rotating motor shaft. This isolates the drive motor from the sample space and avoids any possible compromise of the atmosphere integrity. A rotating motor shaft seal can easily produce small leaks which would be unacceptable for oxygen sensitive materials, while placing a motor within the sealed sample space could produce potential outgassing problems. A schematic of the assembly is shown in figure 16. Two sets of four ¼" diameter $SmCo_5$ magnets are used for the coupling. The sample can be either rotated continuously or rocked about some angular range. A maximum rotation speed of 1000 revolutions per minute is possible.

**Atmosphere control**

A Sierra Instruments electronic flow controller was used for gas mixing and flow rate control. Using a divided gas flow, typical flow rates through the furnace ranged from .1 to 5 cubic centimeters per minute. The oxygen partial pressure of the environment can be easily

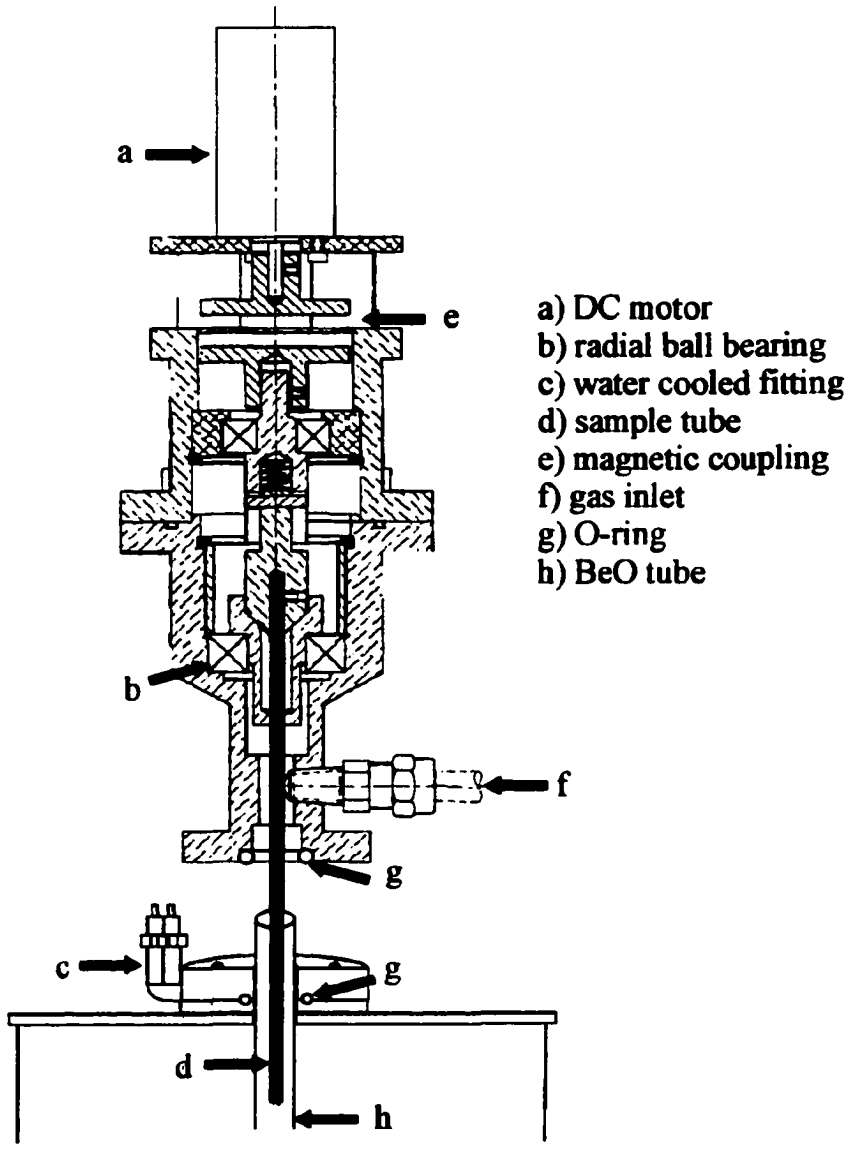


Figure 16. A schematic of the magnetically coupled sample rotation attachment

controlled for $PO_2$ sensitive samples such as high temperature oxide superconductors. For highly oxidizing materials, the furnace seals were checked with a Helium leak detector. Helium leakage was below the sensitivity of the detector ($10^{-6}$ mbar·litre/s). In this case, the oxygen content of the sample space is limited by the purity of the incoming gas. For extremely oxidizing materials, quartz tubes containing sample powder and gettering material can be vacuum sealed. Such samples holders were found to be very effective for preventing oxidation as well as for containing reactive liquids.

**Temperature calibration**

The temperature calibration curve and gradient profile of the furnace were measured using a NIST traceable R-type thermocouple which has been calibrated to +/- .1° C. This thermocouple was placed in the center of the sample position and its value recorded versus the control thermocouple value. This is shown in figure 17. Additional data points are given for the solid state transformation temperatures of $BaCO_3$ and $SrCO_3$ (NBS temperature standards, GM-760) as observed by in situ x-ray diffraction. figure 18 shows the thermal gradient profile along the furnace tube axis at a series of temperatures. The probed length of the sample is typically between 1 and 2 mm which corresponds to a $\Delta T$ of less than 1°C across the illuminated sample length.

**Sample preparation and alignment**

The sample and sample holder preparation and alignment are a critical component toward achieving artifact free high temperature x-ray diffraction. To assist in powder averaging and avoid data analysis complications due to extinction, powders should be ground to a particle size of 1-10 μm. Sample capillary tubes of MgO or quartz were used depending on the reactivity of the sample and temperature range of interest. Capillary tubes were fit with BN bushings in order to minimize precession during rotation. In general the vertical size of the incident beam was .75 - 1 mm. Centering the sample inside the furnace on this beam is a challenge, but must be done carefully to avoid aberrations that will be introduced into the diffracted pattern in the case of an incident beam scattering from the top or bottom surface of the sample tube. The sample tube undergoes some precession during rotation even with the added bushings. This may be used as an aid in centering the sample on the beam. By measuring the attenuation of the transmitted beam during sample rotation, this precession

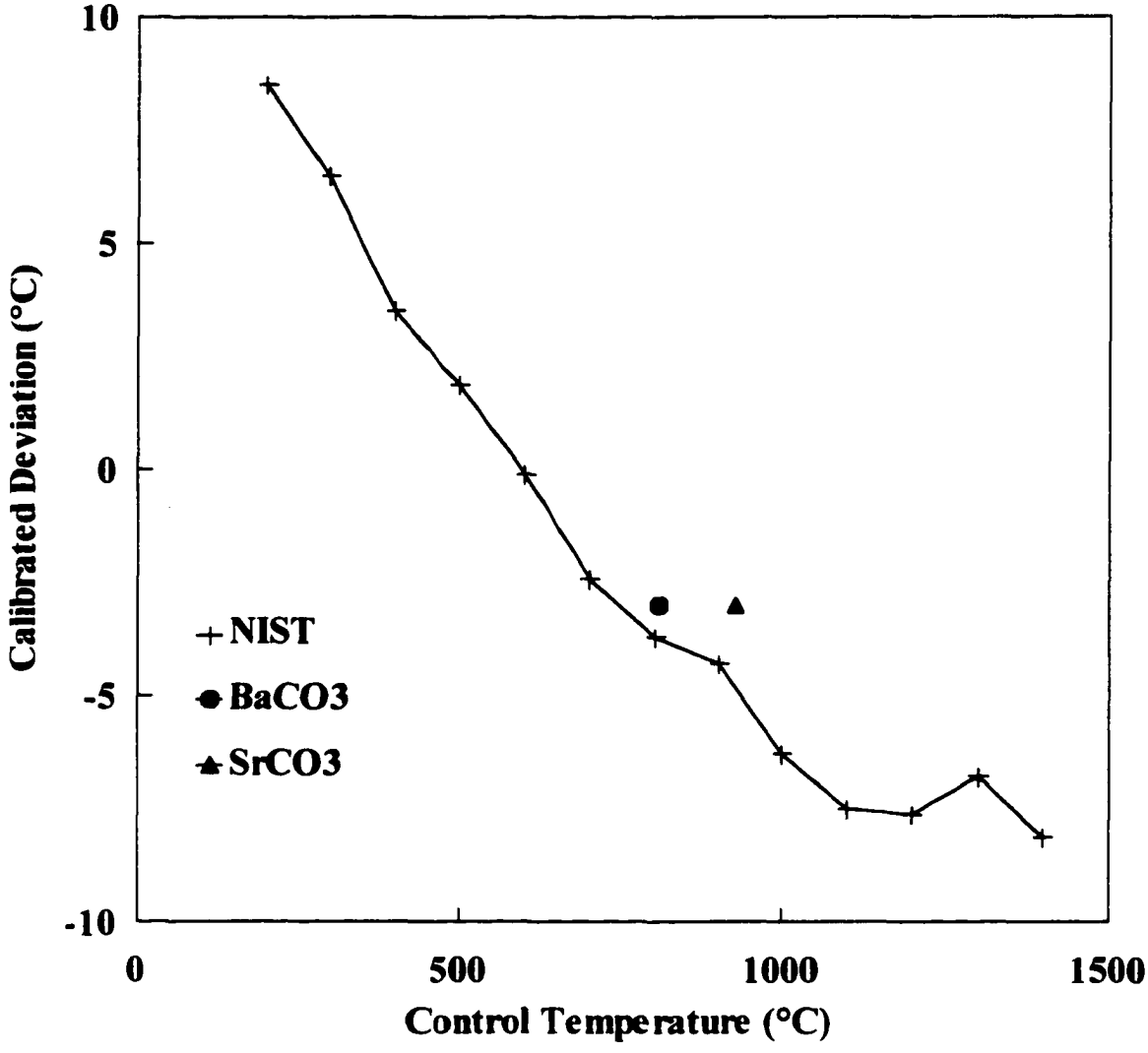


Figure 17. Temperature calibration curve as measured by a NIST traceable standard thermocouple and in situ observation of solid state phase transformations of $BaCO_3$ and $SrCO_3$.

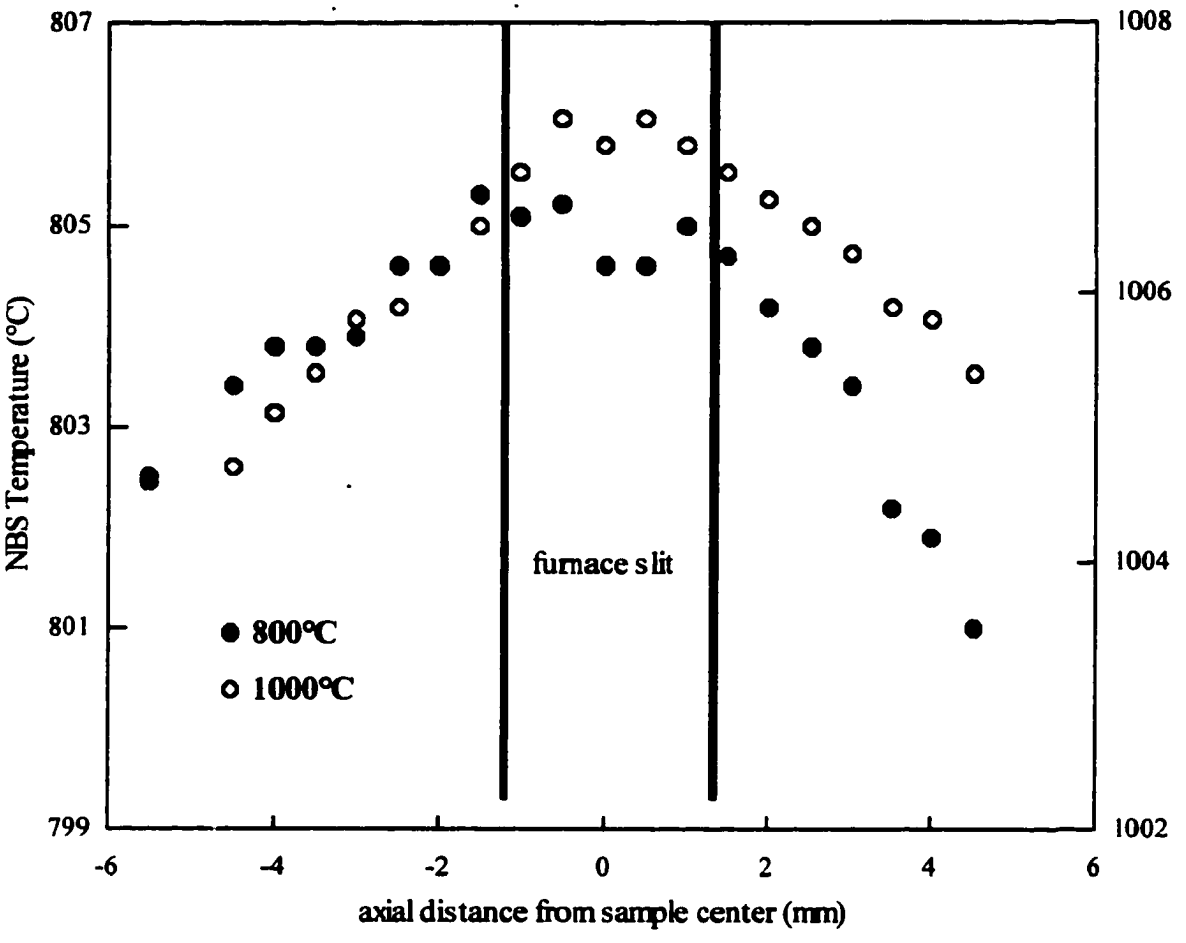


Figure 18. Axial thermal gradient profile at sample position.

can be observed, and the sample center identified. The diffractometer can also be scanned in height in order to bring the sample into the beam center. This method should only be used for time resolved measurements. Since the detector is not coupled to the two theta arm in the time resolved configuration, small offsets of the sample from the diffractometer center of rotation will not introduced errors into the measured diffraction peak positions. Figure 19 shows a scan of the transmitted intensity measured by an ionization chamber versus the diffractometer table height. Rocking the sample by 20°-30° about the minimum intensity position will maximize the fraction of sample bathed in the beam.

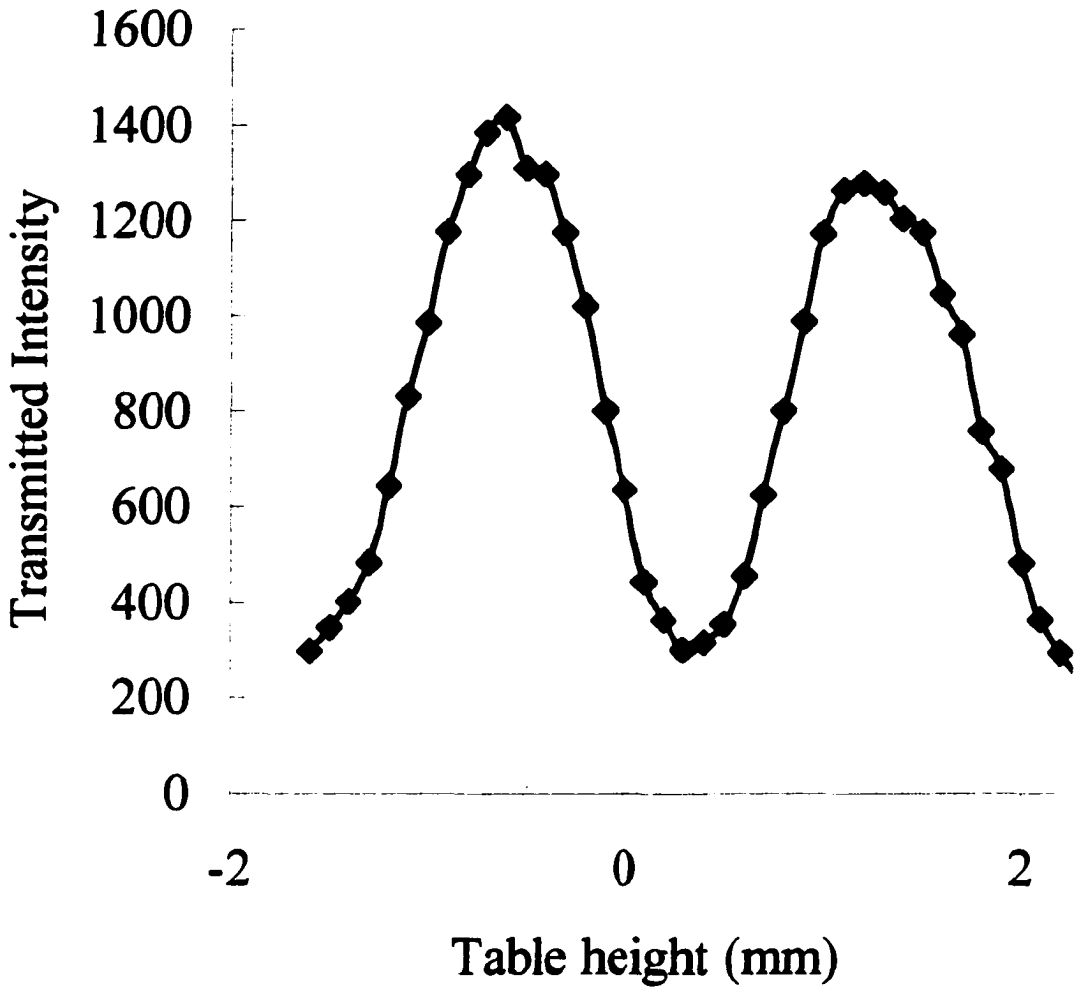


Figure 19. A diffractometer table scan can be used to locate the sample and center it on the incident beam.

## HIGH RESOLUTION DATA COLLECTION

### Diffraction geometry

Figure 20 shows a schematic of the optics used at the A2 line of CHESS for collecting data used in the structurai refinements presented below. A Si (111) double crystal monochromator was tuned to an energy of 60 keV using a calibrated solid state detector. The beam size was 2mm in the horizontal and 1 mm in the vertical giving an incident flux on the sample of approximately $10^{11}$ photons per second. A Si (111) analyzer crystal was used as an angular slit in front of a NaI detector. The analyzer and detector were scanned in the vertical scattering plane. The analyzer crystal was necessary to avoid resolution loss due to large sample diameters, and also minimizes sample displacement and fluorescence effects[119]. NBS standards were used to fit the wavelength and 2θ zero offset. Standards run at the beginning and end of the beam time showed the beam energy to be stable to within +/- 7 eV. It was found that the 2θ zero offset was very sensitive to small misalignments of the analyzer crystal. Therefore, the analyzer crystal orientation was periodically checked by centering the crystal rocking curve on the direct beam. Scans used for Rietveld refinement were typically done with step sizes of .002° 2θ and counting times of .5 to .85 seconds per data point. The typical angular range recorded was 3° to 15° 2θ, which corresponds to a range in reciprocal space of 1.6 to 8 $Å^{-1}$ for 60 keV X-rays. This led to data collection times of approximately 1 to 2 hours per scan. Scans taken with sample rocking were set up so that the two theta arm motion was coupled with the sample motor. The counting time for each step occurred over a 20° sample rotation at 4 rpm which alternated between clockwise and counterclockwise motion with each 2θ arm step.

### Peak profile shape and resolution

Previous work done at room temperature on high resolution powder diffraction has demonstrated that diffraction peak shapes can be well described using a psuedo-voigt function, which is a linear approximation to the convolution of Gaussian and Lorentzian functions[121]. The functional form gives the intensity as a function of displacement from the peak center (Δ2θ)

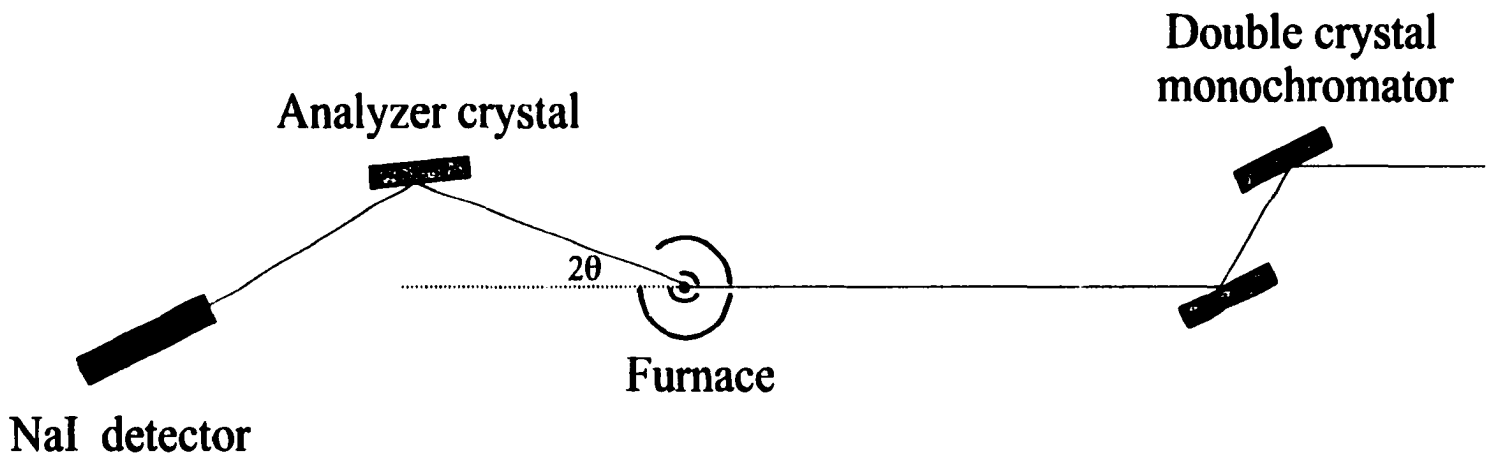


Figure 20. A schematic of the beamline optics and diffraction gemoetry.

$$I(\Delta 2\theta)=I_o\{2\eta/\Gamma\ [1+4(\Delta 2\theta/\Gamma)^2]^{-1}+2(\ln 2/\pi)^{1/2}(1-\eta)/\Gamma \exp[-4\ln 2(\Delta 2\theta/\Gamma)^2]\}+I_B, \quad (1)$$

where $I_0$ is the integrated intensity, $\Gamma$ is the full width at half maximum, $\eta$ is the mixing parameter for determining the Gaussian/Lorentzian contribution, and $I_B$ is the background intensity.

Individual peaks were fit to this function using the least squares peak fitting program PeakFit from Jandel[128]. Figure 21 shows a fit to the (111) reflection from an NBS $CeO_2$ standard. The fit is quite good, and the peak shape is highly symmetric even at this low angle (3.74°). The $CeO_2$ standard should not exhibit significant sample broadening effects and therefore should give a fairly good indication of the instrumental resolution of the experiment. It has been shown[129] that in a non-dispersive geometry the instrumental resolution function of a double crystal monochromator and analyzer crystal is given by:

$$\Gamma(\theta) = \{\phi_v^2(2\tan\theta/\tan\theta_M - \tan\theta_A/\tan\theta_M - 1)^2 + \Gamma^2_{min}\}^{1/2}, \quad (2)$$

where $\phi_v$ is the vertical divergence of the incident beam, $\theta_M$ and $\theta_A$ are the Bragg angles of the monochromator and analyzer respectively, and $\Gamma_{min}$ is the natural Darwin width of the crystals. Figure 22 shows the variation of reflection width with scattering angle for the $Al_2O_3$ standard. The solid line is a least squares fit of the data to equation (2).

**Rietveld refinement**

In Rietveld refinement, powder diffraction intensity data is fit using a least squares algorithm to a function of the form:

$$Y_i = B_i + s\,\Sigma|F(hkl)|^2\,\phi(\Delta 2\theta), \quad (3)$$

Where $B_i$ is the background intensity, s is a scale factor, the summation is over the complete set of contributing reflections at each data point, and $\phi$ ($\Delta 2\theta$) is the peak profile function[130]. A number of possible parameters can be fit which correspond to models of the sample structure and diffraction geometry. Among the parameters fit in this experiment were $2\theta$ zero offset, x-ray wavelength, cell parameters, isotropic or anisotropic thermal parameters, variable atomic positions, background function, peak profile parameters, and a preferred orientation parameter. In addition, anomalous dispersion corrections were entered based on tabulated values. All refinements were performed using GSAS[131]. Diffraction peaks from the BeO furnace tube and MgO sample holder were excluded from the refinements. Due to the high resolution of this experiment, overlap with sample peaks was

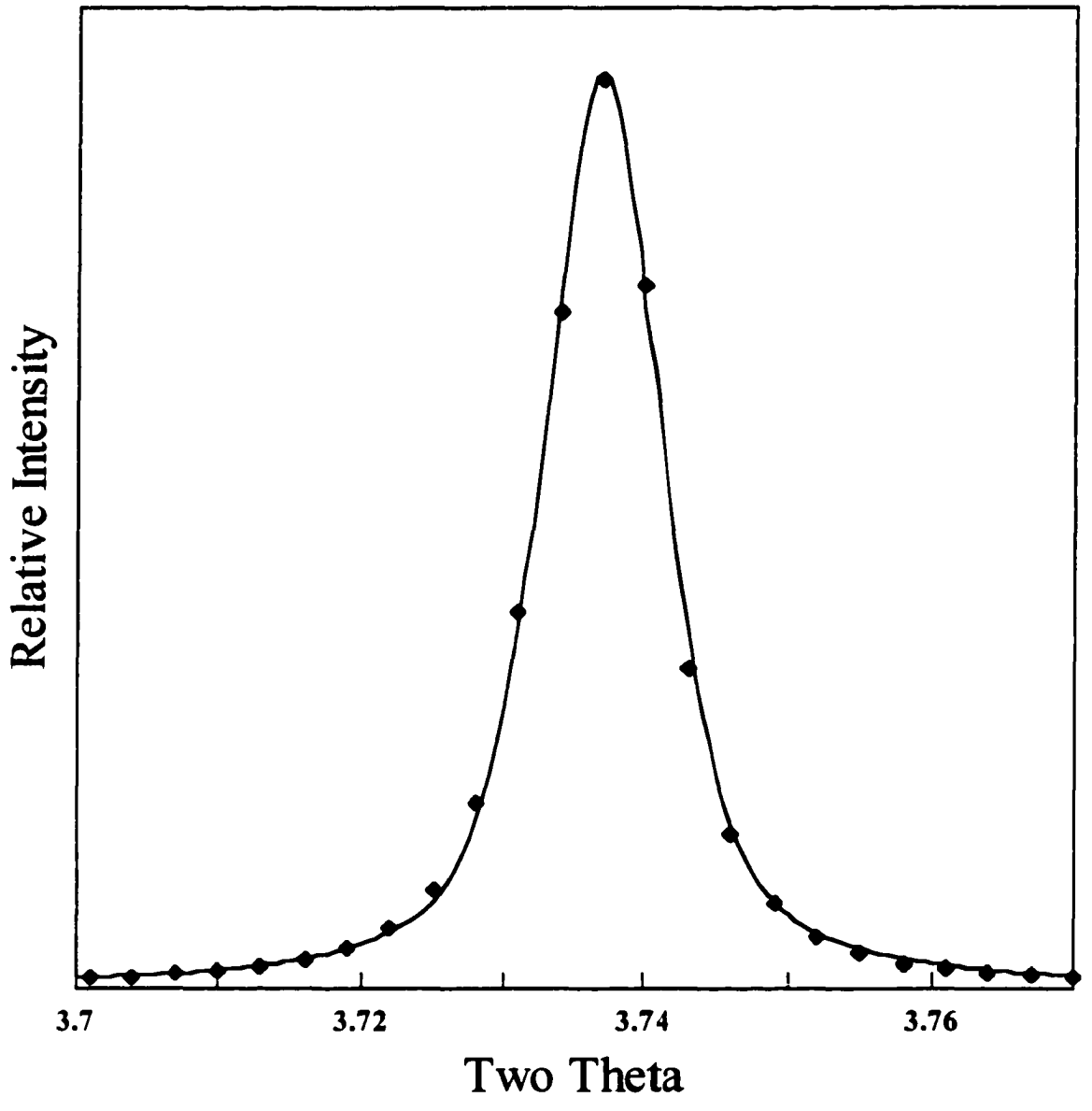


Figure 21. The (111) reflection from a $CeO_2$ standard powder fit to a pseudo-voigt function.

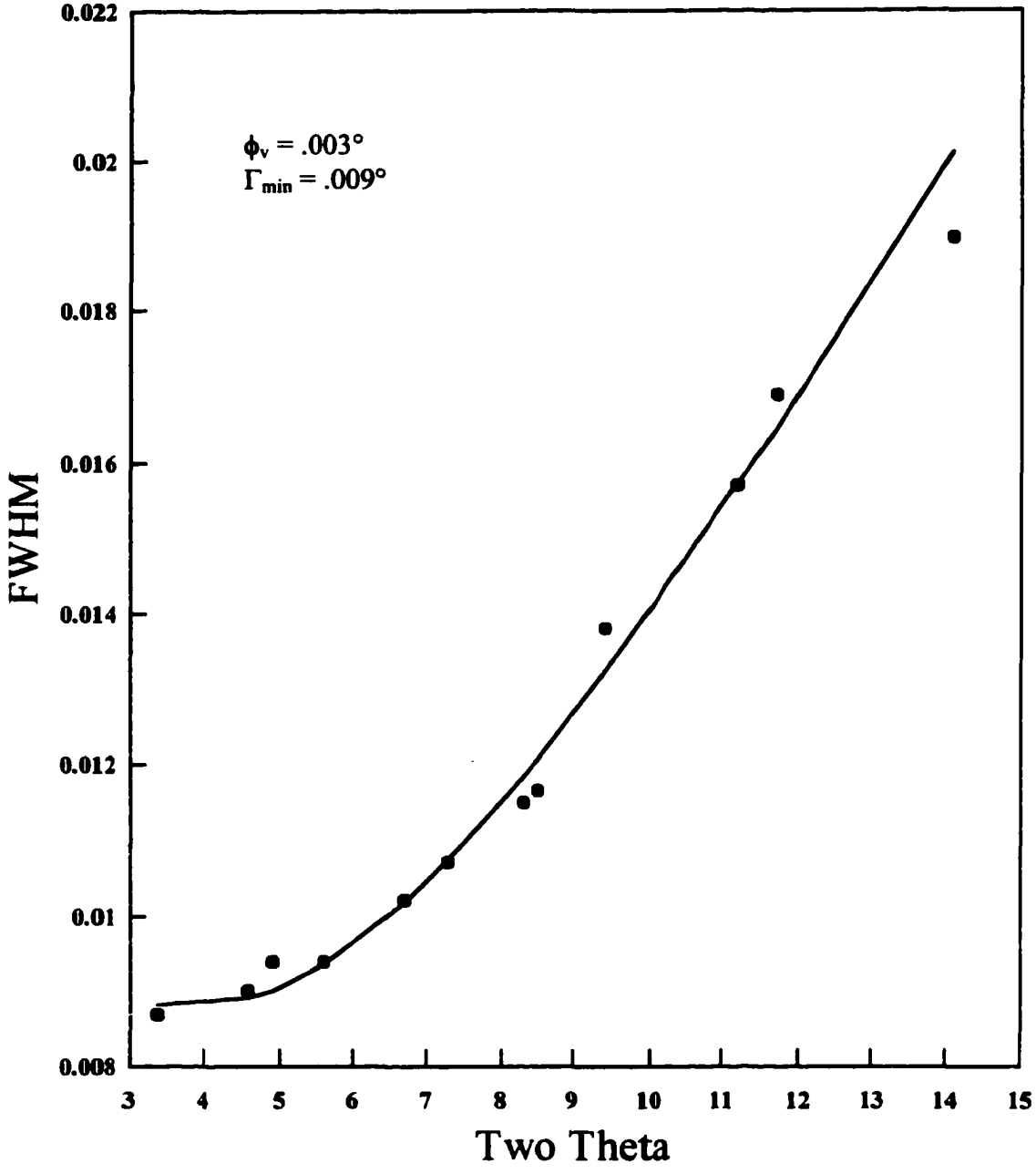


Figure 22. $Al_2O_3$ reflection widths fit to the instrumental resolution function. $\phi_v$ is the vertical divergence of the white beam and $\Gamma_{min}$ is the combined darwin width of the monochromator and analyzer crystal.

minimal, and the BeO and MgO peaks could be removed with minimal loss of sample reflection data.

$CeO_2$ (NBS standard 674a) was used as a wavelength and zero offset calibration standard by performing refinements with the cell parameter fixed at the NBS certified value. It was found that sample rotation was critical for successful Rietveld fitting. Refinement of the data set collected with a stationary sample was highly unstable and failed to converge. Data collected while rotating the sample about 20° per data point successfully converged with a weighted residual of 10.56%. Figure 23 shows the refinement plot with residuals of this $CeO_2$ data set. The effect of sample rotation can be directly appreciated by comparing CCD images of diffraction rings from stationary and rotating samples (Figure 24). The stationary sample gives a highly non-uniform intensity along the diffraction ring, which is typical of incomplete powder averaging. When the sample is rotated, though, the ring becomes uniform and the diffracted intensities can be used to reliably model structural parameters. It is clear that the lack of complete powder averaging in the case of the stationary sample introduced random errors into the structure factor measurements which prevented stable refinement.

Powder pattern refinements performed on data collected with tube sources will often converge to a residual of 2% or less. For powder patterns collected with synchrotron radiation, though, a residual of 10 to 20% is typical [129]. This increased residual is due primarily to the higher instrumental resolution associated with synchrotron radiation. As the instrumental resolution increases, sample broadening effects become more pronounced and tend to dominate peak profile shapes. This reveals the inadequacies in current peak profile modeling which are otherwise masked by the more easily modeled instrumental profile parameters of low resolution experiments. More advanced peak shape modeling which can take into account anisotropic line broadening effects is needed to allow better refinement of synchrotron data. In many cases, it may be advantageous to reduce the instrumental resolution of the experiment to just exceed the intrinsic sample resolution. This will not only simplify peak profile fitting, but will also increase diffracted intensity and speed data collection. This can be easily achieved by switching from a Si analyzer crystal to a wider bandpass crystal such as Ge. In addition, the double crystal monochromator should be

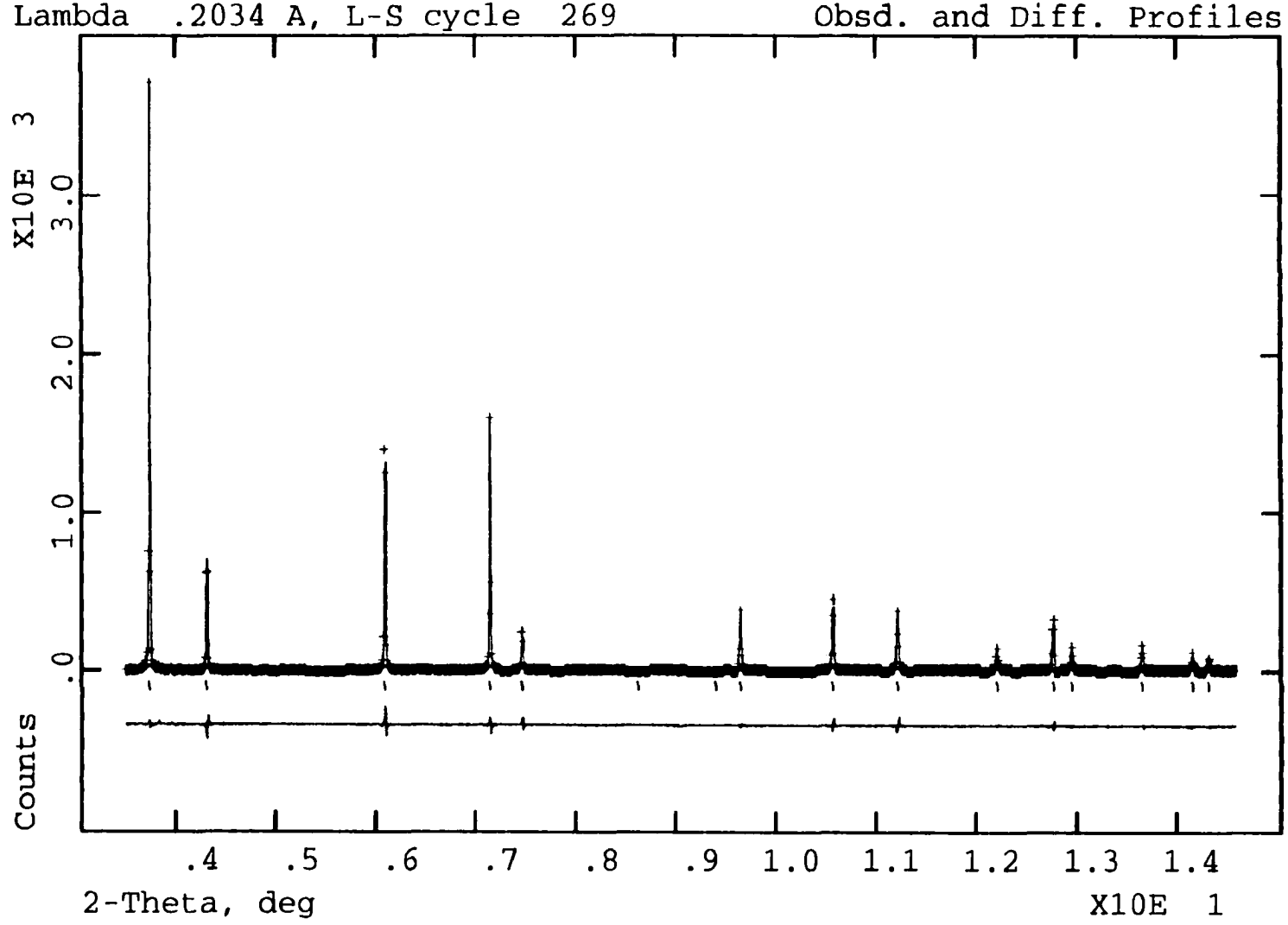


**Figure 23. Rietveld refinement of $CeO_2$ standard powder**

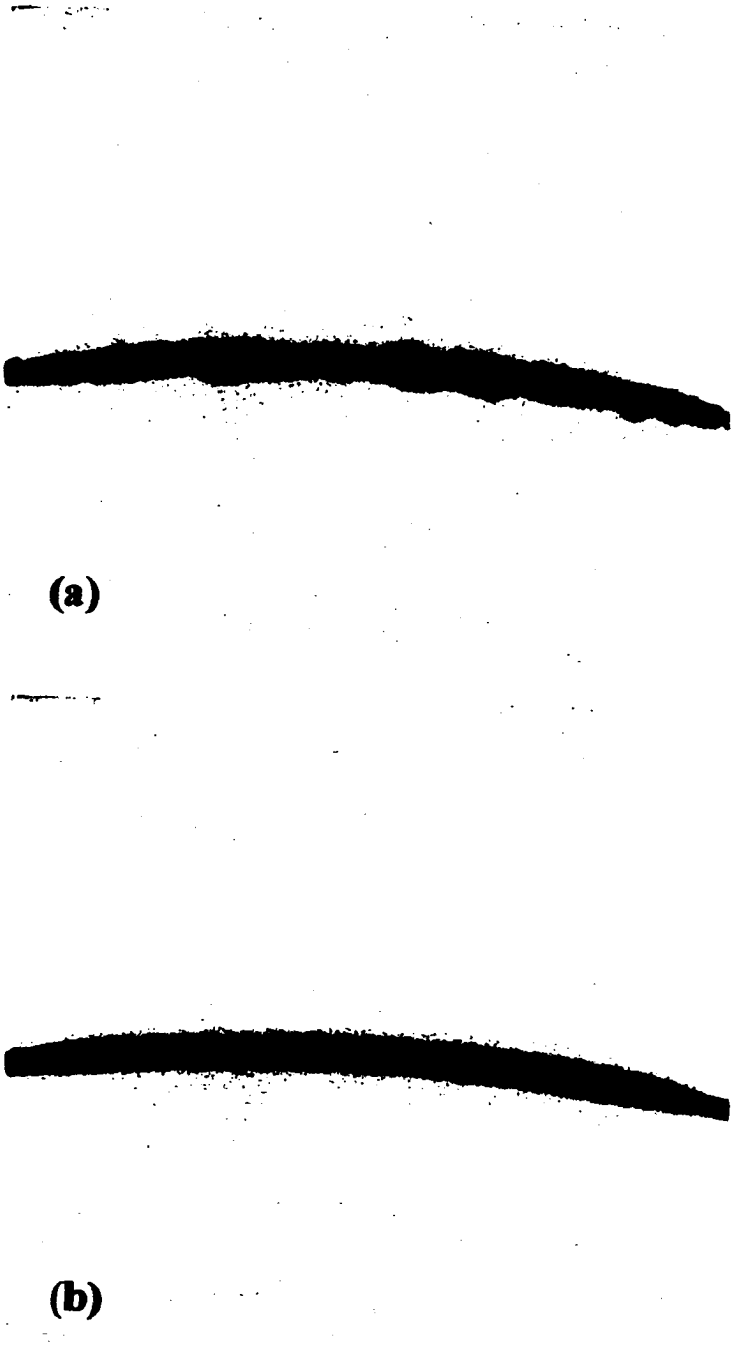


Figure 24. CCD images of $Fe_3Al$ powder (a) taken with a stationary sample and (b) taken with sample rotation.

changed to match the analyzer width for an additional increase in incident flux without any additional loss in resolution. Unfortunately, at the present time the availability of a flexible range of optical components for high energy use is limited. This should change as the new generation of insertion devices produce an increased use of high energy x-ray photons.

Of course, there are cases when maximum resolution is desirable. With the resolution achievable using synchrotron radiation, the level of sensitivity to broadening effects due to sample inhomogeneities, strain, or particle size may be raised by an order of magnitude

**$Al_2O_3$ case study**

In order to test the ability to refine variable atomic positions, especially at high temperatures, $Al_2O_3$ powder (NBS standard 674a) was examined at room temperature, 873 K, and 1473 K. Data was collected for a $2\theta$ range of 2.5° to 14.5° with a step size of .002° and counting time of .5 seconds. The sample was contained in a 1mm ID MgO tube. Figure 25 shows a Rietveld refinement plot of the 1473 K scan. Table 10 gives the refined parameters for these data sets.

The most striking disagreement between the refined parameters and those reported previously in the literature is in the thermal parameter values. Thermal parameters are notoriously difficult to measure accurately using x-ray powder diffraction data, since many of the systematic geometric and sample aberrations that can be introduced into powder diffraction data can be approximated by exponential functions which may be absorbed into the thermal parameter correction terms. For the case of a cylindrical sample which is completely bathed in the incident beam, the absorption correction can easily be taken into account[132]. For this experiment the vertical beam size was smaller than the sample diameter. In addition, slight precession during sample rocking further complicates the situation. For these reasons we were unable to adequately correct for absorption effects. This may explain the lack of agreement between various experiments and the non-physical negative values refined for some of the oxygen thermal parameters. The fact that the thermal parameters do increase with temperature suggests that at least qualitative trends in these values may be real. Smaller sample tube diameters are necessary to correct for this and to allow for quantitative thermal parameter determination.

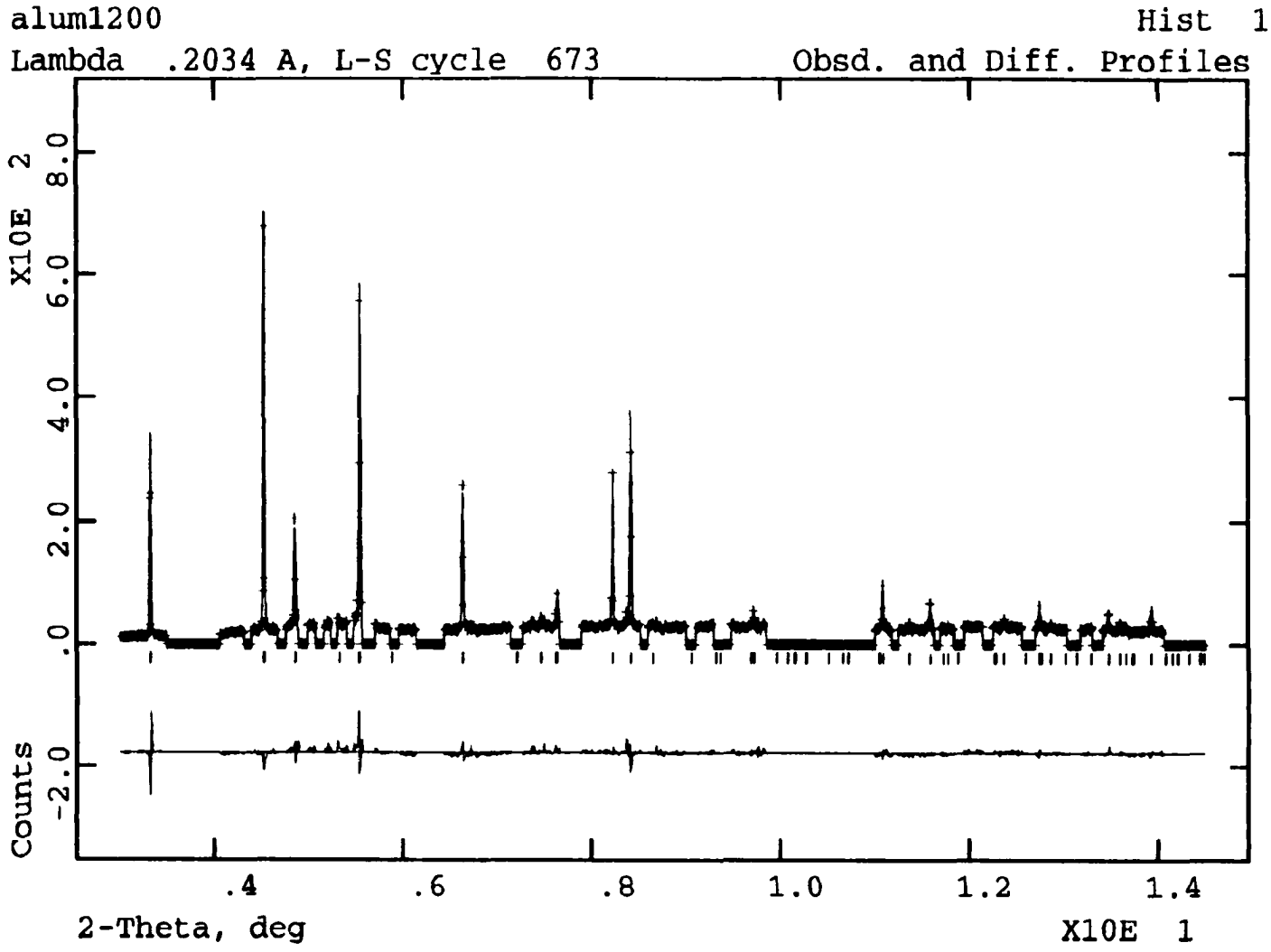


Figure 25. Rietveld refinement of $Al_2O_3$ at 1200°C. Regions containing peaks from the BeO furnace tube and the MgO sample holder were excluded from the refinement.

Table 10. Refined parameters for $Al_2O_3$ data sets. Single crystal data was taken with Mo $K_\alpha$ radiation [133]. The data from Cox, et al.[121] was taken with synchrotron radiation on a 0.5 mm capillary.

| | single xtal 293 K | Cox, et al. 293 K | this study 293 K | this study 873 K | this study 1473 K |
|---|---|---|---|---|---|
| a (Å) | 4.75999(3) | 4.7586(1) | 4.75957(4) | 4.77953(4) | 4.80754(4) |
| c (Å) | 12.99481(7) | 12.9897(1) | 12.9926(3) | 13.0551(3) | 13.1383(3) |
| Al(z) | .35219(1) | .3518(1) | .3528(1) | .3531(1) | .3533(1) |
| B(Al) ($Å^2$) | .26(1) | .68(5) | .54 | .86 | 1.42 |
| O(x) | .30633(5) | .3082(6) | .3066(5) | .3070(5) | .3071(5) |
| B(O) ($Å^2$) | .28(1) | .71(7) | -.26 | .16 | .42 |
| $R_{wp}$ | | .222 | .1300 | .1227 | .1209 |

The refined atomic positions show much better agreement with single crystal data[133], and there are clear trends when examining the high temperature structure. In the R3c structure of $Al_2O_3$ there are two variable atomic positions. Oxygen atoms are located at the position (x,0,1/4) and are six-fold coordinated forming a distorted hexagonal close packed structure. Al atoms are located at the position (0,0,z) and occupy 2/3 of the octahedral interstitial sites. The refined O(x) and Al(z) parameters reveal subtle structural distortions with temperature. To our knowledge, there has been only one other measurement of the high temperature variable atomic positions in $Al_2O_3$. That study was performed on a gas-flame heated single crystal at 2170 K[134], and the results are consistent with the structural trends observed in our refinements. These structural changes can be understood in terms of distortions in the bond distances within and between Al-O six fold coordinated polyhedra. Figure 26 shows a schematic of the coordinated polyhedral structure. Two $AlO_6$ octahedra share a common face which is perpendicular to the c axis. The Al(1)-Al(2) bond across this face is the nearest Al-Al distance in the structure. The Al atoms are displaced from the center of each $AlO_6$ octahedron away from the shared face and toward an empty interstitial site. This displacement becomes more pronounced with increasing temperature. This is clearly seen by examining changes in the two independent Al-O bond lengths within each octahedron. In Figure 27 the fractional change in the Al(1)-O(2)/Al(1)-O(9) bond mismatch is shown normalized to the room temperature values. The two Al-O distances are clearly diverging with increasing temperature. In addition, changes in the O atom site position tend to reduce distortions in the close packed structure. The refined interatomic distances and bond angles are further summarized in Table 11.

Recently, the equation of state of $Al_2O_3$ has been theoretically modeled using quasi-harmonic atomistic simulations[135]. A least squares approximation for the simulated temperature dependence of the atomic coordinates predicted a linear relationship. This is borne out in the experimental measurements presented here. It is interesting to note that the single crystal data from Ishizawa et al. [134] shown in figure 27 shows a deviation from this linear behavior. This is not unexpected from a theoretical perspective as the two body interatomic potential used in the quasi-harmonic model begins to breakdown at temperatures

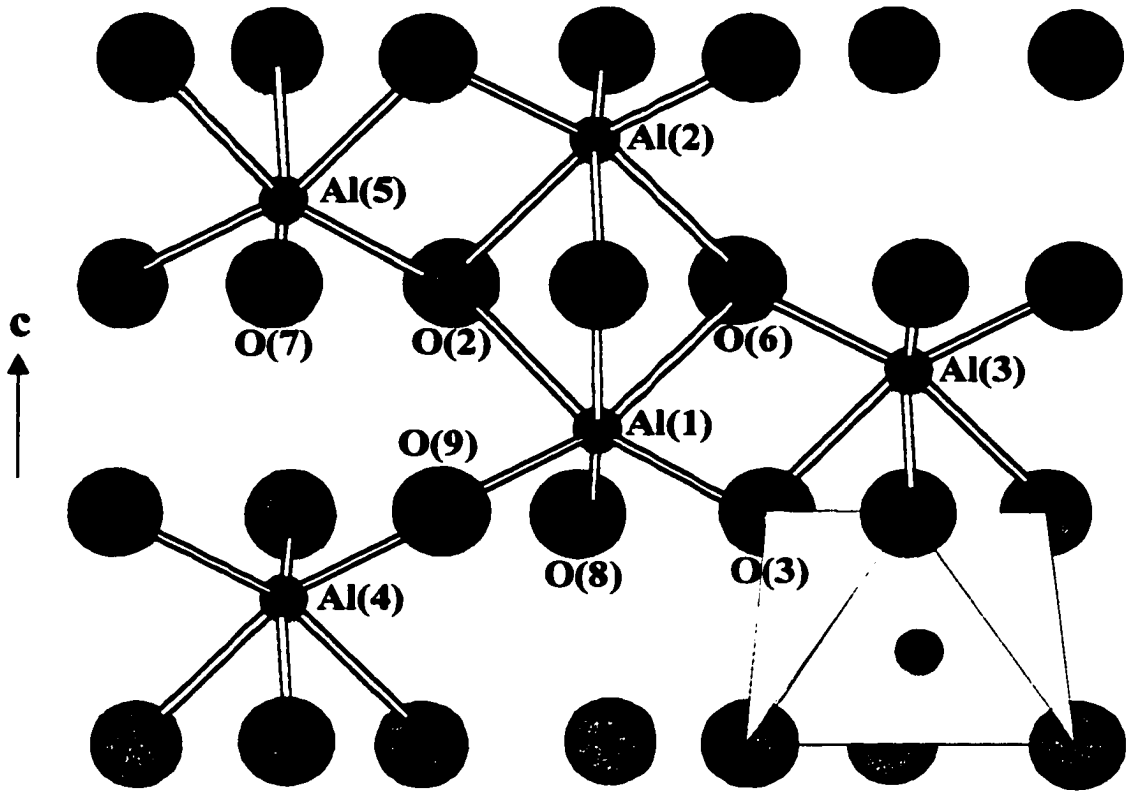


Figure 26. Structure of $Al_2O_3$ viewed looking down the [110] direction.

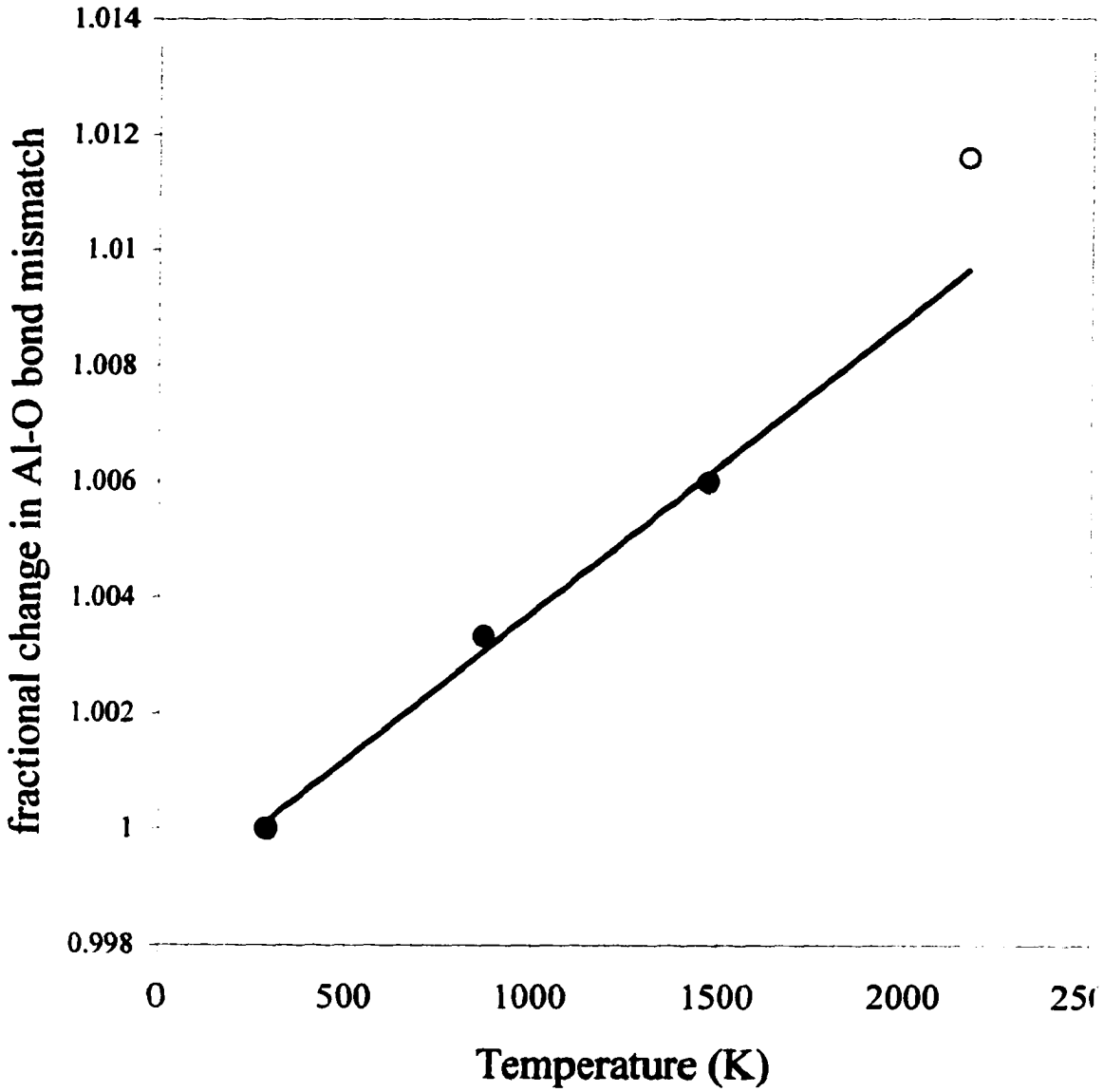


Figure 27. The fractional change in Al(1)-O(2)/Al(1)-O(9) bond length mismat normalized to room temperature. The value at 2170 K is taken from Ishizawa et al. [134].

approaching the melting temperature. The single crystal data was collected at 2170 K which is .95$T_m$, and one would expect deviations from linear behavior in this temperature regime.

Table 11. Interatomic distances (Å) and bond angles (°).

| | 293 K | 873 K | 1473 K |
|---|---|---|---|
| Al(1)-Al(2) | 2.672 | 2.692 | 2.715 |
| Al(1)-Al(3) | 2.794 | 2.807 | 2.825 |
| Al(1)-Al(4) | 3.210 | 3.220 | 3.236 |
| Al(1)-Al(5) | 3.499 | 3.514 | 3.535 |
| Al(1)-O(2) | 1.978 | 1.991 | 2.006 |
| Al(1)-O(9) | 1.850 | 1.856 | 1.865 |
| O(2)-O(6) | 2.528 | 2.542 | 2.557 |
| O(2)-O(7) | 2.864 | 2.875 | 2.891 |
| O(2)-O(8) | 2.621 | 2.633 | 2.650 |
| O(2)-O(9) | 2.725 | 2.737 | 2.753 |
| | | | |
| Al(1)-O(2)-Al(2) | 84.93 | 85.05 | 85.20 |
| Al(1)-O(6)-Al(3) | 93.68 | 93.67 | 93.67 |
| Al(1)-O(9)-Al(4) | 120.34 | 120.39 | 120.36 |
| Al(1)-O(2)-Al(5) | 132.04 | 131.96 | 131.91 |
| O(2)-Al(1)-O(6) | 79.41 | 79.32 | 79.21 |
| O(2)-Al(1)-O(9) | 86.32 | 86.33 | 86.33 |
| O(9)-Al(1)-O(3) | 101.44 | 101.53 | 101.62 |
| O(2)-Al(1)-O(3) | 163.87 | 163.75 | 163.61 |

## TIME RESOLVED DATA COLLECTION

### Diffraction geometry

In order to achieve time resolved data collection, modifications must be made to both the furnace design and detector system. The analyzer crystal must be abandoned in favor of a position sensitive detector. This results in a significant loss of resolution. The instrumental resolution function for this geometry can be expressed as

$$\Gamma = [\phi_v^2(2\tan\theta/\tan\theta_m - 1)^2 + \delta^2]^{1/2} \quad (4)$$

where $\phi_v$ is the vertical divergence of the incident beam, $\theta_m$ is the bragg angle of the monochromator, and $\delta$ is the convolution of the incident beam and the sample diameter.

$$\delta = (D_s^2 + D_d^2)^{1/2}/D_{sd} \quad (5)$$

where $D_s$ is the sample diameter, $D_d$ is the spatial resolution of the detector, and $D_{sd}$ is the sample to detector distance[129].

The use of high energy x-rays limits the available detector choices. The efficiency of gas detectors is related to the ionization cross section of the gas at the energy of interest. At energies above 45 keV conventional detector gases such as Ar or Ne are not appropriate. At these energies Xe or Rn must be used, and safety as well as cost issues have discouraged this approach. Image plates are an attractive alternative due to their ease of use and efficiency at high energies. For this experiment a 20cm X 25cm Fuji image plate was used as a detector. These image plates have a 100μm pixel size. Figure 28 shows the instrumental resolution data for a .7mm ID capillary tube filled with Si standard powder. Data was collected with a sample to plate($D_{sd}$) distance of 1.36m at 60 keV. At this distance, the angular collected range of the image plate is 12° with a pixel size of approximately .004° 2θ. In order to fit equation (4) to the Si reflection data, a sample diameter($D_s$) of .35 mm had to be used. This implies one of two things. Either the sample was not properly centered causing the beam to clip the top or bottom of the sample tube, or the beam size is approximately .35mm in the vertical. The fact that the Si peak widths seemed to be independent of sample size suggests the latter. From the size of the source a maximum beam size of approximately 1 mm should be possible. Slight deviations in the beam position, though, due to heat load on the

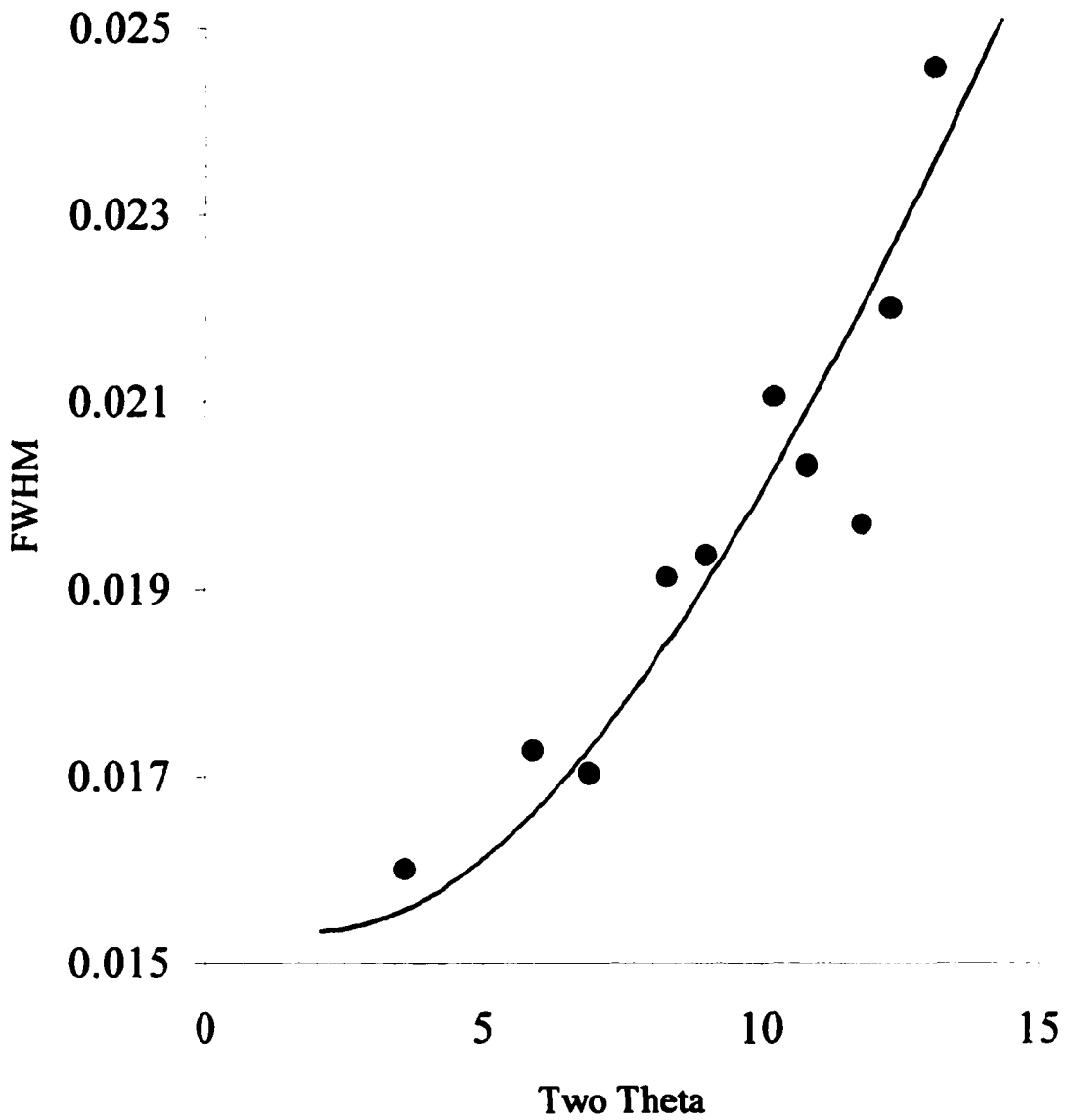


Figure 28. Si standard reflection widths fit to the instrumental resolution function with $D_s$=.35mm, $D_d$=.1mm, $D_{sd}$=1.36m, and $\phi_v$=.003°.

monochromator optics or instabilities in the ring could easily shrink the effective size of the beam at the sample. Slits immediately upstream from the furnace are used to define the beam position on the rotational center of the diffractometer, so any movement in the beam position will cause an effective decrease in the size of the beam.

Without an analyzer crystal, we are now considerably more sensitive to misalignments in sample position. In order to correct for the added geometrical aberrations introduced as a result of the use of a position sensitive detector, it is useful to be able to record reflections at negative bragg angles. A furnace core was constructed for this use, modified to pass scattered x-rays from -45° to 45° 2θ. With this geometry there are three parameters which must be fit using a standard powder pattern. The wavelength and 2θ zero must be fit as in the high resolution set-up, but the additional sample to detector distance must also be fit. In order to correct for misalignments in the image plate position, it is useful to be able to collect standard Si patterns periodically along the image plate width. Since it is not practical to take these room temperature Si patterns from a sample inside the furnace, a Si foil was positioned downstream of the furnace. This foil could be moved in and out of the direct beam to record calibration patterns when necessary. Since the use of an analyzer crystal minimizes the effects of most geometrical misalignments, and analyzer point detector step scan was performed on Si standard powder to independently fit the wavelength. This value could then be used to fit the sample to detector distance for both the sample capillary and the downstream Si foil. Figure 29 shows a schematic of the detector geometry. The image plate is scanned behind a 1mm wide vertical slit. Diffraction data has been collected in two modes. In the first mode, the image plate is continuously scanned across the slit. The time resolution of the experiment is then controlled by the width of the slit and the scanning speed. Measurements can be taken at a constant heating rate so that a linear temperature scale can be easily correlated with the image plate scan. This continuous scan mode can introduce complications into the collected pattern. By scanning the plate during data collection, a convolution between the image plate slit and the diffracted Debye rings will cause peak broadening and asymmetry. To avoid this effect, a second measurement mode was used. A shutter was placed in the direct beam upstream from the furnace. The shutter motor was coupled with the image plate translation motor so that the beam was shuttered

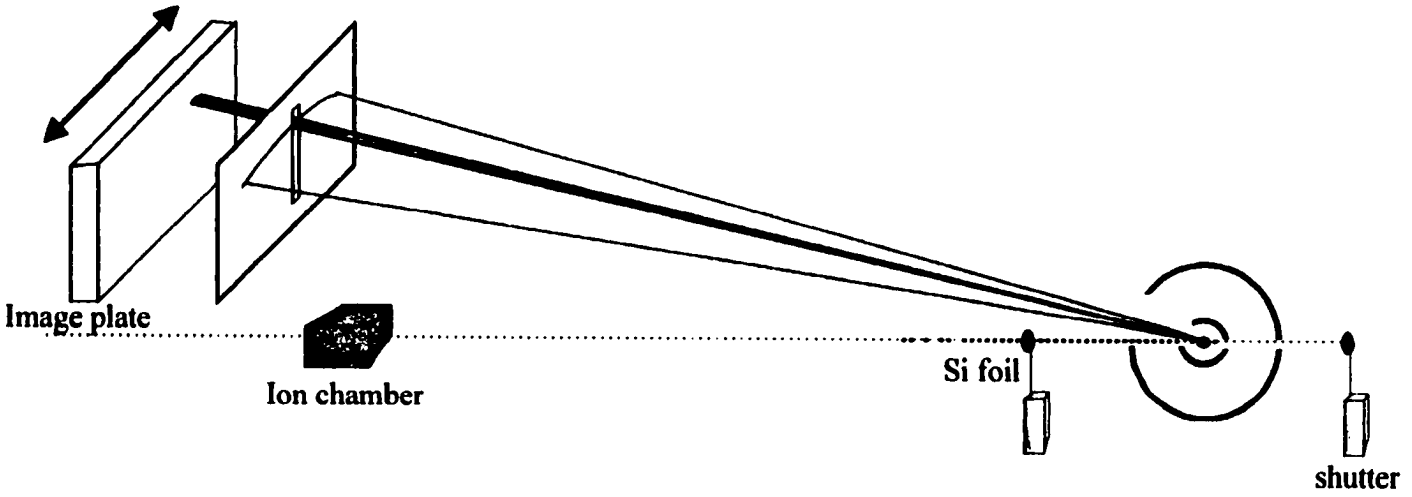


Figure 29. A schematic of the beamline optics used for time resolved measurements.

during image plate motion. In this mode, a series of discrete exposures are taken along the image plate. With the lower resolution of this detector system, overlap between the sample peaks and peaks from the BeO furnace tube becomes a concern. If the temperature range of interest is below 1200°C, an amorphous silica tube can be used to prevent this overlap.

**Data analysis**

Data was collected on $Al_2O_3$ standard powder in order to test the potential for structural refinement with this technique. A cut of the image plate which corresponded to a time exposure of 7.5 seconds was processed to correct for aberrations due to the flat plate detector geometry. The processed data was then used for Rietveld refinement. Scattering from the amorphous silica furnace tube complicates the fitting, and a 26 term radial distribution function was necessary to properly model the background. The weighted residual of the final refinement was 6.87% (figure 30). This lower residual as compared to the high resolution step scan refinements does not necessarily reflect a better structural fit, but rather is indicative of the higher background contribution to the image plate pattern. Despite the larger background and lower resolution, structural parameters could still be successfully fit. The Al(z) and O(x) variable atomic positions refined to values of .3521 and .3064, respectively. These values are in close agreement with the single crystal data presented in Table 10. The ability to collect high temperature Rietveld refineable diffraction patterns with a time resolution on the order of seconds opens up the possibility of observing subtle structural changes during phase transformations. In particular transient metastable structures may be observable in the intermediate stages of kinetic processes.

**$SrCO_3$ case study**

$SrCO_3$ undergoes a first order phase transformation from the orthorhombic space group Pmcn to the rhombohedral space group R3m at 928°C. This transformation is often used as a thermal analysis calibration standard due to the fast transformation kinetics. This makes it an ideal model system to observe nucleation and growth kinetics of first order transformations in real time. Figure 31 shows a full image plate pattern collected during heating and cooling through this transformation at 10°C/min. The boxed area is presented in figure 32 as a three dimensional surface plot. This allows a better appreciation of the

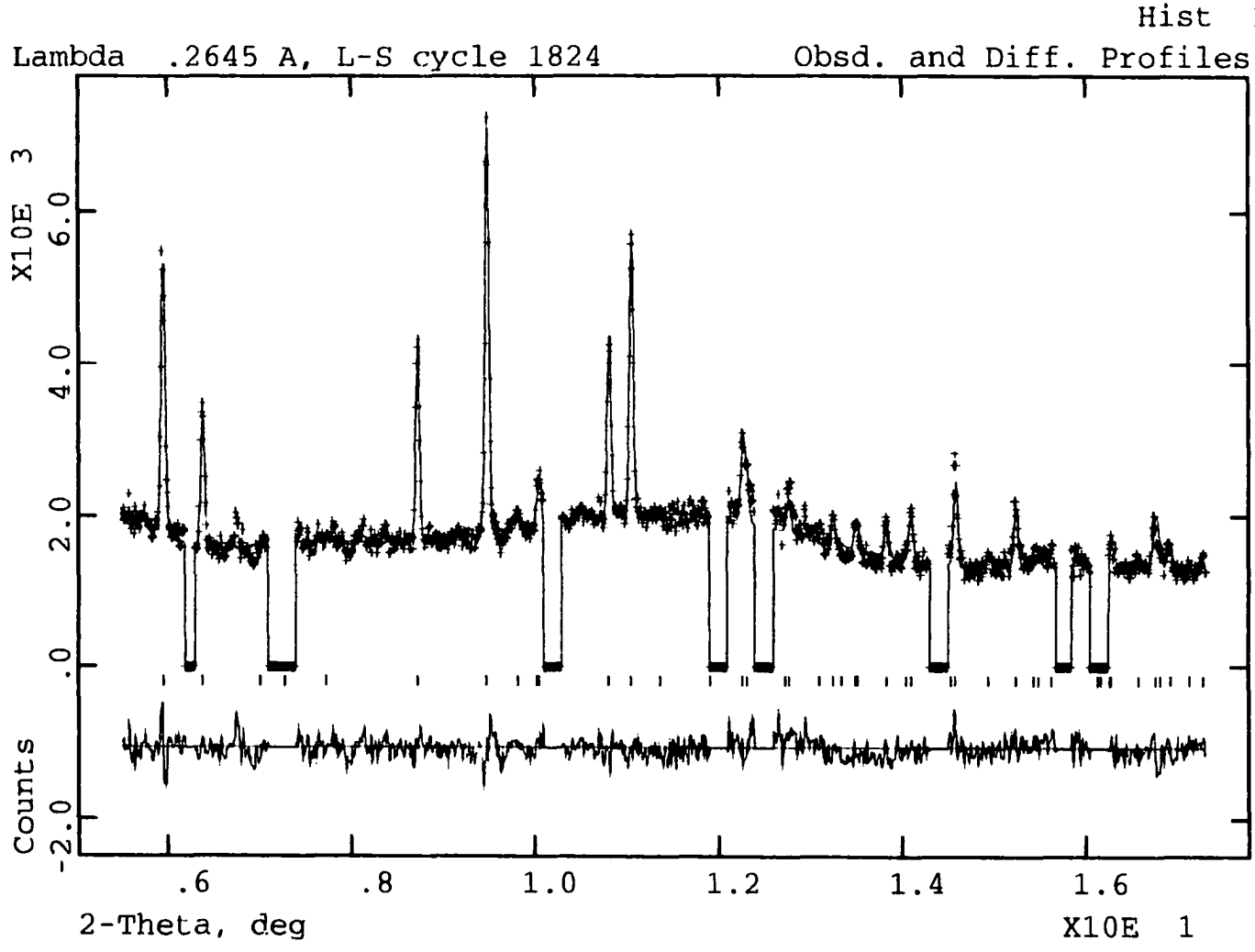


Figure 30. Rietveld refinement plot of an $Al_2O_3$ powder pattern taken with a 7.5 second image plate exposure. Regions containing reflections from the MgO sample holder were excluded from the refinement.

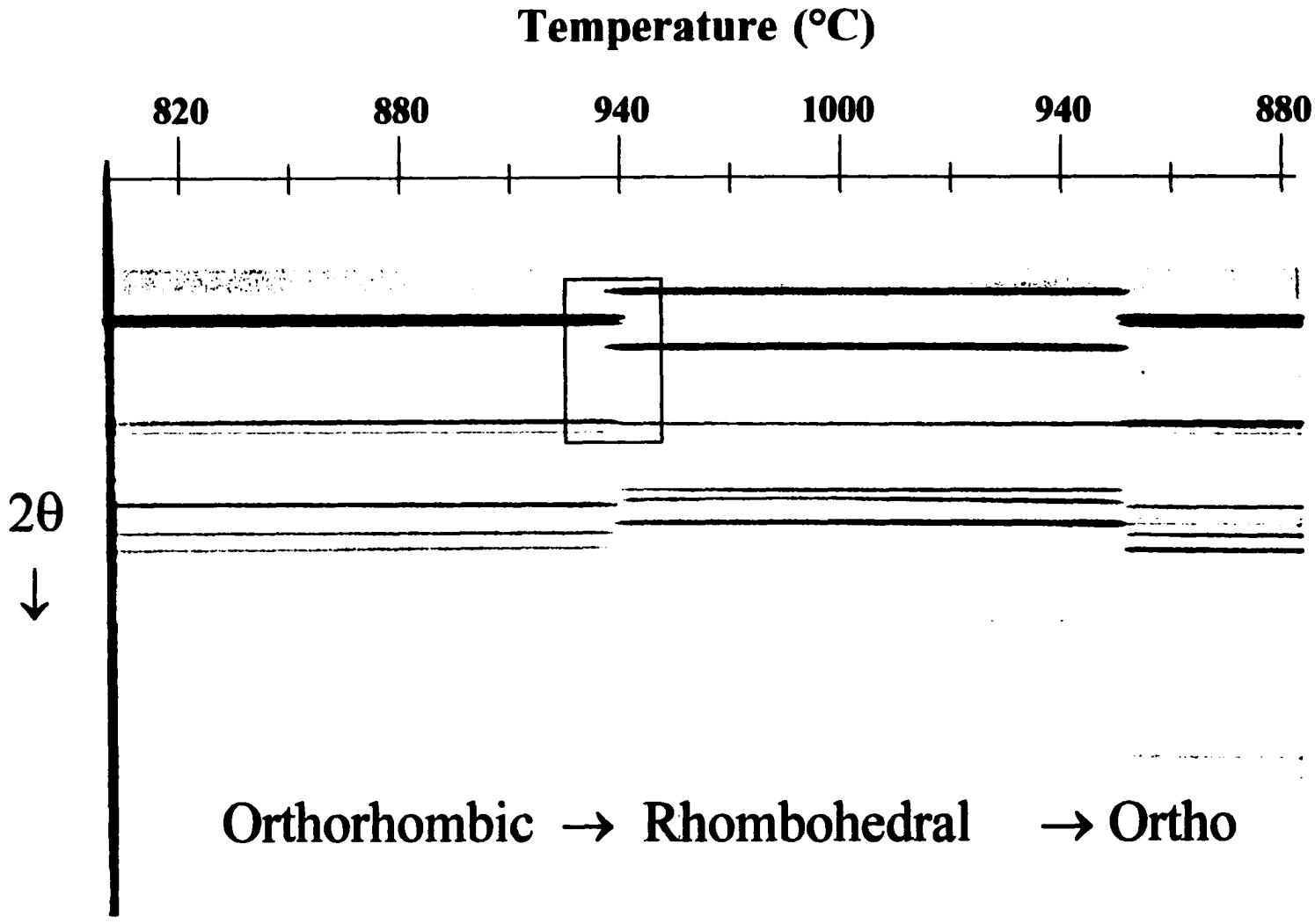


Figure 31. Image plate scan of the reversible orthorhombic to rhombohedral phase transformation on heating and cooling of $SrCO_3$. The ramp rate was 10°C/min for both heating and cooling. The full height of the image plate corresponds to a 2θ range of 1.5° to 17.5°.

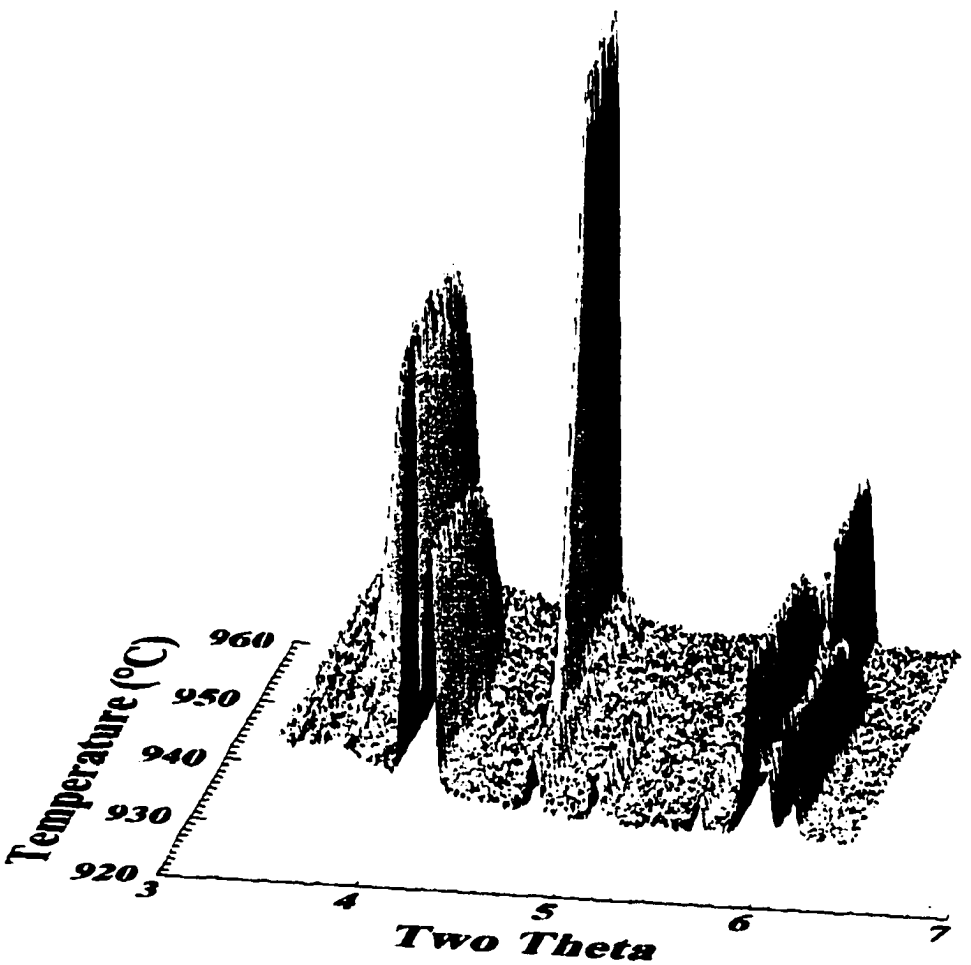


Figure 32. Surface plot of the outlined phase transition region on heating from fig. 31.

transformation region that is captured at this time resolution. One can observe the nucleation and growth of the high temperature phase at the expense of the low temperature phase. Ideally, one would like to perform sequentitial refinements throughout this region in order to track transient structural changes in the transforming phases. A Rietveld refinement of a cut of the two phase transformation region is shown in figure 33. Both phase could be successfully fit with a weighted residual of 5.87%. The ability to perform structural refinement on time resolved patterns collected during phase transformations allows a variety of information to be collected. Refinements were performed on 45 cuts along the image plate. Lattice parameters were fit for both phases. It is interesting to track the lattice parameters of the high temperature phase as it nucleates and grows. Figure 34 shows the a and c cell parameters as a function of temperature. The c parameter shows reversible behavior on heating and cooling. This demonstrates the lack of significant temperature hysteresis between heating and cooling due to thermal lag of the furnace. Any deviation from reversibility, then, can be reasonably attributed to real sample effects rather than furnace induced artifacts. This is important as the a cell parameter does shows hysteretic behavior. The newly nucleated phase seems to be anisotropically strained along the a direction, and this strain slowly relaxes over time. This strain may be caused by an epitaxial relationship between the nucleating high temperature phase and the low temperature matrix phase. If this were the case, though, one would expect the strain to relax once the high temperature phase had consumed the matrix. This is not the case as the hysteresis is maintained well after the transformation is complete. It is possible that this strain is maintained in the transformed structure and that recrystallization occurs in order to relax this strain.

Collecting time resolved patterns during first order phase transformations allows the kinetics of nucleation and growth to be studied. Measuring the rate of a transformation can reveal information on the transformation mechanism. The Avrami equation describes how the volume fraction of a nucleating phase changes with time and is expressed as

$$F = 1 - \exp(-kt^n) \qquad (6)$$

where k depends on the nucleation and growth rates. A number of nuclei growth models for solid state reactions have been developed. Depending on the details of the kinetic model

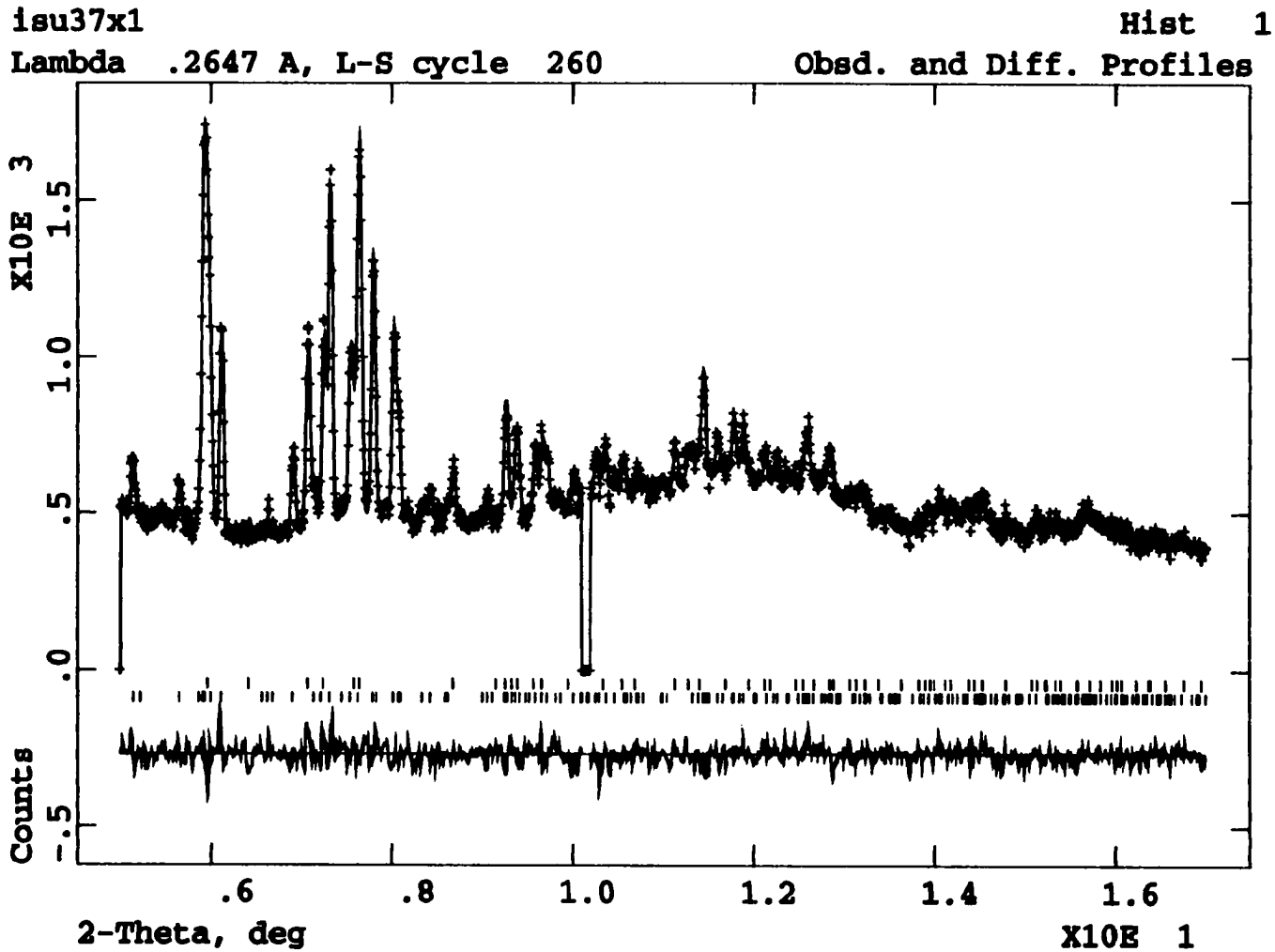


Figure 33. Rietveld refinement of the two phase transformation region in $SrCO_3$ at 950°C.

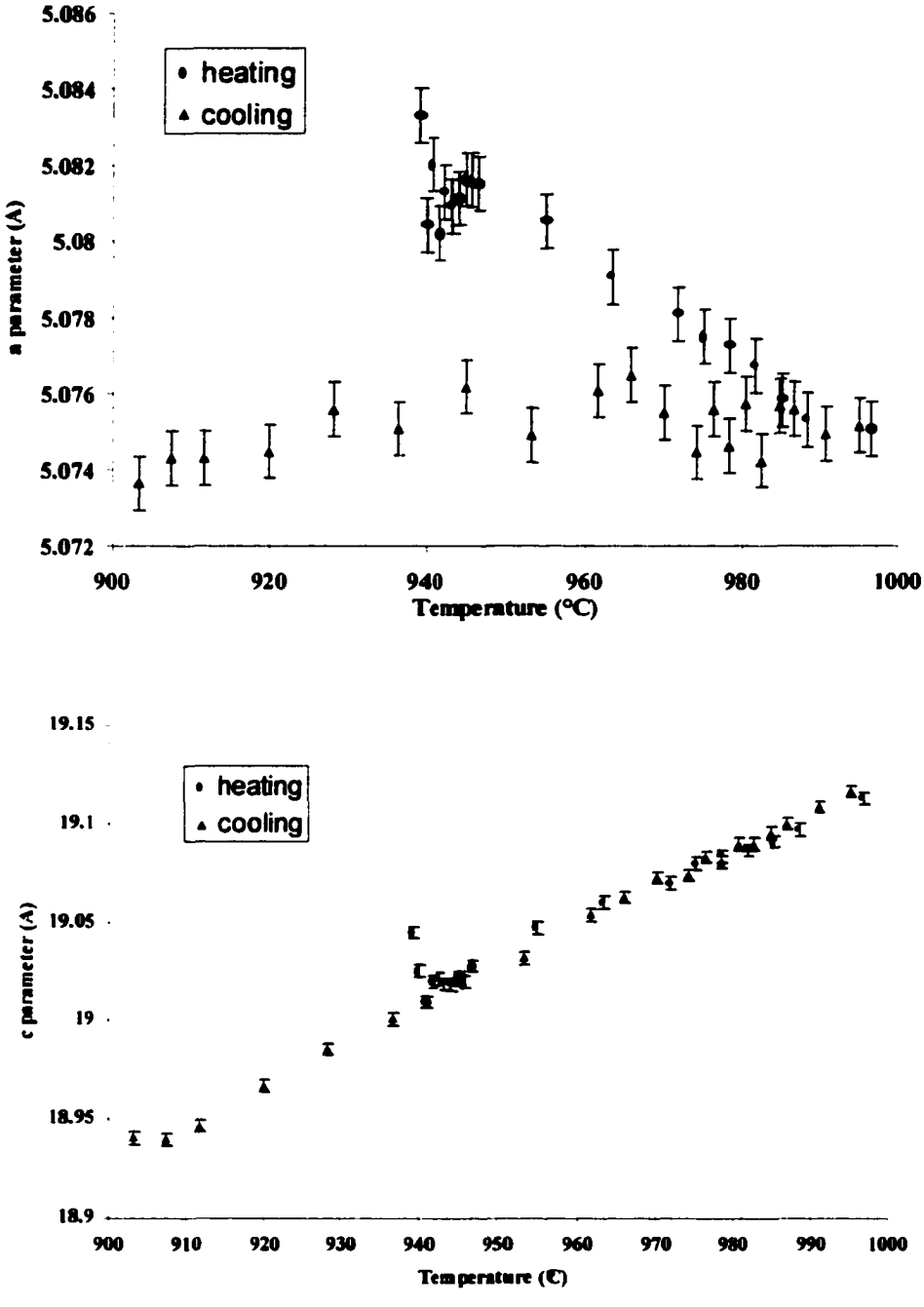


Figure 34. The a and c cell parameters for the high temperature phase of $SrCO_3$ on heating and cooling.

assumptions, the exponent n can vary from .5 to 4. Rietveld refinement of multiphased patterns is a very accurate methods for measuring quantitative phase fractions. The volume fraction of the high and low temperature forms of $SrCO_3$ were refined throughout the two phase transformation region. Figure 35 shows the volume fraction of the high temperature phase fit to the avrami equation during nucleation and growth on heating through the transformation temperature. Since the nucleation and growth rates (and therefore, k) are temperature dependent, the Avrami equation is strictly only valid for isothermal processes. The $SrCO_3$ transformation is extremely rapid and goes to completion over a small temperature range, so in this case a fairly reasonable fit can be made. The least squares fit suggests an avrami exponent which is close to 4. This is consistent with a three dimensional growth model which is phase boundary controlled rather than diffusion controlled[136]. For an allotropic phase transformation, one would not expect long range diffusion. Accordingly, the kinetically limiting mechanism should be associated with atomic mobility at the transformation boundary.

**Bi2212 revisited**

The use of synchrotron radiation for performing full bulk sampling in a controlled low thermal gradient environment should provide a reliable probe of the partial liquid phase equilibria in the Bi-Sr-Ca-Cu-O system. This should help resolve some of the questions that arise due to discrepancies between quenching and conventional high temperature x-ray diffraction results. As outlined in part I, a number of factors including thermal gradients and phase separation, bring into suspicion many of the results observed with conventional strip heater diffractometers. The quenching results reported in the literature are more consistent, however, it is important to verify the validity of this approach through in situ methods. In the end, quenching is an indirect method of determining the high temperature phase equilibria, and the possibility of artifacts being introduced during the quenching process always exists.

For the Bi2212 system in particular, a point of contention between quenching studies and conventional high temperature x-ray diffraction is the existence of the Cu-free (9$\underline{1}$1$\underline{5}$) phase in the high temperature partial melt. It was suggested in part I that this phase is denser than the liquid and may sink below the penetration depth of the x-rays in conventional

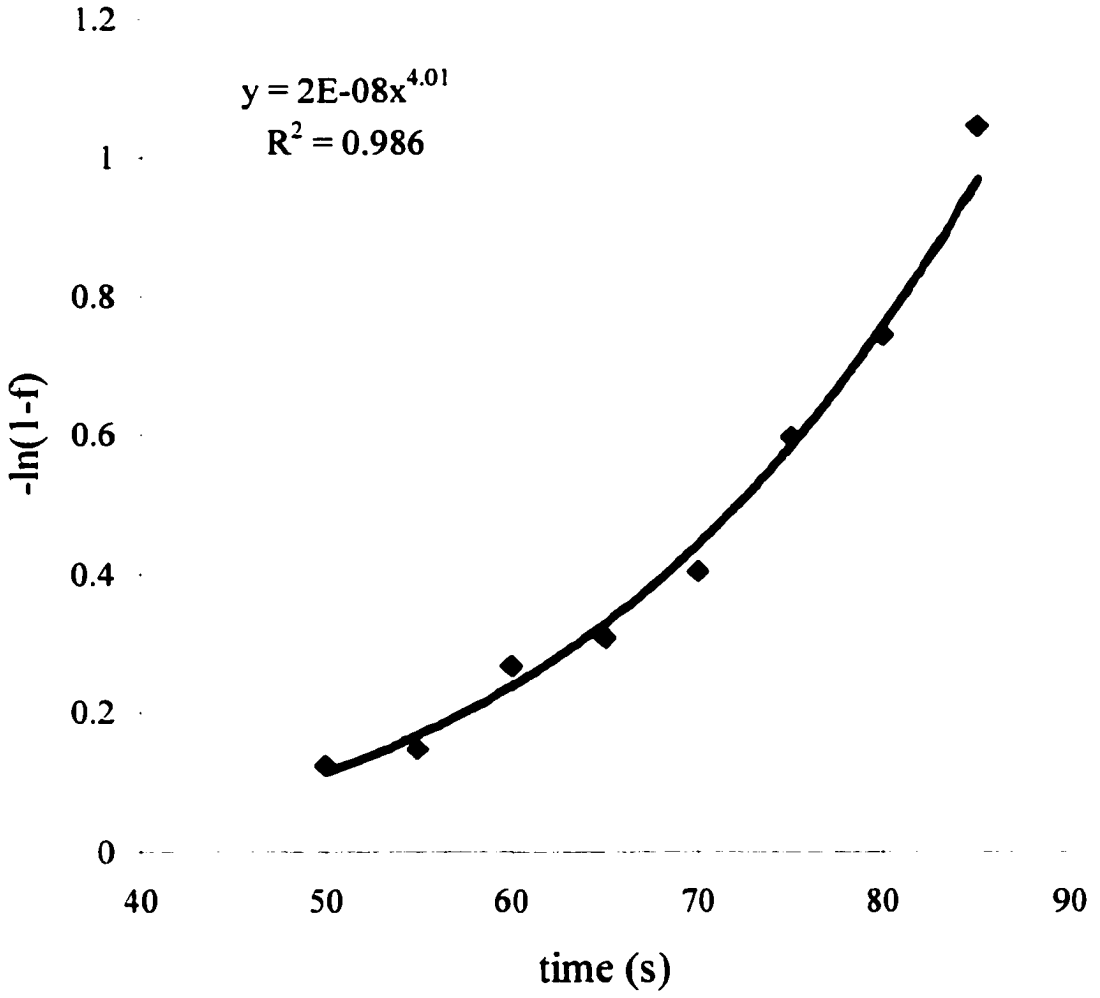


Figure 35. The increase in volume fraction of the high temperature $SrCO_3$ phase as a function of time follows the Avrami relation.

systems. If this is indeed the case, then we should be in the position to successfully detect this phase with the new furnace design coupled with high energy synchrotron radiation.

According to the quenching results of part I, in 100% $O_2$, Bi2212 will undergo the peritectic reaction, Bi2212 → liquid + (9$\underline{1}$15) + (14,24) at 900°C. At this high $PO_2$ there should be a significant volume fraction of (9$\underline{1}$15) in the melt in this first supersolidus phase region. The Bi2212 sample was packed into a 2 mm ID MgO tube. Au foil was pressed into either end of the tube to prevent the liquid from flowing down the tube and out of the beam. Au is known to be non-reactive with the Bi2212 melt. Data was collected while heating at 1°C/min through the first peritectic reaction. 10 second exposures were taken every minute. Figure 36 shows a surface plot of the data from 880°C to 920°C. The peritectic reaction is clearly captured and crystalline peaks in the partial liquid phase region could be indexed to the (14,24) and (9$\underline{1}$15) phases. This confirms the reliability of the quenching results presented in part I and underscores the problems associated with conventional high temperature x-ray diffraction measurements.

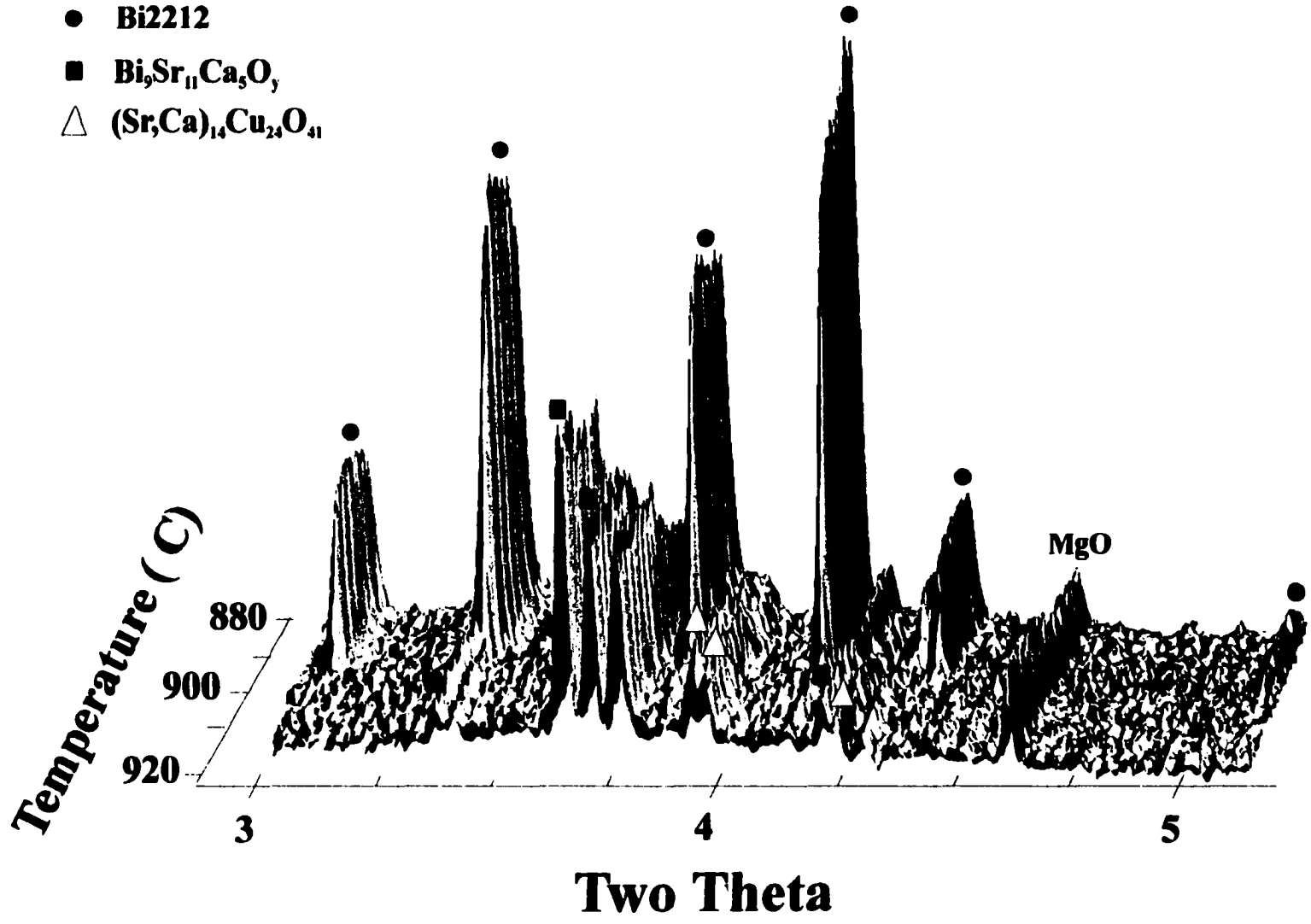


Figure 35. The peritectic decomposition of Bi2212 in 100% $O_2$. The (14,24) and (9115) phases are observed in the melt.

# GENERAL CONCLUSIONS

The use of synchrotron radiation has allowed for significant improvements in the quality and reliability of high temperature x-ray diffraction measurements. By using high energy x-rays in a Debye-Scherrer transmission geometry, full bulk sampling is achieved within a well insulated low thermal gradient environment. In addition, this geometry allows for sample rotation and minimizes preferred orientation. As a result, reliable Rietveld refinement can be performed on high temperature powder patterns. This opens the possibility for performing unique studies into the kinetics of phase transformations when coupled with position sensitive detectors. In the future, the use of CCD detectors should improve both the data quality and time resolution. The flux available at third generation synchrotron sources should allow for a time resolution on the order of a tenth of a second. With more efficient monochromator optics, the maximum time resolution possible before signal to noise becomes unacceptably low is potentially considerably faster. Ideally, one would like to tailor the bandwidth of the monochromator optics to match the resolution function due to the sample and detector geometry. In practice, this will most certainly be controlled by sample size.

Phase equilibria studies may also be improved through these techniques. For partial liquid phase regions it has been demonstrated that this high temperature diffraction design does not suffer from the experimental artifacts inherent in conventional designs. As a result, reliable phase equilibria data can be collected for difficult systems such as Bi-Sr-Ca-Cu-O-Ag. The results presented in part I and part II on this system are consistent and complimentary. Although high temperature x-ray diffraction is a more time-efficient, direct probe of the high temperature phase equilibria, it cannot provide microstructural details. Ideally, one would like to utilize both high temperature in situ diffraction measurements and quenching experiments to maximize the reliability of both techniques. Examination of a few coarsely gridded quench samples would allow for chemical identification of equilibrium phases and observation of morphology. High temperature x-ray diffraction should then be used to complete the details of the phase boundaries and verify the crystallographic identity of the high temperature phases. Additionally, when time resolved techniques are used, the

potential for studying the kinetics of the phase transformations exists and transient metastable phases may be captured that would be missed in quenching studies.

# APPENDIX

Table 12. Refined parameters for high resolution step scans of $Al_2O_3$.

| | 293 K | 873 K | 1473 K |
|---|---|---|---|
| a (Å) | 4.75957(4) | 4.77953(4) | 4.80754(4) |
| c (Å) | 12.9926(3) | 13.0551(3) | 13.1383(3) |
| Al (z) | .3528(1) | .3531(1) | .3533(1) |
| B(Al) | .54 | .86 | 1.42 |
| O (x) | .3066(5) | .3070(5) | .3071(5) |
| B(O) | -.26 | .16 | .42 |
| λ (Å) | .203364 | .203364 | .203364 |
| Zero (°) | .006 | .006 | .006 |
| GU | 68.0 | 44.0 | 35.2 |
| GV | -6.33 | -3.31 | -2.93 |
| GW | .19 | .1 | .1 |
| LX | .44 | .46 | .44 |
| LY | 4.26 | 3.32 | 2.78 |
| Asym | -.017 | -.022 | -.029 |
| Δf(Al) | -.004 | -.004 | -.004 |
| Δf'(Al) | .004 | .004 | .004 |
| Δf(O) | -.002 | -.002 | -.002 |
| Δf'(O) | .000 | .000 | .000 |
| $R_p$ | .0989 | .0957 | .0933 |
| $R_{wp}$ | .1300 | .1227 | .1209 |

Table 13. Refined parameters for time resolved image plate scan of $Al_2O_3$ using a real space background distribution function.

| | 293 K | Background Coefficients | 293 K |
|---|---|---|---|
| a (Å) | 4.75989(5) | | |
| c (Å) | 12.9897(4) | B1 | -.35954E+05 |
| Al (z) | .3521(3) | B2 | .23961E+04 |
| B(Al) | -1.09 | B3 | .59044E+04 |
| O (x) | .3063(15) | B4 | .14880E+01 |
| B(O) | -1.23 | B5 | .31663E+05 |
| λ (Å) | .264803 | B6 | .49000E+00 |
| Zero (°) | .004 | B7 | .46540E+04 |
| GU | 1713 | B8 | .42974E+01 |
| GV | -259.9 | B9 | .57351E+04 |
| GW | 13.8 | B10 | .50994E+01 |
| LX | 0 | B11 | .32564E+04 |
| LY | 0 | B12 | .59124E+01 |
| Asym | .0197 | B13 | -.19868E+04 |
| Δf'(Al) | .002 | B14 | .72277E+01 |
| Δf''(Al) | .006 | B15 | .90926E+03 |
| Δf'(O) | -.002 | B16 | .25655E+02 |
| Δf''(O) | .007 | B17 | .18918E+04 |
| $R_p$ | .0693 | B18 | .89490E+01 |
| $R_{wp}$ | .0534 | B19 | .34579E+04 |
| | | B20 | .16915E+03 |
| | | B21 | -.19763E+04 |
| | | B22 | .38833E+02 |
| | | B23 | .17587E+04 |
| | | B24 | .13075E+02 |

## REFERENCES


1 S. X. Dou, Supercond. Sci. Tech. 3 (1990) 138.

2 A. P. Malozemoff, Cryogenics 32, ICMC Supplement (1992) 478.

3 Y. Yamada, J.Q. Xu, J. Kessler, E. Seibt, W. Goldacker, W. Jahn, R. Flukiger, Physica C 185-189 (1991) 2483.

4 L. Civale, et al., Phys. Rev. Lett. 67 (1991) 648.

5 M. A. Kirk, H. W. Weber, Studies of High-Temperature Superconductors, Vol 10, 243 (1992).

6 M. Murakami, S. Gotoh, H. Fujimoto, K. Yamaguchi, N. Koshizuka, S. Tanaka, Supercond. Sci. Tech. 4 (1991) 543.

7 H. Wu, M.J. Kramer, K.W. Dennis, R.W. McCallum, Appl. Phys. Lett. 71 (1997) 3572.

8 J. Case, N. Irisawa, T. Morimoto, K. Togano, H. Kumakura, D. R. Dietderich, H. Maeda, Appl. Phys. Lett. 56 (1990) 970.

9 E.E. Hellstrom, R.D. Ray II, W. Zhang, Appl. Supercond. 1 (1993) 1535.

10 M. J. Kramer, L. Margulies, S. R. Arrasmith, K. W. Dennis, J. C. Lang, R. W. McCallum, P.K. Gallagher, J. Mater. Res. 9 (1994) 1661.

11 Y. Kuba, K. Michishita, N. Shimizu, Y. Higashida, H. Yokoyama, Y. Hayami, E. Inukai, A. Saji, N. Kuroda, H. Yoshida, Jpn. J. Appl. Phys. 28 (1989) L1936.

12 W. Gao, J.B. Vandersande, Physica C 181 (1991) 105.

13 W. Lee, Y. Abe, E. Inukai, J. Am. Cer. Soc. 76 (1993) 849.

14 T. E. Jones, W. C. McGinnis, E. W. Jacobs, R. D. Boss, P. M. Thibado, J. S. Briggs, W. E. Glad, Physica C 201 (1992) 279.

15 Y. Fang, S. Danyluk, K. C. Goretta, N. Chen, M. Runde, S. J. Rothman, J. L. Routbort, Appl. Phys. Lett. 60 (1992) 2291.

16 J.B. Parise, C.C. Torardi, C.J. Rawn, R.S. Roth, B.P. Burton, A. Santoro, J. Solid State Chem. 102 (1993) 132.

16 J.B. Parise, C.C. Torardi, C.J. Rawn, R.S. Roth, B.P. Burton, A. Santoro, J. Solid State Chem. 102 (1993) 132.

17 B. Hong, J. Hahn, T.O. Mason, J. Am. Ceram. Soc. 73 (1990) 1965.

18 C.J. Rawn, R.S. Roth, H.F. McMurdie, Powder Diffr. 7 (1992) 109.

19 B.P. Burton, C.J. Rawn, R.S. Roth, N.M. Hwang, J. Res. Natl. Inst. Stand. Technol. 98 (1993) 469.

20 R.S. Roth, N.M Hwang, C.J. Rawn, B.P. Burton, J.J Ritter, J. Am. Ceram. Soc. 74 (1991) 2148.

21 U.C. Boehnke, P. Heitman, M. Krotzsch, B. Lippold, G. Zhan, J. Mater. Sci. 28 (1993) 111.

22 R. Shimpo, Y. Nakamura, Metall. Mater. Trans. B 25B (1994) 97.

23 J.B. Parise, C.C. Torardi, M. H. Whangbo, C.J. Rawn, R.S. Roth, B.P. Burton, Chem. Mater. 2 (1990) 454.

24 P. Conflant, J.C. Boivin, G. Tridot, C. R. Seances. Acad. Sci., Ser C 279 (1974) 457.

25 P. Conflant, J.C. Boivin, D.J. Thomas, J. Solid State Chem. 18 (1976) 1333.

26 J. Cassedanne, C.P. Campelo, An. Acad. Brasil. Cienc. 38(1966) 36.

27 J.C. Boivin, D.J. Thomas, G. Tridot, C.R. Seances Acad. Sci., Ser. C 276 (1973) 1105.

28 A.M. Murenkov, P.M. Zaitsev, I.V. Popik, L.E. Semikina, Russ. J. Phys. Chem. 47 (1973) 593.

29 M. Arjomand, D.J. Machin, J. Chem. Soc., Dalton Trans. 11(1975) 1061.

30 R. Arpe, H. Muller-Buschbaum, Z. Anorg. Allg. Chem. 426 (1976) 1.

31 J.C. Boivin, J. Trehoux, D. Thomas, Bull. Soc. Fr. Mineral. Cristallogr. 99 (1976) 193.

32 B.G. Kakhan, V.B. Lazarev, I.S. Shaplygin, Russ J. Inorg. Chem. 24 (1979) 922.

33 V.V. Belousov, V.N. Konev, A.K. Roslik, Sverkhprovodimost: Fiz., Khim., Tekh 3 (1990) 1890.

34 R. S. Roth, C.J. Rawn, B.P. Burton, F. Beech, J. Res. Nat. Inst. Stand. Technol. 95 (1990) 291.

35 R. Horyn, I. Fhatow, J. Ziaji, M. Wolcyrz, Supercond. Sci. Technol. 3 (1990) 347.

36 R. Guillermo, P. Conflant, J.C. Bovin, D.J. Thomas, Rev. Chim. Miner. 15 (1978) 153.

37 C.C. Torardi, J.B. Parise, A. Santoro, C.J. Rawn, R.S. Roth, B.P. Burton, J. Solid State. Chem. 93 (1991) 228.

38 W. Wong-Ng, H. McMurdie, B. Paretzkin, C. Hubbard A. Dragoo, Powder Diffraction 3 (1988) 186.

39 P. Conflant, J.C. Boivin, C.R. Seances Acad. Sci., Ser. C 288 (1979) 161.

40 L. G. Sillen, B. Aurivillius, Z. Krist. 10 (1943) 483.

41 E.M. Levin, R.S. Roth, J. Res. Natl. Bur. Stand. 68 (1964) 197.

42 F. Abbattista, C. Brisi, D. Mazza, M. Vallino, Mat. Res. Bull. 26 (1991) 107.

43 A.M.M. Gadalla, J. White, Trans. Br. Ceram. Soc. 65 (1966) 181.

44 R.S. Roth, C.J. Rawn, J.J. Ritter, B.P. Burton, J. Am. Ceram. Soc. 72 (1989) 1545.

45 T. Siegrist, R.S. Roth, C.J. Rawn, J.J. Ritter, Chem. Mater. 2 (1990) 192.

46 C.L. Teske, H. Mueller-Buschbaum, Z. Anorg. Allg. Chem. 370 (1970) 234.

47 D. Risold, B. Hallstedt, L. Gaukler, J. Am. Ceram. Soc. 78 (1995) 2655.

48 T. Mathews, J.P. Hajra, K.T. Jacob, Chem. Mater. 5 (1993) 1669.

49 J.K. Liang, Z. Chen, F. Wu, S.S. Xie Solid State Commun. 75 (1990) 247.

50 K.T. Jacob, P.M. Raj, Y. Waseda, J. Phase Equilib. 16 (1995) 113.

51 B.V. Slobodin, A.A. Fotiev, N.A. Pakhomov, Russ. J. Inorg. Chem. 36 (1991) 286.

52 Y. Ikeda, H. Ito, S. Shimomura, Z. Hiroi, M. Takano, Y. Bando, J. Takada, K. Oda, H. Kitaguchi, Y. Miura, Y. Takeda, T. Takeda, Physica C 190 (1991) 18.

53 C.J. Rawn, R.S. Roth, B.P. Burton, M.D. Hill, J. Am. Ceram. Soc. 77 (1994) 2173.

54 W. Wong-Ng, C.J. Rawn, R.S. Roth, J. Am Ceram. Soc. 80 (1997) 324.

55 R.S. Roth, B.P. Burton, C.J. Rawn N.M. Hwang, Ceramic Transactions, vol.13 (1990) 23.

56 R. Muller, Th. Schweizer, P. Bohac, R.O. Zuzuki, L.J. Gaukler, Physica C 203 (1992) 299.

57 M. Yoshida, A. Endo, Jpn. J. Appl. Phys. 32 (1993) L1509.

58 Y. Ikeda, H. Ito, S. Shimomura, Y. Oue, K Inaba, Z. Hiroi, M. Takano, Physica C 159 (1989) 93.

59 Y. Idemoto, S. Kobayashi, K. Fueki, Physica C 29 (1994) 47.

60 R.S. Roth, C.J. Rawn, L.A. Bendersky, J. Mater. Res. 5 (1990) 46.

61 D. Sedmidubsky, E. Pollert, Physica C 217 (1993) 203.

62 B.V. Slobodin, I.A. Ostapenko, A.A. Fotiev, Inorg. Mater. 27 (1991) 2220.

63 K.T. Jacob, T. Mattews, J. Mater. Chem. 1 (1991) 545.

64 K. Schulze, P. Majewski, B. Hettich, G. Petzow, Z. Metallkd 81 (1990) 836.

65 R. Muller, T. Schweizer, P. Bohac, R.O. Suzuki, L.J. Gaukler, Physica C 203 (1992) 299.

66 A. Fuertes, C. Miravitlles, J. Gonzalez-Calbet, M. Vallet-Regi, X. Obradors, J. Rodriguez-Carvajal, Physica C 157 (1989) 525.

67 J.A. Saggio, K. Sugata, J. Hahn, S. Hwu, K.R. Poeppelmeir, T.O. Mason, J. Am. Ceram. Soc. Commun. 72 (1989) 849.

68 R.S. Roth, C.J. Rawn, J.J. Ritter, B.P. Burton, J. Am. Ceram. Soc. 72 (1989) 1545.

69 T. Siegrist, S.M. Zahurak, D.W. Murphy, R.S. Roth, Nature 334 (1988) 231.

70 M. Xu, E.T. Voiles, L.S. Chumbley, A.I. Goldman, D.K. Finnemore, J. Mater. Res. 7 (1992) 1283.

71 J.A. Alonso, G. Lapertot, Physica C 250 (1995) 93.

72 E. George, D. Elthon, J.K. Meen, J. Am. Ceram. Soc. 78 (1995) 3309.

73 C. Lee, J. Chen. W. Wen, T. Perng, J. Wu, T. Wu, T. Chin, R. Liu , P. Wu, J. Mater. Res. 5 (1990) 1403.

74 T. Suzuki, K. Yumoto, M. Mamiya, M. Hasegawa, H. Takei, Physica C 301 (1998) 173.

75 P. Strobel, J.C. Toledano, D. Morin, J. Schneck, G. Vacquier, O. Monnereau, J. Primot, T. Fournier, Physica C 201 (1992) 27.

76 J.L. MacManus-Driscoll, Y.H. Li, Z. Yi, J. Am. Ceram. Soc. (1996).

77 L.M. Rubin, T.P. Orlando, J.B. Vander Sande, G. Gorman, R. Savoy, R. Swope, R. Beyers, Appl. Phys. Lett. 61 (1992) 1977.

78 W. Wong-Ng, L.P. Cook, F. Jiang, J. Am. Ceram. Soc. (1997).

79 U. Endo, S. Koyama, T. Kawai, Jpn. J. Appl. Phys. 27 (1988) L1476.

80 P. Majewski, B. Hettich, Mater. Res. Soc. Symp. Proc. 275 (1992) 627.

81 T.G. Holesinger, D.J. Miller, L.S. Chumbley, M.J. Kramer, K.W. Dennis, Physica C 202 (1992) 109.

82 Y. Oka, N. Yamamoto, H. Kitaguchi, K, Oda, J, Takada, Jpn. J. Appl. Phys. 28 (1989) L213.

83 Y. Oka, N. Yamamoto, Y. Tomii, H. Kitaguchi, K. Oda, J. Takada, Jap. J. Appl. Phys. 28 (1989) L801.

84 A. Endo, S. Nishikida, IEEE Trans. Appl. Supercond. AS-3 (1993) 931.

85 W. Zhang, E. Hellstrom, Supercond. Sci. Tech. (1995) 430.

86 J. MacManus-Driscoll, J. Brauman, R. Savoy, G. Gorman, R. Beyers, J. Am. Cer. Soc. 77 (1994) 2305.

87 D. Buhl, T. Lang, B. Heeb, L.Gaukler, Proc. 4$^{th}$ Congr. on Superconductivity, Orlando, Fl, USA (1994).

88 K. Heine, J. Tenbrink, M. Thoner, Appl. Phys. Lett 55 (1989) 2441.

89 J. Tenbrink, M. Wilhelm, K. Heine, H. Krauth, IEEE Trans. Mag. MAG-27 (1991) 1239.

90 T. Hasegawa, T. Kitamura, H. Kobayashi, H. Kumakura, H. Kitaguchi, K. Togano, Appl. Phys. Lett. 60 (1992) 2692.

91 T. Hasegawa, H. Kobayashi, H. Kumakura, H. Kitaguchi, K. Togano, Proc. 5th International Symposium on Superconductivity (1993) 737.

92 T. Hasegawa, H. Kobayashi, H. Kumakura, H. Kitaguchi, K. Togano, Physica C 222 (1994) 111.

93 J. Polonka, M. Xu, Q. Li, A. Goldman, D. Finnemore, Appl. Phys. Lett. 59 (1991) 3640.

94 D. P. Matheis, S.T. Misture, R.L. Snyder, Physica C 217 (1993) 319.

95 J. Kase, K. Togano, H. Kumakura, D.R. Dietderich, N. Irisawa, T. Morimoto, H. Maeda, Jpn. J. Appl. Phys. 29 (1990) L1096.

96 T. Hasebe, Y. Tanaka, T. Yanagiya, T. Asano, M. Fukitomi, H. Maeda, Jpn. J.Appl. Phys. 31 (1992) L21.

97 T. Suzuki, K. Yumoto, M. Mamiya, M. Hasegawa, H. Takei, Physica C 301 (1998) 173.

98 M. Yoshida, Jpn. J. Appl. Phys. 34 (1995) 98.

99 E.E. Hellstrom, W. Zhang, Proc. 6th International Symposium on Superconductivity (1994) 247.

100 J. Case, N. Irisawa, T. Morimoto, K. Togano, H. Kumakura, D. Dietderich, H. Maeda, Appl. Phys. Lett. 56 (1990) 970.

101 M. Kramer, L. Margulies, S. Arrasmith, K. Dennis, J. Lang, R. McCallum, P. Gallagher, J. Mater. Res. 9 (1994) 1661.

102 T. Lang, D. Buhl, M. Cantoni, L. Gauckler, Proc. for the European Conference on Applied Superconductivity, Edinburgh, Scotland, July 3-6, 1995.

103 W. Zhang, E. Hellstrom, poster presented at MRS meeting, Nov. 1993.

104 M. Xu, J. Polonka, A. I. Goldman, and D. K. Finnemore, Applied Superconductivity, Vol 1, No. 1/2(1993) 53.

105 H. Komatsu, Y. Kato, S. Miyashita, T. Inoue, and S. Hayashi, Physica C 190 (1991) 14.

106 J. L. Macmanus-Driscoll, Pin-Chin Wang, J. C. Bravman, Appl. Phys. Lett. 65 (1994) 2872.

107 R. W. McCallum, K. W. Dennis, L. Margulies, and M. J. Kramer, Proc.

108 J. Cassedanne and C. P. Campelo, An. Acad. Brasil. Cienc. 38 (1966) 36.

109 C. Park, S. T. Misture, D. Sriram, R. L. Snyder, J. Electronic Mat. 24 (1995) 1897.

110 S. T. Misture, D. P. Matheis, R. L. Snyder, T. N. Blanton, G. M. Zorn, B. Seebacher. Physica C 205 (1995) 175.

111 J. Wang, R. Stevens, J. Bultitude, Journal of Materials Science 23 (1988) 3393.

112 H. Fjellvag, P. Karen, A. Kjekshus, P. Kofstad and T. Norby. Acta Chem. Scand. A23 (1988) 178.

113 T. Hasegawa, T. Kitamura, H. Kobayashi, H. Kumakura, H. Kitaguchi, and K. Togano, Appl. Phys. Lett. 60 (1992) 2692.

114 F. Abbattista, C. Brisi, D. Mazza, and M. Vallino, Mat. Res. Bull 26 (1991) 107.

115 R. Muller, M. Cantoni, L. J. Gauckler, Physica C 243 (1995) 103.

116 J. L. MacManus-Driscoll, J. C. Bravman, R. B. Beyers, Physica C 251 (1995) 71.

117 J. Shimoyama, J. Kase, T. Morimoto, H. Kitaguchi, H. Kumakura, K. Togano, H, Maeda. Jpn. J. Appl. Phys. 31 (1992) L1167.

118 J. Assal, PhD thesis, Swiss Federal Institute of Technology (1998).

119 J. B. Hastings, W. Thomlinson, D. E. Cox, J. Appl. Cryst. 17(1984) 85.

120 P. Thompson, I. G. Wood, J. Appl. Cryst. 16(1983) 458.

121 P. Thompson, D. E. Cox, J. B. Hastings, J. Appl. Cryst. 20 (1987) 79.

122 M. S. Lehmann, A. N. Christensen, H. Fjellvag, R. Feidenhans'l, M. Nielsen, J. Appl. Cryst. 20 (1987) 123.

123 D. E. Cox, B. H. Toby, M. M. Eddy, Aust. J. Phys. 41 (1988) 117.

124 F. Marumo, H. Morikawa, Y. Shimizugawa, M. Tokonami, M. Miyake, K. Ohsumi. S. Sasaki, Rev. Sci. Instrum. 60 (1989) 2421.

125 S. E. Rasmussen, J. Jorgensen, B. Lundtoft, J. Appl. Cryst. 29 (1996) 42.

126 F. Muller, I. Rannou, L. Duclaux, J. M. Guet, J. Appl. Cryst. 30 (1997) 557.

127 J. Schreuer, A. Baumgarte, M. A. Estermann, W. Steurer, H. Reifler, J. Appl. Cryst. 29 (1996) 365.

128 Peakfit v3.0, Jandel Scientific (1990).

129 P. Coppens and D. E. Cox, Synchrotron Radiation Crystallography, (Academic Press Limited, 1992), Ch. 3, pp. 186-254.

130 H. M. Rietveld, J. Appl. Cryst. 2 (1969) 65.

131 A. C. Larson, R. B. Von Dreele, Report LAUR 86-748, GSAS (Los Alamos National Laboratory, Los Alamos, N.M., 1994).

132 International Tables for X-ray Crystallography, Vol. III, Edited by C. H. MacGilavry, G. D. Rieck, and K. Lonsdale, (Knoch Press, Birmingham, 1959).

133 L. D. Calvert, E. J. Gabe, Y. Le Page, Acta Cryst. A37 (1981) C314.

134 N. Ishizawa, T. Miyata, I. Minato, F. Marumo, S. Iwai, Acta Cryst. B36 (1980) 228.

135 M. Catti, A. Pavese, Acta Cryst. B54 (1998) 741.

136 S.F. Hulbert, J. Brit. Ceram. Soc. 6 (1969) 11.